Theoretical Exploration of Ultrafast Dynamics in Atomic Clusters: Analysis and Control†

Vlasta Bonačić-Koutecký* and Roland Mitrić

Institut für Chemie, Humboldt-Universität zu Berlin, Brook-Taylor-Strasse 2, D-12489 Berlin, Germany

Received August 2, 2004

Contents

1. Introduction

Theoretical investigations of femtosecond dynamical processes in elemental clusters and their active control by designed light fields are of fundamental importance for learning how the interplay of size, structures, and lasers can be used to manipulate optical properties and chemical reactivity of these species. This research area provides a potential for establishing foundations for combining laser-selective femtochemistry[1−11] with the functionalism of nanostructures, opening new perspectives for the basic research and numerous technological applications. In this context, exploration of clusters in the size regime in which each atom counts[12−15] is of particular importance. This is due to the fact that in this case structures and the number of atoms determine the size-selective optical and reactivity properties of clusters. Moreover, they are excellent candidates to study dynamics of systems with finite density of states, where the separation of time scales is feasible.[14] The purpose of the present review is threefold: to survey the present status of theoretical concepts and computational approaches applicable for investigation of time-resolved processes and their optical control by designed laser fields in elemental clusters; to show the importance of the interplay between theory and experiments; and to stimulate new developments and new directions in this research area. We focus on analysis and control of ultrafast processes in weak fields and in gas-phase elemental clusters with binding energies beyond those of weakly bound van der Waals clusters.

The review is organized as follows. Section 2 serves to establish the connection between developments in

† See also the thematic issue "Femtochemistry", *Chemical Reviews* **2004**, *104* (4), 1717−2124, Marcos Dantus and Ahmed Zewail, Guest Editors.

* To whom correspondence should be addressed. Fax: +4930/2093 5573. Phone: +4930/2093 5576/5579. E-mail: vbk@chemie.hu-berlin.de.

10.1021/cr0206925 CCC: $53.50
Published on Web 12/22/2004

Vlasta Bonačić-Koutecký received her diploma in 1967 from the University of Zagreb, Croatia, and her doctoral degree in 1971 from the Johns Hopkins University, Baltimore, MA. After postdoctoral studies at the Belfer Graduate School of Science, Yeshiva University, New York, she was Assistant Professor in the Chemistry Department at Freie Universität Berlin, where she habilitated in 1977. Following research and teaching activity at Gesamthochschule Wuppertal (1979–1980), she was nominated as Professor in the Chemistry Department at Freie Universität Berlin in 1982. Since 1994, she has been Professor of Physical and Theoretical Chemistry at Humboldt-Universität zu Berlin. Her research activities cover the field of chemical physics, including ab initio quantum chemistry and molecular dynamics as well as theoretical bioorganic photochemistry. The choice of the scientific problems and the interest in developing theoretical methods are strongly oriented toward their capability to extract chemical and physical properties of the studied systems, providing interpretation and basic understanding of the experimental results. Her present research directions are as follows: (1) chemical reaction control or laser selective chemistry of nanoclusters with tailored light fields; (2) structure–reactivity relationships of metal oxide clusters as foundations for the development and design of nanoscale catalytic materials; (3) photophysical and photochemical size selective properties of metallic clusters and their potential for optical storage elements and for emitters in optical devices; (4) elucidations of mechanisms responsible for conformational changes in biological and biooraganic systems, including electronic and dynamical aspects.

Roland Mitrić received his diploma in 1998 from the University of Zagreb, Croatia, and Ph.D. in 2003 from Humboldt University of Berlin, Germany. The subject of his graduate work with Prof. V. Bonačić-Koutecký was the study of reactivity, optical properties, and ultrafast processes in atomic clusters and development of semiclassical methods for control of ultrafast dynamics in complex systems, which was awarded by two prizes. His present research interests include the combination of ab initio quantum chemistry with molecular dynamics methods for control of ultrafast processes in biomolecules and of reactivity in atomic clusters.

cluster science and femtosecond spectroscopy. This sets up requirements on the theory to introduce means for analyzing and controlling the ultrafast processes and to provide the conceptual frame for observations. For this purpose contributions from quantum chemistry, molecular dynamics, wave packet propagation, and theory of optical control are needed. Therefore, the aim of this paper is not to give a complete review of each of these fields separately, but rather to focus on unifying interdisciplinary aspects. In section 3 we address methods for investigations of ultrafast dynamics and for simulations of femtosecond signals (fs-signals). Their applications to elemental clusters with different sizes and atomic compositions, allowing us to analyze the underlying processes and to predict observable properties, are given in section 4. Section 5 is devoted to control of ultrafast processes in clusters by tuning laser parameters or using tailored fields. The summary and outlook are given in section 6. Section 7 contains a list of references which is constructed according to the interdisciplinary aspect of this review and therefore does not provide a complete literature survey for each of the involved research fields. Appendices A and B serve as supporting material for sections 4.2.1 and 4.3.1.

2. Cluster Research and Ultrafast Time Resolved Phenomena

2.1. General

Over the last three decades cluster science has become an established and recognized research area in physical and theoretical chemistry and molecular physics. This is due to numerous important discoveries emerging from pronounced size-dependent microscopic properties which clusters, isolated or embedded in different media, can exhibit. Experimentally, the clusters have been observed in supersonic expansions, their size has been selected by mass spectrometers, and their spectroscopic properties have been precisely determined by different laser techniques (cf. books and reviews for refs 2, 13, and 16−23). The investigations of clusters have been carried out in the gas-phase,[13,16,20−23] in matrixes of rare gas atoms,[24−28] and on different support materials,[29−34] and their reactivity toward organic and inorganic molecules has been studied.[35−48]

The interest of many researchers in the field of gas-phase clusters was first focused on scalable properties concerning a smooth transition from small particles to solids,[49,50] searching for different phase transitions.[51−56] However, in the meantime, it has been fully recognized that the nonscalable properties in the nanosize regime from a few atoms to a considerable number of atoms are of particular importance.[12−15] The nature, size, and structure of the confinement have given rise to many novel and unexpected properties with a large potential for applications in different technologies. Attention has been paid first to the stationary ground state and to the optical properties of gas-phase clusters as a function of their size, and many surprising phenomena have been discovered.[12,16,17,19] Solvation, energy transfer, and reactivity are other aspects which received considerable attention.[14,20,21] In contrast, ultrafast time-resolved studies on clusters[22,23] became available only in the past decade due to advances in conceptual and technical aspects of the femtosecond pump−probe

spectroscopy (compare ref 5 and references therein). The time-resolved ultrafast laser studies carried out on clusters provided findings on the nature and time scales of processes such as conformational changes, internal vibrational energy redistributions (IVRs), charge separation, and Coulomb explosion.[14,21−23] Furthermore, due to advances in laser technology, the femtosecond pulse shapers permitted the manipulation of very short femtosecond laser pulses giving rise to specially designed laser fields which are able to guide molecular dynamics to the desired target such as a given fragmentation channel, a particular isomer, or an aimed reaction product.[11,57−78]

Complementary to experimental developments, the role of theory in the field of cluster research has been essential from a conceptual as well as from a quantitatively predictive point of view. Theory provided information on structural, bonding, reactivity, and optical properties of gas-phase clusters[12,43,44,46,79−103] and allowed one to account for the influence of different media such as solvation,[14,104,105] matrixes,[106−108] and support materials.[29−31,109,110] In particular, the connection between energetic, structural, and electronic properties as a function of the size has been established for gas-phase metallic clusters.[12,16,17] Notice that direct experimental determination of cluster structures in the gas-phase is still very difficult and mostly not available for an arbitrary size and atomic composition. However, indirect information can be obtained from spectroscopic observations. Comparison between theoretical spectra calculated for the stable structures of clusters and experimental data allowed identification of the structures responsible for the observed spectral features.[12,17,98,99] Moreover, the analysis of electronic properties responsible for the characteristic spectroscopic patterns provided a conceptual framework for nonscalable optical properties.[12,79] The influence of temperature in experimental findings[111] has also been elucidated.[79,99] In the case of clusters interacting with different media, the complexity increases and the role of theory to unravel different effects and to establish a connection among them has become increasingly important.[14,29−31,109,110] The situation is particularly demanding if dynamical aspects of clusters are considered. Time-resolved observations are strongly dependent on the setup of experimental conditions such as laser wavelengths, duration of laser pulses and their shapes, competition between one- and many-photon effects, strength of the electric field, and so forth. Here theory has the role not only to provide insight into the nature of time-dependent processes but also to identify the conditions under which they can be observed.[112−125] Consequently, theory is directly involved in conceptual planning of time-resolved experiments. The prominent examples are theoretical proposals of different optical control schemes exploiting laser field parameters in order to manipulate ultrafast processes.[2,126−131] They stimulated control experiments, first on simple systems such as metallic dimers and trimers[132−154] and later on more complex systems[58−60,73,78,155,156−159] which confirmed the conceptual frame of the proposed theoretical schemes outlined in section 2.3.

2.2. Dynamics and Ultrafast Observables

Femtosecond spectroscopy became a powerful technique for the real-time investigation of intra- and intercluster and molecular electronic and nuclear dynamics during the geometric transformation along the reaction coordinate. It is based on the preparation of the transition state of the chemical reaction by the optical excitation of a stable species in a nonequilibrium nuclear configuration in the pump step, and probing its time evolution by laser induced techniques such as fluorescence, resonant multiphoton ionization, or photoelectron spectroscopy. This approach was pioneered by Zewail et al. for bimolecular reactions.[160−162] For an elementary reaction involving breaking of one bond and creation of another one, changes in intermolecular separation of ∼10 Å are observable on a time scale of 1−10 ps. For this purpose, the duration of the probe step must be 10−100 fs if a resolution of ∼0.1 Å has to be achieved. In another approach advanced by Neumark et al. and Lineberger et al., a nonequilibrium or transition state can also be produced by vertical photodetachment of stable negative ions. The transition state of the neutral species can be close to the stable geometry of anions as shown by Neumark et al.,[22,163−171] or it can provide the starting point for the isomerization process in the neutral ground state as illustrated by Lineberger et al.[172−174] The negative ion-to-neutral-to-positive ion (NeNePo) pump−probe experiments introduced by Wöste and his colleagues[175,176] advanced the vertical one-photon detachment technique, allowing probing of structural and isomerization relaxation in neutral clusters as a function of the cluster size.[175] An extension of the NeNePo technique by two-color excitations has been proposed by Lineberger et al.[177] Complementary, time-resolved photoelectron spectroscopy[22] became a powerful technique applicable to clusters as well.[178] Recent developments of time-resolved techniques such as ultrafast electron diffraction[179] and time-domain X-ray absorption[180] allow one to reveal transient molecular structres in chemical reactions of complex systems and in excited states of molecules.

However, the conceptual framework of ultrafast spectroscopy is provided by theory and simulations which allow determination of the time scales and the nature of configurational changes as well as internal energy redistribution (IVR) in vertically excited or ionized states of clusters.[112−117,119,181] The separation of time scales of different processes is essential for identifying them in measured spectral features. Moreover, the distinction between coherent and dissipative IVRs in finite systems can be addressed as a function of the cluster size. For investigation of intra- and intercluster dynamics in fs-spectroscopy, which involves the generation of the initial conditions and multistate dynamics for the time evolution of the system itself and for the probe or the dump step, two basic requirements have to be fulfilled. The first is the use of accurately determined electronic structure in the ground and excited states as a function of all degrees of freedom. In the case that the electronic states involved are well separated, the Born−Oppenheimer approximation is valid and the adiabatic

dynamics is appropriate. In contrast, if avoided crossings and conical intersections between electronic states are present during the geometric and chemical transformation, breakdown of the Born−Oppenheimer approximation occurs and nonadiabatic effects have to be taken into account. This represents an additional theoretical and computational challenge. The second basic requirement is the accurate simulation of ultrafast observables such as pump−probe signals. This involves appropriate treatment of optical transitions such as ultrafast creation and detection of the evolving wave packet or classical ensemble. In the latter case, the dynamics is described by classical mechanics, and the average over trajectories has to be made in order to simulate the spectroscopic observables.

Accurately precalculated global ab initio energy surfaces of ground and excited states have been limited to systems with few atoms for which quantum dynamics of nuclei is feasible. Therefore, investigations of ultrafast dynamics have been carried out for metallic dimers[132,133,136,182−191] and trimers.[192−199] In contrast, for larger systems in general, either a few degrees of freedom can be selected for explicit treatment or model potentials have to be used. Both situations are generally not applicable to elemental clusters, in particular with metallic atoms,[12] since usually they do not contain a "chromophore type" subunit or they do not obey regular growth patterns.[56] An addition of a single atom can produce drastic changes in the properties of their ground and excited states. Therefore, in the majority of cases, all degrees of freedom have to be considered, and semiempirical analytic potentials are usually not suitable, since they do not properly describe structural and electronic properties with changing cluster size. Consequently, first principle (ab initio) molecular dynamics (AIMD) "on the fly", without precalculation of the energy surfaces, represents an appropriate choice to study ultrafast processes in elemental clusters with heavy atoms for which, in the first approximation, the classical description of nuclear motion is acceptable. This method, pioneered by Car and Parrinello[200] and based on the density functional method and plane wave basis sets, was originally introduced for the dynamics in the electronic ground state. The basic idea is to compute forces acting on nuclei from the electronic structure calculations which are carried out "on the fly".[201] Related AIMD methods with plane wave basis sets have also contributed significantly to the success in applications on clusters.[202]

For fast calculations of forces, analytic gradients are needed. They have been developed for geometry optimization in quantum chemistry methods[203−206] at different levels of accuracy and are, therefore, also available for the MD schemes along the molecular dynamics trajectories. Advances in these techniques over the last few years provided an excellent basis for applications of ab initio ground-state classical MD on small and large systems with controllable accuracy, depending on the method used for calculation of the electronic structure (e.g. different versions of density functional methods with atomic basis sets[207,208] or other approaches accounting for the electronic correlation effects[209,210]).

The situation is still very different for ab initio adiabatic and nonadiabatic MD "on the fly" involving excited electronic states. Despite recent efforts and successes,[115,116,211−215] further development of such theoretical methods which combine accurate quantum chemistry methods for electronic structure with MD adiabatic and nonadiabatic simulations "on the fly" has promise to open many new possibilities for successful investigation of fs-processes. This research area will essentially remove borders between quantum chemistry and molecular dynamics communities, although each of them has numerous challenging tasks to be accomplished in order to provide a conceptual frame for fs-chemistry and -physics of molecules and clusters. In this context, very intense research is presently going on along two main avenues. One is to achieve fast calculations of forces in excited states, as well as of nonadiabatic couplings, at the level of theory accounting for electron correlation effects with controllable accuracy which are suitable for implementation in different adiabatic and nonadiabatic MD schemes "on the fly".[215] The second is to introduce quantum effects for the motion of nuclei, particularly in the case of nonadiabatic dynamics,[216−226] in systems with a considerable number of degrees of freedom, allowing for their identification in spectroscopic observables such as fs-signals. For each of these two research areas, excellent reviews are available.[215,217,218,221,227,228]

2.3. Concepts for Control of Ultrafast Processes

The idea to control the selectivity of product formation in a chemical reaction, using ultrashort pulses by the proper choice of their phase or of the time duration and the delay between the pump and the probe (or dump) step, is based on exploitation of the coherence properties of laser radiation due to quantum mechanical interference effects.[126−130,229] First, single-parameter control schemes were proposed. Within the Brumer−Shapiro phase-control scheme,[129,130,229] constructive and destructive interference between different light induced reaction pathways is used in order to favor or to suppress different reaction channels. The other scheme, introduced by Tannor and Rice,[126,127] takes advantage of differences in potential energy surfaces of different electronic states and, therefore, uses the time parameter for control. The pump pulse brings the system to nonequilibrium configurations from which transformations such as bond stretchings take place. If the probe or dump laser is timed properly, different pathways to dissociation of one of the stretched bonds can be achieved. Both single-parameter control schemes were confirmed experimentally.[132−135,190,230−236] Another single-parameter control is a "linear chirp"[237,238] corresponding to a decrease or increase of the frequency as a function of time under the pulse envelope. This was the first step toward shaping the pulses in the framework of so-called many-parameter optimal control theory (OCT). Tannor and Rice have first variationally optimized electric fields.[239] Then the optimal control theory was applied to molecular

problems by Rabitz et al.,[131,240−242] Kosloff et al.,[243] and Rice et al.[244] Technological progress due to fs-pulse shapers allowed manipulation of ultrashort laser pulses.[57,62,63,65,66] Finally, a closed loop learning control (CLL) was introduced by Judson and Rabitz in 1992,[245] opening the possibility to apply optimal control on more complex systems. Since the potential energy surfaces (PESs) of multidimensional systems are complicated and mostly not available, the idea was to combine a fs-laser system with a computer-controlled pulse shaper to produce specific fields acting on the system initiating photochemical processes. After detection of the product, the learning algorithm[57,246,247] was used to modify the field based on information obtained from the experiment and from the objective (the target). The shaped pulses were tested and improved iteratively until the optimal shape for the chosen target was reached. Such a black box procedure is extremely efficient, but it does not provide information about the nature of the underlying processes which are responsible for the requested outcome. The success of the above-mentioned schemes has been demonstrated by control experiments.[58−76,147−152,248] However, any multiparameter optimization scheme has a drawback of having a manifold of local solutions which are reachable depending on initial conditions. Intense research activity is directed toward improvements of these aspects, particularly in the closed loop learning control.[249,250] The application of optimal control theory has a broad spectrum which will not be addressed in its completeness here. This includes research directions such as laser cooling of internal degrees of freedom of molecules and quantum computing (cf. refs 251−255 for examples of metallic dimers), since they require inclusion of additional methodological aspects.

Since tailored laser pulses have the ability to select pathways on the parts of energy surfaces which optimally lead to the chosen target, their analysis should allow one to determine the mechanism of the processes and at the end provide information about important parts of the PES (so-called inversion problem[187,256−259]). Therefore, developments of theoretical methods are needed which allow one to design interpretable optimal laser pulses for complex systems such as clusters or biomolecules, by establishing the connection between the underlying dynamics and their shapes. Until recently, the limitation was imposed by difficulties in precalculating multidimensional surfaces. To avoid this obstacle, ab initio adiabatic and nonadiabatic MD "on the fly" without precalculation of the ground and excited state energy surfaces is particularly suitable provided that an accurate description of the electronic structure is feasible and practicable. Moreover, this approach offers the following advantages. The quantum-classical correspondence between trajectory and wave packet is valid for short pulses and short time propagation. MD "on the fly" can be applied to relatively complex systems, and moreover, it can be implemented directly in the procedures for optimal control. This allows one to identify properties which are necessary for ensuring the controllability of complex systems and to detect mechanisms responsible for the obtained pulse shapes. In the above-mentioned context, the Liouville space formulation of optimal control theory developed by Yan, Wilson, Mukamel, and their collegues,[260−272] in particular its semiclassical limit in the Wigner representation,[121,262] is very suitable despite its limitations. For example, quantum effects such as interference phenomena or tunneling and zero point vibrational energy are not accounted for. The study of clusters with varying size offers an ideal opportunity to test these concepts and methods as well as to investigate conditions under which different processes can be experimentally controlled and observed.

3. Methods for Dynamics in Ultrafast Spectroscopy

In the classification of different theoretical approaches, three important aspects have to be considered. They concern electronic structure methods, dynamics of nuclei, and dynamics of optical transitions. Concerning the first aspect, we focus on ab initio time-dependent quantum chemistry approaches for the ground and excited states, including a nonadiabatic coupling between electronic states if necessary. The dynamics of nuclei can be described by classical trajectories or by quantum dynamics, depending on the atomic composition of the system (heavy or light atoms) and on the choice of questions to be addressed. In contrast, the time-dependent interaction with the light, giving rise to transitions from one electronic state to the other, is of quantum mechanical nature. Therefore, the semiclassical approaches for dynamics in fs-spectroscopy can involve a pure classical description of nuclei as well as different quantum corrections for propagation of nuclei while the electronic structure is described quantum mechanically. In contrast, full quantum mechanical approaches treat dynamics of nuclei and of optical transitions quantum mechanically and are still limited to a small number of degrees of freedom. Moreover, they rely on precalculated energy surfaces. Since in this review we do not address systems for which active and passive degrees of freedom can be separated, neither mixed quantum-classical (hybrid) methods[106] for propagation of nuclei nor methods describing chromophore-environment separation[273−275] will be addressed. We focus on semiclassical approaches, in particular those which can be connected with ab initio MD "on the fly", giving rise to classical trajectories. The full quantum mechanical methods for dynamics will briefly be outlined in connection with their applications to systems with few atoms.

3.1. Time-Dependent Quantum Chemistry

The important starting step in introducing time into quantum chemistry was the implementation of analytic energy gradients for the optimization of the geometries in the ground states which was pioneered by Pulay.[203] In the meantime, the analytic energy gradients are available for numerous wave function based methods[204] as well as for density functional

theory,[276−278] accounting for electron correlation effects at different levels of accuracy. This includes the variational procedures beyond the Hartree−Fock approximation [such as different variants of configuration interaction (CI) methods and the multiconfigurational self-consistent field (MCSCF) procedure] as well as the perturbation approaches [such as many body perturbation theory (MBPT) and the coupled cluster (CC) method].[204] Large progress in this field is characterized by improving efficiency at a high level of accuracy. This allows the computation of forces needed for the ab initio molecular dynamics (AIMD) "on the fly", which couples quantum mechanical treatment of electrons and forces acting on nuclei with classical equations of motion. The first proposal along these lines can be found in an early paper of Leforestier.[201] However, the success of the first principle AIMD "on the fly" was initiated by the Car−Parrinello method,[200] which is based on the density functional method and employs plane waves as basis sets allowing use of Hellmann−Feynman forces. This is computationally considerably less demanding than the calculations of exact Pulay forces[204] in the framework of quantum chemistry methods based on wave function approaches or density functional theory, both employing Gaussian atomic basis sets. Different versions of the Car−Parrinello method (cf. ref 215), as well as implementation of Gaussian basis sets and exact forces at different levels of correlation treatments by a number of groups,[279−283] allowed for an enormous number of applications of ground-state adiabatic MD in different fields. Furthermore, advances in density functional theory (DFT) due to gradient corrected functionals (GDFTs) for exchange and correlation, leading to a more realistic description of the bonding, made the density functional method[284−289] become an established approach in quantum chemistry and in AIMD "on the fly" for the ground states. Although the accuracy of DFT is less controllable than in the case of wave functions based ab initio methods, computational demand is considerably lower.

The MD procedure "on the fly" is very simple; the time evolution of the atoms is simulated by classical trajectories obtained by the numerical solution of Newton's equations of motion. For this purpose, the Verlet algorithm[290] is particularly suitable. According to this algorithm, the position and velocity of the nucleus $i(\mathbf{r}_i,\mathbf{v}_i)$ at time step $t_n = n\Delta t$ are obtained recurrently:

$$\mathbf{r}_i^{(n+1)} = 2\mathbf{r}_i^{(n)} - \mathbf{r}_i^{(n-1)} + \frac{\Delta t^2}{m}\mathbf{F}_i^{(n)} \quad (1)$$

$$\mathbf{v}_i^{(n)} = (\mathbf{r}_i^{(n+1)} - \mathbf{r}_i^{(n)})/(2\Delta t) \quad (2)$$

The force $\mathbf{F}_i^{(n)}$ acting on nucleus i is related to the gradients of the total molecular energy computed, for example, at the GDFT level. In AIMD-GDFT procedures the ground-state electronic wave function and energy are computed at each time step (i.e. for each geometric configuration). The electronic energy obtained from an iterative Kohn−Sham procedure contributes to the total potential energy, and the forces acting on the nuclei are determined as corresponding derivatives. The MD can be carried out either at constant total energy or at constant temperature. To achieve the conservation of these quantities, the high accuracy of calculated forces is mandatory. This requirement necessarily increases computational demand.

Originally, most applications were focused on the search of structures. In this case, the advantage of AIMD with respect to the gradient methods for geometry optimization is that all local minima can, in principle, be accessed. Thus, for example, the cluster geometries generated along the classical trajectories at high temperatures can be used as starting points in the search of isomeric forms on the potential energy surfaces. Moreover, the applications of AIMD were extended to studies of temperature-dependent properties such as isomerization effects[281−283,291] and finally became extremely useful for exploring ultrafast processes.[79,115−122,292−294]

The situation is still different for the description of excited states, particularly in connection with MD "on the fly". This requires more demanding treatment of electron correlation effects, taking into account large bonding rearrangements specific for the given excited state. In this context, single-reference correlation methods, such as CI with single and double excitations (CISD) or coupled cluster with single and double excitations (CCSD), can often be inadequate, since they suffer from lack of multireference character. For example, a Slater determinant with a double excitation can have a leading role in a CI expansion of a given excited state. The latter can be introduced by choosing the adequate set of reference configurations and performing single and double excitations with respect to all of them by the MRCI procedure. The other possibility is to carry out MCSCF calculations, which allow for improvement of the quality of the molecular orbitals, and to take electron correlation effects into account simultaneously. The complete active space SCF (CASSCF) is a special case of MCSCF in which a full CI procedure (complete optimization of both MO and CI spaces) is performed within the limited orbital set called active space.[295−297] The problem with these methods is determination of several roots of different symmetries. This is not straightforward, because of possible root switching occurring due to changes in the geometric configurations, and it can, in particular, be inconvenient in connection with MD "on the fly". Another alternative is given by the generalized valence bond (GVB) theory, in which contributions of covalent and ionic states are treated at equal footing. In the framework of these wave function methods, the analytic gradients for excited states are available for various Hartree−Fock based schemes,[115,116] generalized valence bond (GVB),[298−302] multiconfiguration self-consistent field (MCSCF),[204,303] complete active spaces SCF (CASSCF),[304−306] and truncated (CIS)[307] and full configuration interaction (CI) methods.[308] Most of them are also implemented in different quantum chemistry programs.[309−311]

The other class of methods for which the gradients in excited states are available belongs to linear

response approaches based on time-dependent perturbation theory. The simplest approximation can be obtained by taking HF wave functions as a reference and including only single excitations and interactions of double excitations with the ground state called deexcitations, leading to the random phase approximation (RPA).[211,213] Therefore, the RPA method gives rise only to accurate results for excited states which are dominated by singly-excited configurations. Moreover, due to some contributions of the double excitations, the results are better than those obtained from CI with single excitations only (CIS). The reference function can be improved by using the MCSCF wave function instead of the HF one or by including higher order excitation operators. To achieve better accuracy, linear response methods based on the coupled cluster reference wave function have been developed in the framework of the equation of motion methods (EOM-CCSD).[312,313] The computational demand of the EOM-CCSD method is large, since each excited state requires more than 50% of the ground-state CCSD calculation. To reduce the computational demand, the similarity transformed equation of motion coupled cluster (STEOM-CC) method, which reduces the coupling between the singly-excited determinants and those with higher excitations, has been introduced.[314] The methods such as the RPA and EOM-CCSD, which are based on the linear response formulation, have advantages to allow for the calculations of many excited states at once. However, since both of them use a single-reference function, the former one a Hartree−Fock single determinant and the latter one a correlated CCSD wave function, they do not allow for accurate description of excited states dominated by double excitations. Very recent developments such as implementation of analytic gradients for excited states for the approximate coupled-cluster singles and doubles model (CC2) employing the resolution-of-the-identity (RI) approximation for electron repulsion integrals represent a promising trend[214] to decrease the computational time and to provide a relatively accurate description for excitation energies. However, these methods are also based on a single-reference wave function and exclude an appropriate description of a number of photochemical processes which require multireference treatment.[315−317] Formulation of analytic gradients in excited states for a multireference wave function is also available in the framework of the direct CI method.[318,319] Calculations of gradients in excited states and forces for MD "on the fly" using highly correlated quantum chemistry methods are still computationally extremely demanding. Further development is needed, particularly in lowering the computational demand of MRCI methods in order to apply them in MD "on the fly" for excited states.

Another type of approach based on DFT is the time-dependent density functional linear response (TD-DFT),[211−213] which also belongs to linear response approaches. This method, in particular with the use of relatively accurate exchange-correlation functionals, has been applied for calculation of excitation spectra and other properties in the frequency domain.[213] Analytic formulation of gradients in excited states in the framework of TD-DFT also became recently available, allowing one to carry out adiabatic AIMD "on the fly" in the excited states, but still for relatively small systems.[211−213] The results are expected to be more accurate for the low excited states than for the energetically higher lying ones and for those in which single-reference character prevails. Therefore, the further development of reliable functionals for excited states is needed, and multireference contribution to the excited states in the framework of the DFT method requires future development. Also, Car−Parrinello MD simulations for excited states, based on the restricted open shell Kohn−Sham formulation and TD-DFT using the adiabatic local density approximation (ALDA) and the plane wave basis set with pseudopotentials, have been formulated. Different test calculations have been performed, and the field is in a promising stage of development (for details, cf. ref 215).

First principle theoretical treatment of nonadiabatic dynamics beyond model systems requires a double task: that is to solve the problem of coupling among electronic states and to treat nonadiabaticity. Concerning the first aspect, either an adiabatic or diabatic representation can be chosen. The first diagonalizes the potential energy, and the second diagonalizes approximately the kinetic energy of nuclei. The diabatic representation gives rise to smoother potential energy surfaces. The adiabatic representation requires the calculations of nonadiabatic couplings between the electronic states. In the case that their analytic formulation is available, the implementation in procedures for nonadiabatic dynamics "on the fly" is straigthforward, allowing one to calculate simultaneously energy surfaces and nonadiabatic couplings for systems with a considerable number of degrees of freedom. This is possible in the framework of HF based methods,[116] CASSCF,[304−306,320−322] and recently for different levels of the CI method.[318,319]

Time-dependent density functional theory in the time domain accounting for nonadiabatic effects has been developed until now in two directions. The first one could be called Ehrenfest molecular dynamics based on Kohn−Sham density functional theory.[323−328] The second one is in the framework of the Car−Parrinello approach, which includes computation of nonadiabatic coupling elements based on the orbital velocities available within this method.[215,329]

Another recent development of nonadiabatic dynamics "on the fly" is based on the analytical formulation of gradients for semiempirical CI wave functions with floating occupation molecular orbitals.[330] The time-dependent electronic wave function is then propagated by means of a local diabatization algorithm.[331] The fractional occupation SCF plus CI technique is adequate for description of bond breaking and orbital degeneracies and treatment of several electronic states on equal footing. This is particularly important for an appropriate description of photochemical processes.[332−334] However, the accuracy of such methods depends on the quality of the parametrization, which is easier to obtain for second and for third row atoms than for heavier elements. These

approximate methods are promising for applications to larger systems.

3.2. Semiclassical Multistate Nuclear Dynamics and fs-Signals

Semiclassical methods for dynamics combine classical mechanics and quantum mechanics. They are particularly attractive for obtaining insight into complex systems with heavy atoms for which full quantum mechanical treatment of dynamics is not mandatory and is usually prohibitive due to their size. Semiclassical methods for dynamics, which make use of classical trajectories with quantized initial conditions, are suitable for applications to such systems. However, the approaches which are able to include the quantum coherence[216] and tunneling[217,335,336] effects into classical MD approximately are very valuable and inevitable for the description of some processes (e.g. motion of light atoms such as proton transfer). Moreover, all the processes which involve transitions between different electronic states require quantum mechanics for the adiabatic or the nonadiabatic dynamics and should in some manner be incorporated consistently with the dynamics of nuclei. Semiclassical methods which contain the superposition of probability amplitudes are therefore capable of providing an approximate description of quantum effects in molecular dynamics[221] (interference, tunneling, etc.). Classical MD in different forms, including ab initio MD "on the fly", is now applicable to relatively large systems, and classical trajectories can be used as inputs in semiclassical approaches for simulations of observables. Moreover, in principle, it is also possible to add quantum effects to classical MD simulations "on the fly".[335,336] Therefore, we focus on the approaches which are able to make use of classical adiabatic and nonadiabatic AIMD and time-dependent quantum chemistry.

The time evolution of the density operator $\hat{\rho}(t)$ is given by the quantum mechanical Liouville−von Neumann equation

$$i\hbar \frac{\partial \hat{\rho}}{\partial t} = [\hat{H}, \hat{\rho}] \tag{3}$$

where $\hat{H}$ is the Hamiltonian of the system. This offers an appropriate starting point for establishing semiclassical approaches. Equation 3 has a well-known classical limit in the case of the nuclear dynamics on a single electronic surface, corresponding to the classical Liouville equation of nonequilibrium statistical mechanics:

$$\frac{\partial \rho}{\partial t} = \{H, \rho\} \tag{4}$$

Here $\rho = \rho(\mathbf{q},\mathbf{p},t)$ and $H = H(\mathbf{q},\mathbf{p},t)$ are functions of classical phase space variables ($\mathbf{q}$, $\mathbf{p}$), and

$$\{H, \rho\} = \frac{\partial H}{\partial \mathbf{q}}\frac{\partial \rho}{\partial \mathbf{p}} - \frac{\partial \rho}{\partial \mathbf{q}}\frac{\partial H}{\partial \mathbf{p}} \tag{5}$$

is the Poisson bracket. The classical limit can be derived from eq 3 by means of a Wigner−Moyal expansion[337−339] of the quantum mechanical Liouville−von Neumann equation in terms of $\hbar$, which emerges from the replacement of the commutator by the Poisson bracket if the expansion is terminated to the lowest order of $\hbar$:

$$[\hat{A}, \hat{B}] \rightarrow i\hbar\{A, B\} + O(\hbar^3) \tag{6}$$

Higher order terms in $\hbar$ serve for introduction of quantum effects in the dynamics.

The semiclassical limit of the Liouville formulation of quantum mechanics, based on the Wigner−Moyal representation of the vibronic density matrix, offers a methodological approach suited for accurate treatment of ultrafast multistate molecular dynamics and pump−probe spectroscopy using classical trajectory simulations.[112,113,115,116,340] This approach is characterized by the conceptual simplicity of classical mechanics and by the ability to approximately describe quantum phenomena such as optical transitions by means of the averaged ensemble over the classical trajectories. Moreover, the introduction of quantum corrections can be made in a systematic manner. The method requires drastically less computational afford than full quantum mechanical calculations, it provides physical insight in ultrafast processes, and it is applicable to complex systems. Additionally, it can be combined directly with quantum chemistry methods for electronic structure to carry out the multistate dynamics at different levels of accuracy including precalculated energy surfaces as well as the ab initio MD "on the fly", which will be addressed separately later. The approach is related to the Liouville space theory of nonlinear spectroscopy in the density matrix representation developed by Mukamel and his colleagues (cf. ref 341). Following the proposal by Martens et al.[340] and our own formulation,[112,113,115,116] the method is briefly outlined in connection with its application to simulations of the time-resolved pump−probe or pump−dump signals, involving first adiabatic and then nonadiabatic dynamics.

3.2.1. Adiabatic Dynamics

The Hamiltonian of a molecular system represented in terms of adiabatic electronic states which is coupled to an electromagnetic field $\epsilon(t)$ can be written as

$$\hat{H} = \hat{H}_{\mathrm{mol}} + \hat{H}_{\mathrm{int}} \equiv \sum_a |a\rangle \hat{h}_a(\mathbf{Q})\langle a| - \epsilon(t)\Big(\sum_{a,b} |a\rangle \hat{\mu}_{ab}(\mathbf{Q})\langle b| + h.c.\Big) \tag{7}$$

with the vibrational Hamiltonian $\hat{h}_a(\mathbf{Q})$ of the adiabatic electronic state a, the collection of vibrational coordinates $\mathbf{Q}$, and the dipole approximation for interaction with the electromagnetic field. The matrix elements of a quantum mechanical operator $\hat{A}(t)$ in the real space representation are given by $A(\mathbf{Q},\mathbf{Q}',t) \equiv \langle \mathbf{Q}|\hat{A}(t)|\mathbf{Q}'\rangle$. Introducing the center of mass coordinate $\mathbf{q} = (\mathbf{Q} + \mathbf{Q}')/2$ and the relative coordinate $\mathbf{s} = \mathbf{Q} - \mathbf{Q}'$, the Wigner transform $A(\mathbf{q},\mathbf{p},t)$ of the operator $\hat{A}(t)$ is defined as

$$A(\mathbf{q},\mathbf{p},t) = \frac{1}{2\pi\hbar}\int_{-\infty}^{\infty} d\mathbf{s}\, e^{-i\mathbf{p}\mathbf{s}/\hbar} A\Big(\mathbf{q}-\frac{\mathbf{s}}{2},\mathbf{q}+\frac{\mathbf{s}}{2},t\Big) \tag{8}$$

The dynamics of the system in the Wigner approach[112] is characterized by Wigner distributions $P_{ab}(\mathbf{q},\mathbf{p},t)$. They are defined as the Wigner transform of the vibrational density matrix elements $\hat{\rho}_{ab}(\mathbf{Q},\mathbf{Q}',t) \equiv \langle a|\langle \mathbf{Q}|\hat{\rho}(t)|\mathbf{Q}'\rangle|b\rangle$. From this definition, the physical meaning of the Wigner distributions is straightforward. The diagonal elements $P_{aa}(\mathbf{q},\mathbf{p},t)$ are the occupation densities of the electronic state a whereas the off-diagonal elements $P_{ab}(\mathbf{q},\mathbf{p},t)$ $(a \neq b)$ determine the transition probabilities from the electronic state a to the state b.

The equation of motion for the Wigner distributions can be obtained by transforming the exact quantum mechanical Liouville−von Neumann equation for the density operator, which takes the following form for the vibronic density matrix:

$$i\hbar \frac{\partial \hat{\rho}_{ab}}{\partial t} = \hat{h}_a \hat{\rho}_{ab} - \hat{\rho}_{ab}\hat{h}_b - \epsilon(t)\sum_c (\hat{\mu}_{ac}\hat{\rho}_{cb} - \hat{\rho}_{ac}\hat{\mu}_{cb}) \quad (9)$$

The intramolecular dynamics is determined by the vibrational Hamiltonians $\hat{h}_a$ and $\hat{h}_b$ and is described by the first two terms on the right-hand side (rhs) of eq 9. The simulation of pump−probe and pump−dump signals requires the explicit consideration of the coupling to the external optical field, which is given by the last term on the rhs of eq 9. The Condon approximation was assumed, imposing a constant transition dipole moment, and $\hat{\mu}_{ac}$ labels the electronic transition dipole moment. From eq 9, the equation of motion for transition probability P_{ab} emerges:

$$\begin{aligned} i\hbar\frac{\partial P_{ab}(\mathbf{q},\mathbf{p},t)}{\partial t} &= h_a(\mathbf{q},\mathbf{p}) \exp\left(\frac{\hbar}{2i}\overleftrightarrow{T}\right) P_{ab}(\mathbf{q},\mathbf{p},t) - \\ & P_{ab}(\mathbf{q},\mathbf{p},t) \exp\left(\frac{\hbar}{2i}\overleftrightarrow{T}\right) h_b(\mathbf{q},\mathbf{p}) + \\ & \epsilon(t)\sum_c^{a\neq c} (\mu_{ac}P_{cb}(\mathbf{q},\mathbf{p},t) - P_{ac}(\mathbf{q},\mathbf{p},t)\mu_{cb}) \quad (10) \end{aligned}$$

where

$$\overleftrightarrow{T} = \frac{\overleftarrow{\partial}}{\partial \mathbf{q}}\frac{\overrightarrow{\partial}}{\partial \mathbf{p}} - \frac{\overleftarrow{\partial}}{\partial \mathbf{p}}\frac{\overrightarrow{\partial}}{\partial \mathbf{q}} \quad (11)$$

The description of optical excitation processes within the framework of Wigner distributions is represented by eq 10. Due to the highly nonlinear derivatives with respect to coordinates and momenta, this expression is too complicated for practical calculations without introducing further approximations.

Classical Limit and Weak Field. Using a $\hbar$-expansion of the exponentials in eq 10 and restricting to the lowest order, the "classical limit" is obtained. In the case that statistically averaged quantities of finite temperature are calculated, this expansion is justified, as pointed out by Heller.[342,343] Moreover, this formalism allows for a systematic introduction of quantum corrections to the classical behavior of the system.

The coupling to the electromagnetic field can also be simplified. The assumption that the field is weak enough in intensity allows one to expand the Wigner distribution in a perturbation series, written as $P_{ab} = \sum_i P_{ab}^{(i)}$, where the subscript i indicates the order in the field. Therefore, in the "classical limit" and for weak fields, the equations hold for the transition probabilities $(a \neq b)$:

$$\begin{aligned} i\hbar \frac{\partial P_{ab}^{(i)}(\mathbf{q},\mathbf{p},t)}{\partial t} &= (h_a(\mathbf{q},\mathbf{p}) - h_b(\mathbf{q},\mathbf{p}))P_{ab}^{(i)}(\mathbf{q},\mathbf{p},t) + \\ & \epsilon(t)\sum_c^{a\neq c}(\mu_{ac}P_{cb}^{(i-1)}(\mathbf{q},\mathbf{p},t) - P_{ac}^{(i-1)}(\mathbf{q},\mathbf{p},t)\mu_{cb}), \\ & a \neq b \quad (12) \end{aligned}$$

and for the occupation densities $(a = b)$

$$\begin{aligned} i\hbar \frac{\partial P_{aa}^{(i)}(\mathbf{q},\mathbf{p},t)}{\partial t} &= \frac{\hbar}{i}\left\{\frac{\partial h_a(\mathbf{q},\mathbf{p})}{\partial \mathbf{q}}\frac{\partial P_{aa}^{(i)}(\mathbf{q},\mathbf{p},t)}{\partial \mathbf{p}} - \right. \\ & \left. \frac{\partial h_a(\mathbf{q},\mathbf{p})}{\partial \mathbf{p}}\frac{\partial P_{aa}^{(i)}(\mathbf{q},\mathbf{p},t)}{\partial \mathbf{q}}\right\} + \\ & \epsilon(t)\sum_c^{a\neq c}(\mu_{ac}P_{ca}^{(i-1)}(\mathbf{q},\mathbf{p},t) - P_{ac}^{(i-1)}(\mathbf{q},\mathbf{p},t)\mu_{ca}) \quad (13) \end{aligned}$$

Assuming the initial conditions $P_{ab}^{(0)}(\mathbf{q},\mathbf{p},t=0) = P_{ab}^{(0)}(\mathbf{q},\mathbf{p})$ for the Wigner distributions, and $\mathbf{q}_a(t=0;\mathbf{q}_{a0}) = \mathbf{q}_{a0}$ and $\mathbf{p}_a(t=0;\mathbf{p}_{a0}) = \mathbf{p}_{a0}$ for coordinates and momenta, respectively, eqs 12 and 13 can be iteratively solved

$$\begin{aligned} P_{ab}^{(i)}(\Gamma,t) &= \frac{1}{i\hbar}\int_0^t \mathrm{d}t_1 \exp\left[-\frac{i}{\hbar}V_{ab}(\Gamma)(t-t_1)\right] \times \\ & \epsilon(t_1)\sum_c^{a\neq c}[\mu_{ac}P_{cb}^{(i-1)}(\Gamma,t_1) - P_{ac}^{(i-1)}(\Gamma,t_1)\mu_{cb}], \\ & a \neq b \quad (14) \end{aligned}$$

$$\begin{aligned} P_{aa}^{(i)}(\Gamma,t) &= \frac{1}{i\hbar}\int \mathrm{d}\Gamma_{a0} \int_0^t \mathrm{d}t_2\, \delta(\Gamma - \Gamma_a(t-t_2;\Gamma_{a0})) \times \\ & \epsilon(t_2)\sum_d^{d\neq a}[\mu_{ad}P_{da}^{(i-1)}(\Gamma_{a0},t_2) - P_{ad}^{(i-1)}(\Gamma_{a0},t_2)\mu_{da}] \quad (15) \end{aligned}$$

with the abbreviation $\Gamma = \{\mathbf{q},\mathbf{p}\}$ and the definition $\delta(\Gamma - \Gamma_a(t-t_2;\Gamma_{a0})) \equiv \delta(\mathbf{q} - \mathbf{q}_a(t-t_2;\mathbf{q}_{a0}))\, \delta(\mathbf{p} - \mathbf{p}_a(t-t_2;\mathbf{p}_{a0}))$. The energy gap between the electronic states a and b is given by the quantity $V_{ab}(\Gamma) \equiv h_a(\Gamma) - h_b(\Gamma)$. By inserting eq 14 into eq 15, the final expression for the occupation densities P_{aa} of the electronic state a reads

$$\begin{aligned} P_{aa}^{(i)}(\Gamma,t) &= \frac{1}{\hbar^2}Re\int \mathrm{d}\Gamma_{a0} \int_0^t \mathrm{d}t_2 \int_0^{t_2}\mathrm{d}t_1\, \delta(\Gamma - \Gamma_a(t- \\ & t_2;\Gamma_{a0}))\, \epsilon(t_2)\, \epsilon(t_1)\sum_{c,d}\mu_{ad}(\mu_{dc}P_{ca}^{(i-2)}(\Gamma_{a0},t_1) - \\ & P_{dc}^{(i-2)}(\Gamma_{a0},t_1)\mu_{ca}) \exp\left[-\frac{i}{\hbar}V_{da}(\Gamma_{a0})(t_2 - t_1)\right] \quad (16) \end{aligned}$$

Equation 16 allows one to calculate time-dependent optical spectra. In context with time-resolved spectroscopy with ultrashort laser pulses, a further

specification of the pulse by a Gaussian envelope $\epsilon(t) = \exp[-t^2/2\sigma^2]\cos\omega t$ centered around the laser frequency ω can be introduced in eq 16. The product of the laser pulses with short durations σ can be approximated by

$$\begin{aligned}\epsilon(t_1)\,\epsilon(t_2) &= \exp\left(-\frac{t_1^2}{2\sigma^2}\right)\exp\left(-\frac{t_2^2}{2\sigma^2}\right)\cos\omega t_1\cos\omega t_2\\ &= \exp\left(-\frac{(t_1-t_2)^2}{4\sigma^2}\right)\times\\ &\qquad\exp\left(-\frac{(t_1+t_2)^2}{4\sigma^2}\right)\cos\omega t_1\cos\omega t_2\\ &\approx \exp\left(-\frac{t_2^2}{\sigma^2}\right)\times\\ &\qquad\exp\left(-\frac{(t_1-t_2)^2}{4\sigma^2}\right)\cos\omega t_1\cos\omega t_2\\ &\equiv I(t_2)\exp\left(-\frac{(t_1-t_2)^2}{4\sigma^2}\right)\cos\omega t_1\cos\omega t_2\end{aligned} \tag{17}$$

Using the variable transformation

$$\tau_1 = t - t_2 \tag{18}$$

$$\mathrm{t}_a = t_2 - t_1 \tag{19}$$

in eq 17 and the rotating wave approximation (RWA), the density distribution of eq 16 takes the following form:

$$\begin{aligned}P_{aa}^{(i)}(\Gamma,t) = \frac{1}{\hbar^2}\int \mathrm{d}\Gamma_{a0}\int_0^t \mathrm{d}\tau_1\int_0^{t-\tau_1}\mathrm{d}\tau_\alpha\,\delta(\Gamma -\\ \Gamma_a(\tau_1;\Gamma_{a0}))\,I(t-\tau_1)\sum_{c,d}\mu_{ad}(\mu_{dc}P_{ca}^{(i-2)}(\Gamma_{a0},t-\tau_1-\tau_\alpha) -\\ P_{dc}^{(i-2)}(\Gamma_{a0},t-\tau_1-\tau_\alpha)\mu_{ca})\times\\ \exp\left[-\frac{i}{\hbar}(\hbar\omega - V_{da}(\Gamma_{a0}))\tau_\alpha\right]\exp\left[-\frac{\tau_\alpha^2}{4\sigma^2}\right]\end{aligned} \tag{20}$$

For short pulse durations σ the Gaussian ($\exp[-\tau_\alpha^2/4\sigma^2]$) in eq 20 is strongly localized. Thus, the upper limit $t - \tau_1$ of the integration variable τ_α can be set up to infinity. This allows for an analytic integration of the exponential part of eq 20, which yields the Gaussian spectral distribution determined by the pulse duration σ:

$$\begin{aligned}P_{aa}^{(i)}(\Gamma,t) = \frac{1}{\hbar^2}\int \mathrm{d}\Gamma_{a0}\int_0^t \mathrm{d}\tau_1\,\delta(\Gamma-\Gamma_a(\tau_1;\Gamma_{a0})\times\\ I(t-\tau_1)\sum_{c,d}\mu_{ad}(\mu_{dc}P_{ca}^{(i-2)}(\Gamma_{a0},t-\tau_1) -\\ P_{dc}^{(i-2)}(\Gamma_{a0},t-\tau_1))\mu_{ca})\exp\left[-\sigma^2\frac{(\hbar\omega - V_{da}(\Gamma_{a0}))^2}{\hbar^2}\right]\end{aligned} \tag{21}$$

Equation 21 allows one to calculate more general time-resolved optical signals which are determined by the occupation density of the electronic states and are not limited to the first-order fields (cf. also ref 340).

Assuming that the pump and the probe processes are both of the first order in the fields, eq 21 can be applied only twice ($i = 2$) to calculate the occupation densities $P_{11}^{(2)}(\mathbf{q},\mathbf{p},t)$ and $P_{22}^{(2)}(\mathbf{q},\mathbf{p},t)$ of states 1 and 2, respectively. For the occupation of the probe state $P_{22}^{(2)}(t)$, the following expression holds:

$$\begin{aligned}P_{22}^{(2)}(t) = \int \mathrm{d}\mathbf{q}\,\mathrm{d}\mathbf{p}\,P_{22}^{(2)}(\mathbf{q},\mathbf{p},t) \sim\\ \int \mathrm{d}\mathbf{q}_0\,\mathrm{d}\mathbf{p}_0\int_0^t \mathrm{d}\tau_2\int_0^{t-\tau_2}\mathrm{d}\tau_1\times\\ \exp\left[-\sigma_{\mathrm{pr}}^2\frac{[\hbar\omega_{\mathrm{pr}} - V_{21}(\mathbf{q}_1(\tau_1;\mathbf{q}_0,\mathbf{p}_0))]^2}{\hbar^2}\right]\times\\ \exp\left[-\sigma_{\mathrm{pu}}^2\frac{[\hbar\omega_{\mathrm{pu}} - V_{10}(\mathbf{q}_0,\mathbf{p}_0)]^2}{\hbar^2}\right]\times\\ I_{\mathrm{pu}}(t-\tau_1-\tau_2)\,I_{\mathrm{pr}}(t-\tau_2-t_{\mathrm{d}})\,P_{00}(\mathbf{q}_0,\mathbf{p}_0)\end{aligned} \tag{22}$$

where dipole matrix elements are assumed to be constant. The indices pu and pr label the corresponding parameters of the pump and the probe field, respectively, and t_{d} denotes the time delay.

Since the integration over the pump−probe correlation function can be carried out explicitly,

$$\begin{aligned}\int_0^\infty \mathrm{d}t_2\,I_{\mathrm{pu}}(t-\tau_1-\tau_2)\,I_{\mathrm{pr}}(t-\tau_2-t_{\mathrm{d}}) =\\ \frac{\tilde{\epsilon}_{\mathrm{pu}}^2\tilde{\epsilon}_{\mathrm{pr}}^2}{\sqrt{\pi}\sqrt{\sigma_{\mathrm{pu}}^2+\sigma_{\mathrm{pr}}^2}}\exp\left\{-\frac{(\tau_1-t_{\mathrm{d}})^2}{\sigma_{\mathrm{pu}}^2+\sigma_{\mathrm{pr}}^2}\right\}\end{aligned} \tag{23}$$

the transient photoionization signal can be calculated according to

$$\begin{aligned}S[t_{\mathrm{d}}] = \lim_{t\to\infty}P_{22}^{(2)}(t)\\ \approx \int \mathrm{d}\mathbf{q}_0\,\mathrm{d}\mathbf{p}_0\int_0^\infty \mathrm{d}\tau_1\exp\left\{-\frac{(\tau_1-t_{\mathrm{d}})^2}{\sigma_{\mathrm{pu}}^2+\sigma_{\mathrm{pr}}^2}\right\}\times\\ \exp\left\{-\frac{\sigma_{\mathrm{pr}}^2}{\hbar^2}[\hbar\omega_{\mathrm{pr}} - V_{21}(\mathbf{q}_1(\tau_1;\mathbf{q}_0,\mathbf{p}_0))]^2\right\}\times\\ \exp\left\{-\frac{\sigma_{\mathrm{pu}}^2}{\hbar^2}[\hbar\omega_{\mathrm{pu}} - V_{10}(\mathbf{q}_0,\mathbf{p}_0)]^2\right\}P_{00}(\mathbf{q}_0,\mathbf{p}_0)\end{aligned} \tag{24}$$

For the pump−probe signal, the following information is obtained from eq 24. At the beginning, the system is prepared in the electronic ground state (0) where the corresponding Wigner distribution $P_{00}(\mathbf{q}_0,\mathbf{p}_0)$ is assumed to be known (initial condition). This initial phase space density is spectrally filtered during the pump process into state 1 by the third Gaussians of eq 24. Subsequently, the filtered ensemble propagates on state 1 and is spectrally filtered again during the delayed probe pulse into state 2. This is expressed by the second Gaussians in eq 24.

It is important to notice that the Gaussian form of spectra during the pump and probe process is a direct consequence of both the classical approximation given by eq 12 and the short time assumption expressed by eq 17. The final time resolution of the signal is determined by the pump−probe autocorrelation function given by the first Gaussians in the eq 24. Equation 24 can also be used for calculation of the pump−dump signal by replacing σ_{pr} by σ_{du}, $\hbar\omega_{pr}$ by $\hbar\omega_{du}$, and V_{21} by V_{01}, which is the energy gap between the ground and the excited electronic states.

In the framework of the Wigner representation, a summation over an ensemble of initial conditions is required. It can be naturally determined from the initial vibronic Wigner distribution $P_{00}^{(0)}$ on the electronic ground state. For this purpose, the Wigner distribution of a canonical ensemble in each of the normal modes is computed. This allows one to include temperature effects in correspondence with the experimental situations and to take into account the quantum effects of the initial ensemble at low temperatures.

In the analytic form of signals, given by eq 24, quantum coherence effects are not taken into account, which is a consequence of the classical approximation. Thus, the signals can be simulated by an ensemble of independent classical trajectories where, of course, all anharmonic contributions are fully included but quantum effects such as tunneling or zero point energy are not incorporated. Classical trajectories can be obtained either from precalculated surfaces or from ab initio dynamics "on the fly", allowing one to carry out simulations for systems with a relatively large number of degrees of freedom.

Quantum Corrections. To include the nonlocality of quantum mechanics, a proposal[335] has been recently made to include the nonclassical interactions between the members of the ensemble of trajectories, giving rise to entangled trajectory molecular dynamics.[335,336] This involves a power series expansion of the Wigner function $\rho_w(\mathbf{q},\mathbf{p},t)$ to the third order (cf. eq 6)

$$\frac{\partial \rho_w}{\partial t} = -\frac{p}{m}\frac{\partial \rho_w}{\partial q} + h_a'\frac{\partial \rho_w}{\partial p} - \frac{\hbar^2}{24}h_a'''\frac{\partial^3 \rho_w}{\partial p^3} + \ldots$$

$$= \{h_a, \rho_w\} - \frac{\hbar^2}{24}h_a'''\frac{\partial^3 \rho_w}{\partial p^3} + \ldots \qquad (25)$$

For the precalculated surfaces the third derivative of the vibronic Hamiltonian for the given electronic state is straightforward to obtain. For the dynamics "on the fly", the analytic formulation of the third derivative in the framework of HF and MCSCF methods is available,[204] but their implementation and application have not been accomplished yet. An alternative approach has been introduced by the quantum trajectory method based on the hydrodynamics formulation of quantum mechanics.[344−348] It remains to show how these approaches can be made computationally efficient for future applications.

3.2.2. Nonadiabatic Dynamics

To address nonadiabatic transitions in complex systems involving avoided crossings and conical intersections between electronic states, semiclassical methods based on ab initio multistate nonadiabatic dynamics are suitable for the simulation of fs pump−probe signals. For this purpose, in addition to the calculation of forces in the electronic ground and excited states, the computation of coupled electronic states "on the fly" in the adiabatic or diabatic representation is required. Furthermore, the choice of the approach to nonadiabatic dynamics must be made. These ingredients can then be combined with the Wigner−Moyal representation of the vibronic density matrix which allows one to determine the fs-signals. The electronic part, concerning ab initio calculations of forces in the excited states and nonadiabatic couplings, will be addressed in section 4.3 in the context of specific applications. The research direction involving approaches to nonadiabatic dynamics deserves a separate review article (cf. ref 215).

Since we consider the systems with all degrees of freedom, the most simple choice of treatment of the nonadiabatic dynamics is limited either to the classical path methods or to surface hopping methods.[349] They are characterized by problems arising from the approximations that the trajectories propagate in the mean potential or in the state specific potential, respectively.[350−352] In general, nonadiabaticity involves changes in the population of adiabatic states with changing nuclear configurations. In this way, electronic distribution influences trajectories. The simplest way to include such electron−nuclei feedback is to use the mean field (Ehrenfest) method. It is assumed that the system evolves on an effective potential which can be obtained as an average over adiabatic states weighted by their state populations. The problem with this approach is that the system, which was prepared initially in a pure adiabatic state, will be in a mixed state after leaving the nonadiabatic region. Therefore, the adiabatic nature of the involved states disappears even in the asymptotic region.[215] Moreover, the microscopic reversibility is not preserved (cf. ref 215). Improvement to the Ehrenfest method is to include decoherence, assuming that trajectories finish in a pure state after leaving the region of coupled states. This is possible by introducing the continuous surface switching (CSS) procedure.[218]

In contrast, the basic feature of the surface hopping methods is that the propagation is carried out on one of the pure adiabatic states, which is selected according to its population, and the average over the ensemble of trajectories is performed. The molecular dynamics with quantum transitions (MDQT) version of the fewest-switches surface hopping method, as introduced by Tully,[349] is based on the assumption that the fraction of trajectories on each surface is equivalent to the corresponding average quantum probability determined by coherent propagation of quantum amplitude. Moreover, a choice between adiabatic and diabatic representation has to be made. In the former case, the nonadiabatic couplings have to be calculated, and in the latter case, the overlap

between the wave functions of two states is needed in the framework of the method used for calculations of the electronic structure. For example, the MD as well as nonadiabatic couplings calculated "on the fly" can be directly connected with MDQT and then used to simulate fs-signals. Therefore, we briefly outline the concept involving the adiabatic representation.

The time-dependent wave function $\Psi(t,\mathbf{r},\mathbf{R})$, which describes the electronic state at time t, is expanded in terms of the adiabatic electronic basis functions ψ_j of the Hamiltonian with complex valued time-dependent coefficients

$$\Psi(t,\mathbf{r},\mathbf{R}) = \sum_{j=0}^{M} c_j(t)\ \psi_j(\mathbf{r};\mathbf{R}) \tag{26}$$

The adiabatic states are also time-dependent through the classical trajectory $R(t)$. Substitution of this expansion into the time-dependent Schrödinger equation, multiplication by ψ_k from the left, and integration over $\mathbf{r}$ yields a set of linear differential equations of the first order for the expansion coefficients which are equations of motion for the quantum amplitudes:

$$\mathrm{i}\dot{c}_k(t) = \sum_j [\epsilon_j \delta_{kj} - \mathrm{i}\dot{\mathbf{R}}(t)\cdot\langle\psi_k|\nabla_{\mathbf{R}}|\psi_j\rangle] c_j(t) \tag{27}$$

Here ϵ_j are the eigenvalues of the Hamiltonian, and $\langle\psi_k|\nabla_{\mathbf{R}}|\psi_j\rangle$ are nonadiabatic couplings.

The system of eq 27 has to be solved simultaneously with the classical equations of motion for the nuclei

$$M\ddot{\mathbf{R}} = -\nabla_{\mathbf{R}} E_m(\mathbf{R}) \tag{28}$$

where the force is the negative gradient of the potential energy of the "current" m-th adiabatic state. The hopping probabilities g_{ij} between the states are determined by

$$g_{ij} = 2\frac{\Delta t}{c_i c_i^*}[Im(c_i^* c_j \epsilon_i \delta_{ij}) - Re(c_i^* c_j \dot{\mathbf{R}}\langle\psi_i|\nabla_{\mathbf{R}}|\psi_j\rangle)] \tag{29}$$

and can occur randomly according to the fewest-switches surface hopping approach introduced by Tully.[349] This approach has been designed to satisfy the statistical distribution of state populations at each time according to the quantum probabilities $|c_i|^2$ using the minimal number of "hops" necessary to achieve this condition.

However, this internal consistency is not always maintained, as analyzed in the literature.[351] One of the often noticed reasons for the internal inconsistency in MDQT is the presence of classically forbidden transitions. The energy conservation is achieved in MDQT during the transition by adjusting the classical velocities in the direction of the nonadiabatic coupling vector.[349] The transition is classically forbidden if there is not enough velocity in this direction. In this case, two alternatives are commonly used. Either this component of velocity is inversed, or it remains unchanged. The existence of classically forbidden transitions may lead to an inconsistency between the fraction of trajectories in each state and the averaged quantum probability. Another reason for the internal inconsistency in MDQT is the divergence of independent trajectories. For example, in the case that two surfaces substantially differ, the trajectories on the lower state can diverge and follow different pathways after leaving the nonadiabatic coupling region. Since in standard MDQT the quantum amplitudes are propagated coherently for each trajectory, in the case that some trajectories diverge, the coherent propagation can lead also to an inconsistency between the fraction of trajectories in each state and the corresponding average quantum probability. The analysis of the reasons for these inconsistencies and the proposals for improving them can be found in ref 351. The conclusion can be drawn that, in order to obtain the time evolution of the population, the fraction of trajectories is more reliable than the averaged quantum probabilities. Thus, it is better to use the fraction of trajectories for the simulation of the pump−probe signals. Problems with surface hopping methods are particularly pronounced for systems involving an extended nonadiabatic coupling region or when tunneling processes as well as a large number of recrossings occur in this region.

For the determination of the pump−probe signal accounting for passage through the conical intersection, the expression for the cationic occupation $P_{22}^{(2)}$ given by eq 22 has to be modified. This is due to necessity in considering that the propagation of the ensemble starts in the excited state but can hop to the ground state according to the fewest-switches hopping algorithm. Therefore, not only the common averaging over the whole ensemble of the initial conditions due to the Wigner approach is required, but also, for a given initial condition, an averaging over trajectories obtained from different random numbers according to the hopping algorithm must be carried out.[116] Consequently, the coordinates and momenta of the propagated state can be labeled by $\mathbf{q}_x^\nu$ and $\mathbf{p}_x^\nu$, where x is either the excited or the ground state, as determined by the hopping procedure. The quantities ν numerate the set of random numbers used in the hopping algorithm, satisfying the same initial condition. Therefore, the average over the number of hoppings N_{hop} has to be performed, and for the cationic population the following expression yields

$$\begin{aligned} P_{22}^{(2)}(t) &= \int \mathrm{d}\mathbf{q}\ \mathrm{d}\mathbf{p}\ P_{22}^{(2)}(\mathbf{q},\mathbf{p},t) \\ &\sim \int \mathrm{d}\mathbf{q}_0\ \mathrm{d}\mathbf{p}_0 \int_0^t \mathrm{d}\tau_2 \int_0^{t-\tau_2} \mathrm{d}\tau_1 \frac{1}{N_{\mathrm{hop}}} \times \\ &\sum_\nu \exp\left[-\sigma_{\mathrm{pr}}^2 \frac{[\hbar\omega_{\mathrm{pr}} - V_{+1,x}(\mathbf{q}_x^\nu(\tau_1;\mathbf{q}_0,\mathbf{p}_0))]^2}{\hbar^2}\right] \times \\ &\exp\left[-\sigma_{\mathrm{pu}}^2 \frac{[\hbar\omega_{\mathrm{pu}} - V_{10}(\mathbf{q}_0,\mathbf{p}_0)]^2}{\hbar^2}\right] \times \\ &I_{\mathrm{pu}}(t-\tau_1-\tau_2)\, I_{\mathrm{pr}}(t-\tau_2-t_{\mathrm{d}})\, P_{00}^{(0)}(\mathbf{q}_0,\mathbf{p}_0) \end{aligned} \tag{30}$$

which is a modification of eq 22 valid for the adiabatic case. The quantity $V_{+1,x}$ labels the energy gap be-

tween the propagating state and the cationic state at the instant of time. From this expression, the pump−probe signal can be calculated after integration over the pump−probe correlation function $\int_0^\infty d\tau_2\ I_{pu}(t-\tau_1-\tau_2)\ I_{pr}(t-\tau_2-t_d)$ is performed explicitly:

$$S[t_d] = \lim_{t\to\infty} P_{22}^{(2)}(t)$$
$$\sim \int d\mathbf{q}_0\, d\mathbf{p}_0 \int_0^\infty d\tau_1 \exp\left\{-\frac{(\tau_1 - t_d)^2}{\sigma_{pu}^2 + \sigma_{pr}^2}\right\} \times$$
$$\frac{1}{N_{hop}}\sum_\nu \exp\left\{-\frac{\sigma_{pr}^2}{\hbar^2}[\hbar\omega_{pr} - V_{+1,x}(\mathbf{q}_x^\nu(\tau_1;\mathbf{q}_0,\mathbf{p}_0))]^2\right\} \times$$
$$\exp\left\{-\frac{\sigma_{pu}^2}{\hbar^2}[\hbar\omega_{pu} - V_{10}(\mathbf{q}_0,\mathbf{p}_0)]^2\right\} P_{00}^{(0)}(\mathbf{q}_0,\mathbf{p}_0) \quad (31)$$

According to expression 31, the initial ground-state density $P_{00}^{(0)}$ is promoted to the first excited state with the Franck−Condon transition probability given by the last exponential of eq 31. The propagation, the passing through the conical intersection, and the probe transition to the cationic state are described by the second exponential. This expression can be generalized for more than two states by introducing in eq 31 the sum of weighting factors corresponding to the transition moments between the electronic states involved, for which also time-dependent energy gaps have to be calculated. The probe pulse window, being located around the time delay t_d between the pump and the probe pulses, and the resolution of the signal determined by the square of the pulse durations are given by the first exponential. As it is required in the Wigner distribution approach, an ensemble average over the initial conditions has to be performed. The latter can be obtained from a sampling of the initial vibronic Wigner distribution $P_{00}^{(0)}$ of the ground electronic state.

Of course, the basically inherent problems of surface hopping methods can be overcome by using other semiclassical formulations, for example, the framework of stationary phase approximation,[353,354] the linearized semiclassical initial value representation,[221−223] the semiclassical multisurface hopping propagator approach,[355−357] the multiple spawning method,[226,358] the quantum-classical density matrix approach involving a hybrid MD−Monte Carlo algorithm with momentum jumps,[359,360] and the semiclassical multistate Liouville dynamics in diabatic and adiabatic representations.[216,220,361,362] The majority of these methods is computationally more demanding and so far is usually tested and applied on model systems.

Quantum Corrections. Regarding the connection with time-dependent quantum chemistry through classical trajectories "on the fly", it is of particular interest to mention the semiclassical multistate Liouville dynamics in diabatic and adiabatic representations[216,220,361,362] and the multiple spawning method.[226] Both approaches allow introduction of the quantum effects in nonadiabatic dynamics.

In the case of the semiclassical limit of the quantum Liouville equation for multistate electronic-nuclear dynamics, this occurs by introducing additional time-dependent coefficients to each member of the coupled ensemble. These additional dynamical variables represent the time-dependent weights of the trajectories, providing phases for the electronic coherence. The formulation in the adiabatic representation is particularly attractive because it can be connected directly with the calculation of nonadiabatic coupling "on the fly".[216,220,361,362] The results are promising for accounting for coherence effects in the semiclassical treatment of nonadiabaticity. Nevertheless, the applications on the realistic systems have to be carried out in the future.

Full multiple spawning dynamics is a typical approach with classical features but allows for approximate consideration of quantum mechanical effects, which means for the interaction of nuclear populations of different electronic states. It makes use of local properties of quantum chemistry, providing the potential energy and its derivatives for a particular nuclear geometry, from which forces can be calculated and used as locality in time, in classical dynamics. The ab initio full multiple spawning (AIMS) method is nonadiabatic wave packet dynamics based on frozen Gaussians, originally introduced by Heller,[363] in which the calculations of electronic states and nonadiabatic couplings are carried out "on the fly". In the total time-dependent wave function in the framework of the Born−Oppenheimer ansatz

$$\Phi(\mathbf{r},\mathbf{R};t) = \sum_K \psi_k(\mathbf{r},\mathbf{R})\ \chi_k(\mathbf{R};t) \quad (32)$$

the nuclear wave function χ_k in a specific electronic state k is a linear combination of multidimensional traveling Gaussians with time-dependent coefficients $C_j^k(t)$, where j labels the nuclear basis function

$$\chi_k = \sum_j C_j^k(t) G_j^k \quad (33)$$

The Gaussians G_j^k are, in turn, products of time-dependent one-dimensional frozen Gaussians for each degree of freedom. Using this ansatz, Hamilton's classical equations of motion for position, momentum, and nuclear phase have to be solved. This allows one to establish the connection between classical dynamics and quantum chemistry. Finally, the nuclear Schrödinger equation for the time-dependent coefficients $C_j^k(t)$ involves calculations of diagonal and off-diagonal elements of the Hamiltonian matrix. These include computation of multidimensional integrals and nonadiabatic couplings. Since both are computationally very demanding, the approximations described in ref 226 are generally used. The accuracy of describing some quantum mechanical phenomena, such as nonadiabaticity and tunneling, depends not only on these approximations but also on the choice of nuclear basis functions (e.g. trajectories) on each electronic state; each of these is dressed by multidimensional Gaussian functions. An important feature

of this method is the possibility to extend nuclear basis functions when it is needed, such as, for example, according to the magnitude of nonadiabatic couplings. This means that additional nuclear basis functions are spawned only when the system goes through the region of nonadiabatic couplings. This allows for making the computational demand feasible. Consequently, several interesting applications in photochemistry have been achieved using this method.[226] The fast multiple spawning (FMS) method is nevertheless more computationally demanding than other approximate methods for the description of nonadiabatic dynamics of large systems, such as surface hopping approaches, Pechukas force methods,[364,365] and mean field approximations. Systematic comparisons of these approaches on realistic systems still have to be carried out.

3.3. Full Quantum Mechanical Multistate Nuclear Dynamics and fs-Signals

The methods for time-dependent quantum simulations represent powerful quantitative tools for studying and understanding dynamics of systems with few atoms, provided that accurate precalculated global potential energy surfaces (PESs) are available. The computational aspects in solving the time-dependent Schrödinger equation involve spatial discretization of the wave function, action of the Hamiltonian on the wave function, and propagation of the initial wave function in time.[366−369] The latter two allow one to carry out discretization in time.

The grid representation is a widely used technique for discretization of the wave function.[368,369] The grid has to include the whole wave function during the time period investigated, and the number of points has to be large enough to mimic the continuous function. Consequently, the number of grid points scales as M^N where N is the dimension of the problem and M is the number of grid points for each degree of freedom. Therefore, the method is limited to systems with few degrees of freedom. There are also other efficient methods for spatial discretization which will be not addressed here.[370]

Concerning the time discretization, the action of the potential energy part of the Hamiltonian on the wave function is simply a pointwise multiplication over the spatial grid due to the fact that the potential energy operator is local in coordinates. In the case of the action of the kinetic energy operator on the wave function, the Fourier method is a suitable approach, since it makes use of the fact that the kinetic energy operator is local in the reciprocal momentum space. This allows transformation of the wave function, employing a fast Fourier transform algorithm in momentum space where the direct multiplication can be carried out, after which an inverse Fourier transform back to the coordinate space is made.[367−369] Finally, the time-dependent wave function has to be evaluated according to the Schrödinger equation

$$\Psi(t) = \hat{U}(t)\ \psi(0) = \mathrm{e}^{-i/\hbar \hat{H} t}\psi(0) \tag{34}$$

where, for the time-independent Hamiltonian, the evolution operator $\hat{U}(t)$ has a simple exponential form. If $\hat{H}$ is time-dependent, then $\hat{U}$ is defined as

$$\hat{U}(t) = \exp(-i/\hbar \int_0^t \hat{H}(t')\ \mathrm{d}t') \tag{35}$$

To apply the evolution operator on the initial wave function, the procedures for discretization of the evolution operator have to be used which involve different types of expansions. Those used mostly are expansions into series of Chebyshev and so-called local propagators, such as second-order differences (SODs) or split-operator (S−O) methods.[367−369]

From this brief outline of the basis of quantum dynamical algorithms, the conclusion can be drawn that, for each additional degree of freedom, the numerical operations in propagation increase by a factor corresponding to the number of grid points needed for an appropriate description of the given mode. Moreover, the grid methods cannot be directly connected with ab initio MD "on the fly" because they make use of grid points from precalculated energy surfaces. Both aspects are disadvantageous for consideration of systems larger than four atoms or six coupled modes.

fs-Signals. For the calculation of the pump−probe signals using grid methods, we outline the procedure for ultrashort pulses and weak fields for which first-order perturbation theory is applicable.[371] The system is initially in the vibrational ground state χ_0 with energy E_0 of the electronic ground state $|0\rangle$. The vibrational dynamics in the electronic state $|1\rangle$ can be observed by a time-delayed fs-excitation to the electronic state $|2\rangle$, and detection of a fluorescence signal or of a photoionization signal follows from state $|2\rangle$.

The nuclear wave function χ_1 of the electronic excited state $|1\rangle$ can be written as

$$\chi_1(t) = \frac{1}{i}\int_0^t \mathrm{d}t\ U_1(t-t')\ V_{10}(t',T_1)\ U_0(t')\chi_0 \tag{36}$$

with U_1 and U_0 propagators for the nuclear motion in the electronic states $|1\rangle$ and $|0\rangle$, respectively. The interaction energy in the dipole approximation is

$$V_{10}(t,T_1) = -\mu_{10}\epsilon_0 G(t,T_1)\mathrm{e}^{-\omega_1(t-T_1)} \tag{37}$$

with the following labels: the dipole transition μ_{10} between states $|0\rangle$ and $|1\rangle$, the strength of the field ϵ_0, and the frequency ω_1. $G(t,T_1)$ is the envelope function centered around T_1 and is therefore denoted as Gaussian. By discretization of the integral given by eq 36

$$\chi_1(t) \approx \Delta t \sum_{n=0}^{N} U_1[(N-n)\Delta t] V_{10}(n\Delta t, T_1)\ U_0(n\Delta t)\chi_0 \tag{38}$$

one obtains

$$\chi_1(t) \approx \sum_{n=0}^{N} a_n w_n^{(1)} \tag{39}$$

where $w_n^{(1)}$ and a_n are weighting factors and amplitudes, respectively.

$$a_n = U_1[(N-n)\Delta t]\mu_{10}\chi_0 \quad (40)$$

and the rest is a weighting factor.

The expression (eq 39) for the excited-state wave function is the coherent sum of $\mu_{10}\chi_0$ propagated for different times $(N-n)\Delta t$ on the excited state with weighting factors $w_n^{(1)}$. An analogous expression holds for the nuclear wave function χ_2 in state $|2\rangle$ which arises from the absorption of a photon induced by a fs-pulse with frequency w_2 and field strength ϵ_0', which is centered at T_2 and starts at $t = 0$:

$$\chi_2(t) = \frac{1}{i}\int_0^t \mathrm{d}t'\; U_2(t-t')\; V_{21}(t',T_2)\; U_1(t')\chi_1(t') \quad (41)$$

with the interaction between the field and the system given by $V_{21}(t',T_2)$. Since the pump and probe pulses do not overlap, discretization leads to

$$\chi_2(t) \approx \Delta t \sum_{m=0}^{N} U_2[(N-m)\Delta t]V_{21}(m,\Delta t,T_2)\,\chi_1(m,\Delta t) \quad (42)$$

Inserting the expression for $\chi_1(m,\Delta t)$ given by eq 39 and defining the weight $w_m^{(2)}$ as

$$w_m^{(2)} = \Delta t\epsilon_0' G(m,\Delta t - T_2)\mathrm{e}^{i\omega_2(m\Delta t - T_2)} \quad (43)$$

one obtains

$$\chi_2(t) \approx \sum_{m=0}^{N}\sum_{n=0}^{m} w_m^{(2)} w_n^{(1)} U_2[(N-m)\Delta t]\mu_{21}a_n$$
$$\approx \sum_{m=0}^{N}\sum_{n=0}^{m} w_m^{(2)} w_n^{(1)} b_{mn} \quad (44)$$

Finally, the population in state $|2\rangle$ corresponding to the signal is calculated according to

$$P_2(\tau) = \lim_{t\to\infty}\langle\chi_2(t)|\chi_2(t)\rangle \quad (45)$$

For details, see refs 371 and 372. The formulation for pump−probe signals in terms of population of the final state for the case that two electronic states are coupled is given in ref 372.

4. Analysis of Dynamics and of Simulated fs-Signals

4.1. Multistate Adiabatic Nuclear Dynamics in Ground States and Simulation of NeNePo Pump−Probe Signals: Noble Metal Clusters

Advances in experimental pump−probe fs-spectroscopy include application of vertical one-photon detachment to prepare a nonequilibrium state of clusters and subsequent investigation of its dynamics by two-photon ionization. This technique is known as NeNePo (negative ion-to-neutral-to-positive ion) spectroscopy and was pioneered by Wöste and his colleagues.[175] Since dynamics in the ground state of the neutral species can be explored, this approach bridges cluster dynamics with the real time investigation of chemical reactions.

fs-NeNePo spectroscopy is also attractive for theoretical investigation for the following reasons: it requires development of methods for adiabatic ab initio MD "on the fly" in the ground state and their application for simulation of femtosecond signals; it provides the opportunity to determine conditions under which different processes and their time scales can be observed; and therefore, it contributes to establish the scope of this experimental technique.[112,119,181,373] Concerning the first aspect, the accuracy of electronic structure calculations, using for example an ab initio gradient corrected density functional approach with Gaussian atomic basis sets for MD "on the fly" (AIMD-GDFT),[79,280−283,293] and the adequacy of the semiclassical Wigner distribution approach for simulation of fs pump−probe signals can be tested by comparing obtained results with experimental findings and with the full quantum mechanical treatment of the nuclei. The latter is feasible for trimers.[114] Second, by introducing experimental conditions for simulation of fs-signals, their influence on revealed processes can be examined. Third, by varying the size and composition of clusters, processes such as geometric relaxation, intracluster collisions, IVRs, structural information based on vibronic patterns, as well as isomerization processes can be identified in the pump−probe signals, providing a conceptual frame for NeNePo spectroscopy. All of these aspects will be illustrated with examples of silver, gold, and mixed silver−gold clusters.

To do this, the electronic and structural properties of noble metal clusters will be addressed first. Then attention will be paid to MD "on the fly" and to the simulation of signals, and finally, the analysis of signals and comparison with experimental findings will be presented, allowing for identification of processes and for proposals of new experiments.

Electronic Structure. Structural, reactivity, and optical properties of noble metal clusters attracted theoretical[43,82−88,91,92,109,117,119,181,374−376] and experimental researchers[24−28,375−384] over the years because of their relatively simple electronic nature in comparison with that of transition metals and their similarity to s-shell alkali metals. This is particularly the case for the Ag atom because of a large s−d gap in contrast to that of the Au atom. In the latter case, the s−d gap is considerably smaller and, therefore, the relativistic effects play an essential role, strongly influencing the energy of an s-orbital, for example. These differences in electronic structure are also reflected in structural properties of small silver and gold clusters. Recent theoretical and experimental investigations showed that gold clusters remain planar for larger sizes than do the silver clusters.[85,109,375,376] Increasing interest in gold and silver clusters is due to their newly discovered size-selective reactivity properties toward molecular oxygen and CO.[29,43,44,87,88,91,385,386] In this context, the mixed silver−gold clusters have also attracted the attention of researchers due to the electronegativity difference between Ag and Au atoms[85,384] giving rise to charge transfer from Ag to Au. All together, the noble metal

clusters represent an attractive research direction for fs-chemistry.

Relativistic effective core potentials (RECPs) are mandatory for a description of the studied species. In general, effective core potential (ECP) methods allow one to eliminate core electrons (close to nuclei) from explicit electron correlation treatment, which then involves only electrons directly participating in bonding. Usually they were developed in the literature for the Hartree−Fock wave functions, and therefore, they had to be revisited and carefully tested in connection with the gradient corrected density functional theory (GDFT) method.[88] GDFT is presently the method of choice for the ground-state properties of metallic clusters provided that the use of correlation and exchange functionals allows for accurate determination of binding energies and structural properties, which is not always the case.[88] This is particularly important for a reliable calculation of the energy ordering of different isomers which can assume related or very different structures with close lying energies. The presence of a number of isomers for a given cluster size is an unpleasant characteristic of metal clusters (alkali- as well as noble-metal clusters). Therefore, determination of the lowest energy structure is not always an easy task. Consequently, the temperature is a crucial parameter which has to be considered in experiment and theory. Notice that only at low temperatures can the mixture of different isomers be avoided, in contrast to the cases at higher temperatures.

In the early work on structural and optical properties of neutral and charged silver clusters, 1- and 11-electron relativistic effective core potentials (1e-RECPs and 11e-RECPs) with corresponding AO basis sets were developed.[83,84,374] The first one, which was later revisited in connection with the DFT method[119] employing Becke and Lee, Yang, Parr (BLYP) functionals[287,288] for exchange and correlation, respectively, is suitable for description of the ground-state properties. The second one is inevitable for determination of excited states of pure silver clusters. Since d-electrons are localized at the nuclei of silver atoms, they almost do not participate in bonding. Their role is only important for the quantitative determination of energies of excited states in silver clusters. Recent DFT calculations on structural properties using 19e-RECPs and ion mobility experiments carried out on Ag_n^+ clusters[376] have confirmed the early findings.[83,84] The 1e-RECP for the Au atom is less reliable for studying structural properties of Au clusters because the d-electrons participate directly in bonding. The use of the 1e-RECP for gold clusters might be useful only if the results agree with those obtained from the 19e-RECP, due to the fact that the former one is computationally considerably less demanding. (For details, see ref 85.) Moreover, for reactivity studies involving oxidized clusters, the 19e-RECP is mandatory also for silver clusters due to the activation of d-electrons by the p-electrons of the oxygen atom.[43,88,91]

Dynamics and Signals. To study fs-dynamics of metallic clusters as a function of their size, the precalculation of energy surfaces is not practicable (although for trimers feasible). Therefore, the ab initio MD approach "on the fly" is the method of choice. Ab initio molecular dynamics codes, which utilize a Gaussian atomic basis set and gradient corrected density functional (AIMD-GDF),[279−283] are, in the meantime, implemented in standard programs such as Gaussian[309] or Turbomole.[310] The investigation of dynamics of atoms is carried out by integration of the classical equations of motion using the Verlet algorithm (cf. eqs 1 and 2).[290] The SCF Kohn−Sham formulation and the accurate calculations of Pulay forces (cf. section 3.1) are needed at each time step in order to achieve a satisfactory conservation of the total energy. It is important that all this occurs at low computational demand, because the simulation of pump−probe signal requires, in addition to the calculation of an ensemble of trajectories for the ground state of the neutral species, calculations of the energy gaps between neutral and cationic ground states. The accurate numerical evaluations of the exchange-correlation energy parts of the Kohn−Sham matrix and the exchange-correlation energy derivatives are the most computationally demanding steps if the number of AO basis functions is not extremely large. Therefore, effort has been made to reach a good accuracy at relatively low cost (cf. refs 279−283).

For the simulation of NeNePo signals, a combination of the ab initio molecular dynamics "on the fly" with the vibronic density matrix approach in the classical Wigner−Moyal representation offers an adequate approach (cf. section 3.2.1). This involves (i) the density of the anionic state forming the initial ensemble, (ii) the density of the neutral state reached after photodetachment by the pump, (iii) the density of the cationic state after photoionization of the probe, and (iv) the laser-induced transition probabilities between the latter two states. Densities and transition probabilities can be calculated in the framework of the classical approximation to the Wigner−Moyal transformed Liouville equation for the vibronic matrix by restricting the expansion to the lowest order in $\hbar$ as outlined in section 3.2.1. In addition, only the first-order optical transition processes can be taken into account, which is justified for the low laser intensities, as it is the case in the NeNePo technique. Assuming zero kinetic energy (ZEKE) conditions for the photodetached electron and for the cation, as well as short laser pulses which can be well described with Gaussian pulse envelopes, the analytic expression for time-resolved NeNePo signals directly related to expression 24 of section 3.2.1 can be straightforwardly formulated:

$$\begin{aligned} S[t_d] &= \lim_{t\to\infty} P_{22}^{(2)}(t) \\ &\approx \int d\mathbf{q}_0\, d\mathbf{p}_0 \int_0^\infty d\tau_1 \exp\left\{-\frac{(\tau_1 - t_d)^2}{\sigma_{pu}^2 + \sigma_{pr}^2}\right\} \times \\ &\exp\left\{-\frac{\sigma_{pr}^2}{\hbar^2}[\hbar\omega_{pr} - V_{IP}(\mathbf{q}_1(\tau_1;\mathbf{q}_0,\mathbf{p}_0))]^2\right\} \times \\ &\exp\left\{-\frac{\sigma_{pu}^2}{\hbar^2}[\hbar\omega_{pu} - V_{VDE}(\mathbf{q}_0)]^2\right\} P_{00}(\mathbf{q}_0,\mathbf{p}_0) \quad (46) \end{aligned}$$

Here σ_{pu} (σ_{pr}) and $E_{pu} = \hbar\omega_{pu}$ ($E_{pr} = \hbar\omega_{pr}$) are the pulse durations and excitation energies for the pump

and the probe step with the time delay t_d. The quantity $V_{IP}(\mathbf{q}_1(\tau_1;\mathbf{q}_0,\mathbf{p}_0))$ labels the time-dependent energy gaps between neutral and cationic ground states calculated at coordinates $\mathbf{q}_1(\tau_1)$ on the neutral ground state with initial coordinates and momenta $\mathbf{q}_0$ and $\mathbf{p}_0$ given by the anionic thermal Wigner distribution $P_{00}(\mathbf{q}_0,\mathbf{p}_0)$, and $V_{VDE}(\mathbf{q}_0)$ are the vertical detachment energies of the initial anionic ensemble. Therefore, the first step for the simulation of signals involves the generation of $P_{00}(\mathbf{q}_0,\mathbf{p}_0)$, which can be calculated either for individual vibronic states or for the thermal ensemble assuming the harmonic approximation in the case of low or moderate initial temperatures, for which the anharmonicities of nuclei are negligible. Then, the Wigner distribution for each normal mode is given by

$$P(q,p) = \frac{\alpha}{\pi\hbar}\exp\left[-\frac{2\alpha}{\hbar\omega}(p^2+\omega^2p^2)\right] \qquad (47)$$

with $\alpha = \tanh(\hbar\omega/2k_bT)$ and the normal-mode frequency ω, corresponding fully to the quantum mechanical density distributions. The ensemble of initial conditions needed for the MD on the neutral ground state energies emerges from sampling of the phase space distribution given by expression 47. For the case of high temperatures, for which anharmonicities are important but quantum effects of the initial distribution are not, the phase space distribution can be obtained from a sufficiently long classical trajectory. The analytical expression for NeNePo signals given by eq 46 is easy to understand. The last exponential in eq 46 gives the Franck−Condon transition probability after the initial ensemble is photodetached. Then, the propagation occurs on the neutral state in terms of MD "on the fly", giving rise to the time-dependent ionization energies V_{IP}. The transition to the cationic ground state involves the probe step with a window function given by the second exponential of eq 46. The signal is obtained by the summation over the whole ensemble, and its time resolution is determined by the pump−probe correlation function with the probe window located around the time delay between two pulses given by the first exponential of eq 46. The spectral resolution depends on the duration of both pulses.

However, expression 46 has to be modified if the emitted electrons carry away some amount of kinetic energy. Consequently, for the simulation of the transient photoionization NeNePo signal, the integrations of the populations of the anionic and cationic states over the entire range of possible excess energies E_0 and E_2 have to be carried out in order to provide an approximate treatment of continuum. This leads to the following expression of the NeNePo signals

$$\begin{aligned} S[t_d] &= \lim_{t\to\infty} P_{22}^{(2)}(t) \\ &\approx \int d\mathbf{q}_0\, d\mathbf{p}_0 \int_0^\infty d\tau_1 \exp\left\{-\frac{(\tau_1-t_d)^2}{\sigma_{pu}^2+\sigma_{pr}^2}\right\} \times \\ &\int_0^\infty dE_2\ \exp\left\{-\frac{\sigma_{pr}^2}{\hbar^2}[\hbar\omega_{pr} - V_{21}(\mathbf{q}_1(\tau_1;\mathbf{q}_0,\mathbf{p}_0))]^2\right\} \times \\ &\int_0^\infty dE_0\ \exp\left\{-\frac{\sigma_{pu}^2}{\hbar^2}[\hbar\omega_{pu} - V_{10}(\mathbf{q}_0)]^2\right\} P_{00}(\mathbf{q}_0,\mathbf{p}_0) \end{aligned} \qquad (48)$$

Now the application of above outlined combination of methods will be illustrated in order to demonstrate the importance of the interplay between theory and experiment.

4.1.1. Trimers

The example of silver and mixed silver−gold trimers will be addressed in more detail because it allows for identification of conditions under which the separation of time scales of different processes can be observed. Moreover, the theoretically proposed concept can be verified by comparison with experimental findings obtained under different conditions. For this purpose, either the energy surfaces for the ground state of trimers (for anions, neutrals, and cations) can be precalculated (e.g. for Ag_3)[112,113] or ab initio MD "on the fly" can be used (e.g. Ag_2Au).[119,181] In the former case, full CI calculations for valence electrons were performed, and in the latter case, the gradient corrected DFT procedure was employed.

$Ag_3^-/Ag_3/Ag_3^+$. The global minima of the anionic, neutral, and cationic silver trimers assume linear, obtuse triangular, and equilateral trianglar structures, respectively. The location of the minimum of the anion corresponds to a saddle point of the neutral Ag_3. The structural properties of the neutral Ag_3 are characterized by the Jahn−Teller effect, leading to the threefold degenerate minima (cf. Figure 1). The first electronically excited state $^2A_1$ of the neutral Ag_3 exhibits a surface crossing with the ground state $^2B_2$. Nonadiabaticity has not been considered in the dynamics under the assumption that a sufficiently large excess of energy after electron detachment leading to the geometry relaxation in the ground state of Ag_3 will smear out the effects stemming from coupling between two states.

In the experiment, a transient linear Ag_3 cluster has been prepared in its ground electronic state by one-electron photodetachment of the linear Ag_3^-. The temporal evolution from the linear to triangular Ag_3 has been investigated by a delayed ionizing pulse via two photon ionization. The energy scheme of the multistate dynamics for $Ag_3^-/Ag_3/Ag_3^+$ is shown in Figure 1. The Franck−Condon region and the minimum energy region of Ag_3 serve to determine the excitation energies for the pump and probe lasers. Pump pulse wavelengths in the range between VDE = 2.45 eV and the continuum (2.95 eV $\le E_{pu} \le$ 3.13 eV) were employed. The values for E_{pr} range from the vertical ionization potential for the linear geometry to the ionization potential for the triangular one (6.67 eV $\le E_{pr} \le$ 5.73 eV). Since the influence of temperature is important, the corresponding initial conditions can be prepared (e.g. for T = 50 K and T = 300 K). For this purpose, an ensemble of coordinates and momenta can be sampled at short time intervals from a long microcanonical trajectory (e.g. of 10 ps) obtained from the MD on the anionic ground state. By rescaling the velocities, equilibration can be achieved until the time averaged kinetic energy, corresponding, for example, to T = 50 and 300 K, can be obtained. The Franck−Condon transition probabilities in terms of abundances of VDEs between Ag_3 and Ag_3^- for both temperatures are shown in Figure

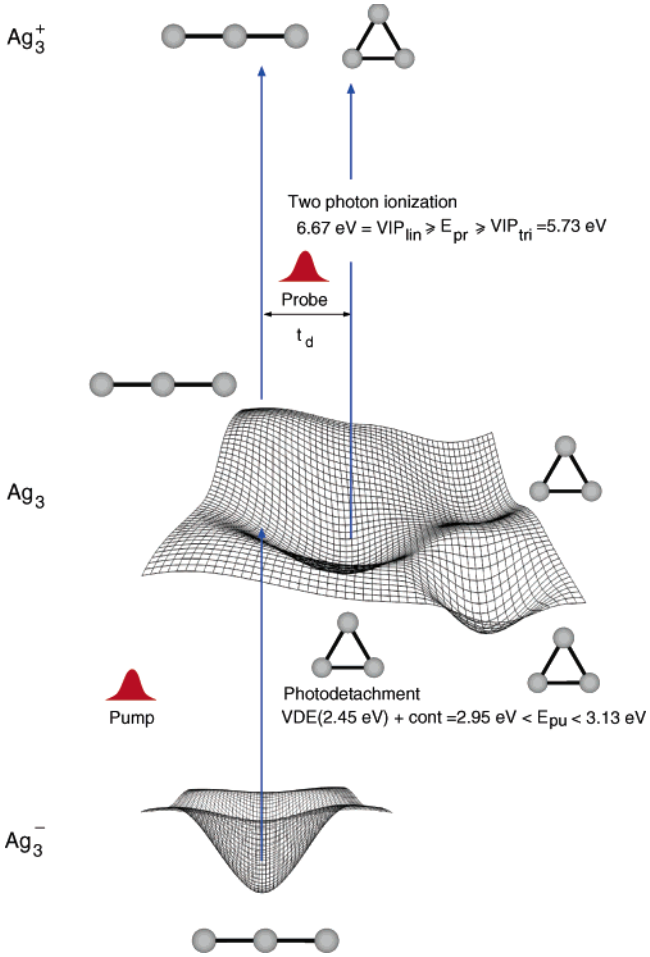

Figure 1. Scheme of the multistate fs-dynamics for NeNePo pump−probe spectroscopy of $Ag_3^-/Ag_3/Ag_3^+$ with structures and energy intervals for pump and probe steps.[112,113]

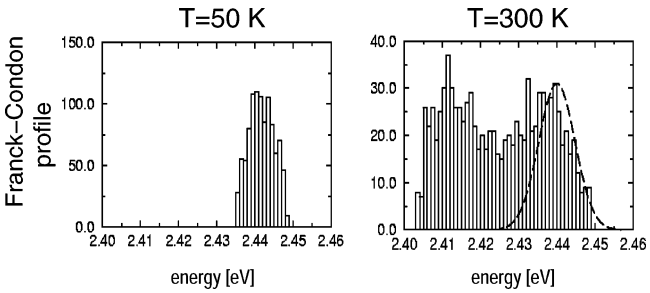

Figure 2. Franck−Condon transition probabilities in terms of abundancies of vertical detachment energies (VDEs) of the Ag_3^- anion at 50 and 300 K. The line shape of a 100 fs Gaussian shape pulse at a pump energy of 2.44 eV has been plotted for $T = 300$ K in order to illustrate spectral filtering.[112,113] Reprinted with permission from ref 112. Copyright 1998 American Institute of Physics.

2. The maximum of the VDE is temperature independent, since it corresponds to VDE = 2.45 eV of the linear geometry of the anion. The asymmetric broadening for the 300 K ensemble arises from the different energy behavior of anion and neutral species along the bending mode. The simulated NeNePo-ZEKE signals using two initial conditions at low and at higher temperature corresponding to the entire anionic initial ensemble are shown in Figure 3.[112,113] The choice of duration of the probe pulse, $\sigma_{pr} = 100$ fs, corresponds to usual experimental conditions.

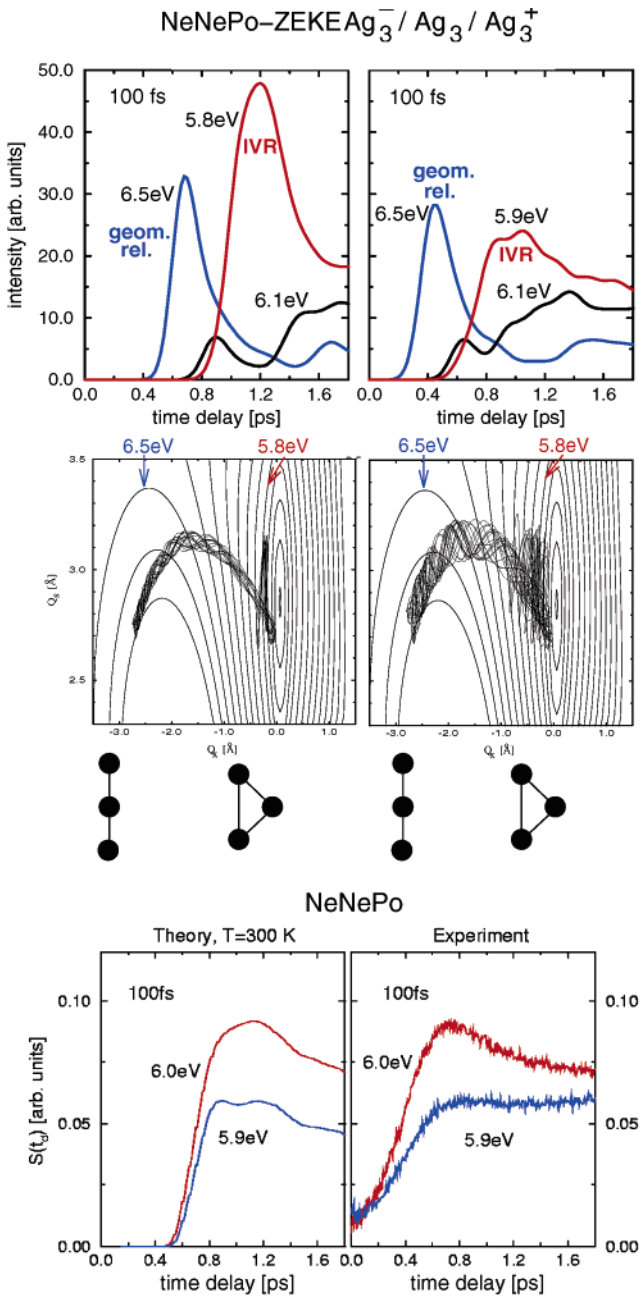

Figure 3. Simulated NeNePo-ZEKE signals ($\sigma_{pu} = 0$ fs, $\sigma_{pr} = 100$ fs) for 50 and 300 K and for $E_{pr} = 6.5$, 6.1, and 5.8 eV (upper part). Bunches of trajectories of the 50 and 300 K ensembles projected on a Q_x (bending) and Q_s (symmetric stretching) contour plot of the cation−neutral energy gap surface (values of 6.5 and 5.8 eV are indicated) (middle part). Comparison between simulated ($T = 300$ K) and experimental NeNePo signals[112,113] for energies of the probe pulse of 5.9 and 6.00 eV (bottom part).

The signals are shown for three probe energies, corresponding to the Franck−Condon region ($E_{pr} = 6.5$ eV), to the Jahn−Teller region of the neutral Ag_3 ($E_{pr} = 5.8$ eV), and to an intermediate energy ($E_{pr} = 6.1$ eV). The simulated signals for $E_{pr} = 6.5$ eV, close to the Franck−Condon region, reflect the changes of the vertical ionization energies due to geometric relaxation from linear to triangular structures. The time scales for the onset of intensity, for its maximum, and for a decrease of intensity are temperature-dependent (at higher temperature, time scales are shorter due to higher velocities of the nuclei). For

$E_{pr} = 5.8$ eV, close to the Jahn−Teller region of Ag_3, the rise and fall of signals occur at considerably later times.

To elucidate the nature of these signals occurring after the geometric relaxation was accomplished, the bunches of trajectories projected on the contour plot for the bending mode and the symmetric stretching modes of the cation−neutral energy gaps are shown also in Figure 3. They allow for the straightforward identification of the IVR induced by a sudden energy transfer from the bending to the stretching mode due to a strong repulsion of the terminal atoms (intracluster collision) for $E_{pr} = 5.8$ eV. It can be seen that the system moves along the 5.8 eV contour line with an almost constant IP for the low temperature case. For $T = 300$ K the ensemble exhibits a spatial spread after the intracluster collision, since both bending and stretching modes are simultaneously excited. This leads to a lower intensity of the signal in the IVR time domain than in the case of low temperatures. At longer times, the analysis shows that dissipative IVR results in vibrational equilibration. In conclusion, Figure 3 reveals that the geometric relaxation and IVR can take place in Ag_3 on different time scales if probed by appropriate energies. These time scales can be influenced by the temperature of the initial ensemble.

The continuum of energy for the detached electron and for the probed cation will be addressed, since it corresponds closer to the original experimental NeNePo conditions. For the 300 K initial ensemble, the simulated signals according to eq 48 are compared with the recorded ones in the lower part of Figure 3. The clear distinction between the geometric relaxation and IVR, which was identified in NeNePo-ZEKE signals, is smeared out under the influence of continuum. The simulated signals are in good agreement with the experimental ones, confirming that the experimental conditions do not allow one to distinguish different processes such as geometric relaxation from IVR.

$Ag_2Au^-/Ag_2Au/Ag_2Au^+$. The above findings stimulated new experiments at low temperature in the initial photodetachment step and with conditions closer to the NeNePo-ZEKE situation which were performed on the mixed trimer. This allows one to study also the influence of the heavy atom on the time scale of fs-processes. The doping of the silver trimer by one gold atom gives rise to the following structural properties: the anionic trimer assumes the linear structure with one Au−Ag heterobond. The isomer with two heterobonds lies 0.38 eV higher in energy. Both linear structures are transition states for the neutral Ag_2Au, which assumes acute triangular geometry, while the obtuse triangle is the minimum for the cation. Each transition state interconnects two symmetry equivalent triangular structures and has two imaginary frequencies along the degenerate bending mode. Notice that the structural properties of mixed trimers are sensitive to the details of the methodological treatment (choice of RECP and of functionals in the DFT procedure). Therefore, the inclusion of d-electrons in the RECP is necessary for quantitative considerations. The energetic scheme relevant for NeNePo together with the structural properties of neutral and charged Ag_2Au is shown in Figure 4.

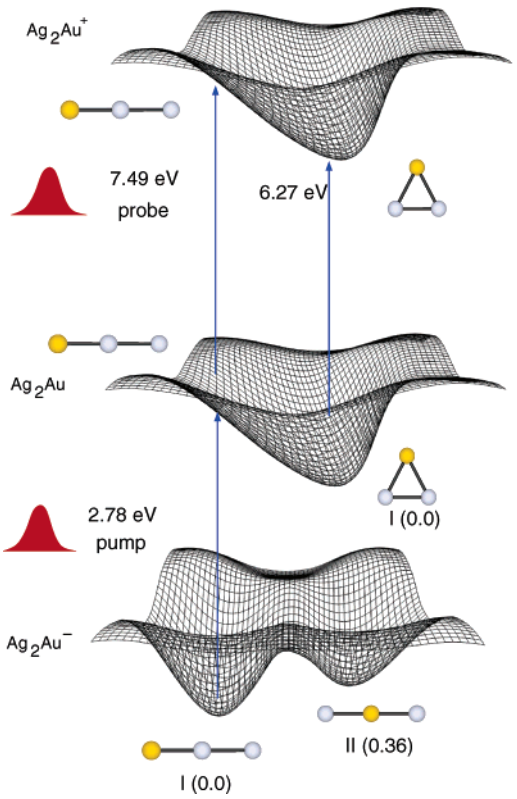

Figure 4. Scheme of the multistate fs-dynamics for NeNePo pump−probe spectroscopy of $Ag_2Au^-/Ag_2Au/Ag_2Au^+$ with structures and energy intervals for pump and probe steps.[119,181]

For the simulations at the initial temperature of 20 K, only the most stable isomer is populated. Under these conditions, the harmonic approximation is valid, and therefore, the initial conditions for the MD simulations can be safely sampled from the canonical Wigner distribution at each independent normal mode using eq 47. Accordingly, the histograms of the vertical detachment energies (VDEs) (or Franck−Condon transition probabilities) assume an almost Gaussian shape centered around 2.78 eV. To simulate NeNePo signals, an ensemble of trajectories (e.g. ~500) has to be propagated in the neutral state, and the time-dependent energy gaps to the cationic state have to be calculated along the trajectories. They are shown in the upper part of Figure 5, since they provide information about the time evolution of individual processes such as the onset of geometrical changes and IVR. Within the first 2 ps, the swarm of energy gaps changes from 7.5 to 6.5 eV, and subsequently, all energy gaps oscillate in the energy interval between 6.1 and 6.5 eV, corresponding to vibrational dynamics within the basin of triangular Ag_2Au. The minimum energy gap value of ~6.1 eV marks the closest approach of the terminal silver and gold atoms, which is referred to as an internal collision within the cluster. Therefore, by adjusting the probe−pulse energy, two different types of processes can be probed in NeNePo-ZEKE signals. Pulse energies between 6.5 and 7.5 eV probe the onset of relaxation processes. Therefore, the signals should

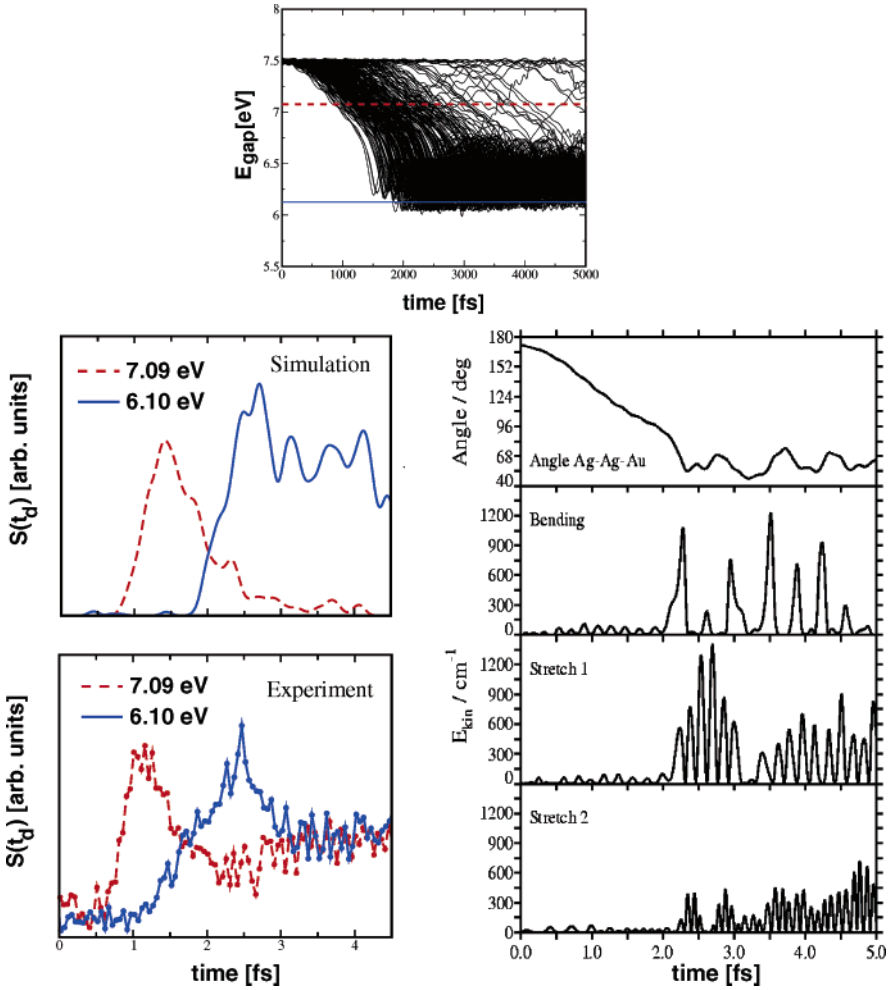

Figure 5. (upper part) Bunch of the cation−neutral energy gaps of Ag_2Au. Energies of 7.09 eV (dashed line) and of 6.1 eV (full line) indicate the proximity of the Franck−Condon region and of the minimum of the neutral species, respectively, and are used for simulations of signals. (lower part) Comparison between simulated and experimental NeNePo-ZEKE signals of $Ag_2Au^-/Ag_2Au/Ag_2Au^+$ (ref 181) (left side). Single-trajectory example of the evolution of the Ag−Ag−Au bond angle and of the kinetic energy in the three vibrational normal modes (right side).

exhibit maxima at delay times when the probe energy is resonant with energy gaps and decrease to zero at later times. Pulse energies below 6.5 eV probe the arrival of and dynamics at the triangular structure. It is to be expected that, at ~6.1 eV pulse energies, the signal will rise after ~2 ps and remain constant at later times. This is illustrated also on the left side of Figure 5, in which the theoretical NeNePo-ZEKE simulated signals are compared with recently obtained experimental results at low temperature (T ~ 20 K) for two probe energies, E_{pr} = 7.09 eV probing the Franck−Condon region and E_{pr} = 6.10 eV probing the triangular geometry region corresponding to the minimum of the neutral Ag_2Au.[181] Experiment and theory are in excellent agreement. The signals at E_{pr} = 7.09 eV reflect geometric relaxation from linear to triangular geometry of the neutral Ag_2Au. The signals at E_{pr} = 6.10 eV are due to IVR.

Insight into the IVR can be gained from an analysis of the single-trajectory example, shown on the right-hand side of Figure 5. At times t < 2.0 ps, the three vibrational modes contain very little energy according to the envelope of their kinetic energy oscillations. This is because the system is located in the flat region of the PES where the bond angle is larger than 90°. In this region, the potential energy is high but can be viewed as a constant offset, which is not available for the vibrational modes. The small envelopes of the kinetic energy oscillations are almost constant, implying only very little IVR in this time domain. At times t > 2.0 ps, the system enters the deep part of the potential well so that the kinetic energy of all modes increases. At t = 2.3 ps, the kinetic energy in the bending mode reaches a sharp maximum. Shortly after the bending mode has passed its maximum kinetic energy, its kinetic energy drops to zero due to internal collision of peripheral atoms. Since the other mode energies increase at the same time, IVR is manifested. The drop of the kinetic energy in the bending mode cannot solely be explained by a conversion of kinetic to potential energy in the bending mode. Since this behavior is also characteristic for other trajectories, one can generally state that notable IVR sets in at the instant of internal collision. This means that the nature of IVR is related to the one found for Ag_3 (cf. refs 112 and 113). Two important aspects should be emphasized. Time scales are much longer than in the case of Ag_3 due to heavy atom influence. Importantly, the experimental results reveal for the first time geometric relaxation separated from an IVR process, indicating that they are close to the ZEKE-like conditions, which has been

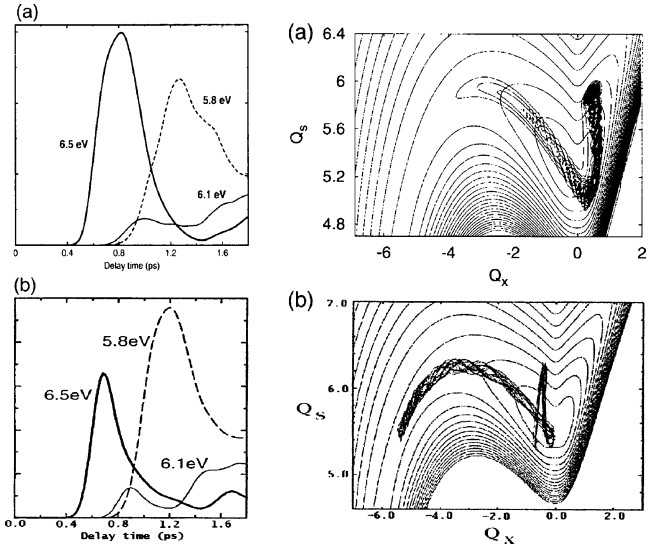

Figure 6. (left side) Comparison of full quantum dynamics and semiclassical simulated NeNePo-ZEKE signals of Ag_3^-/Ag_3/Ag_3^+. (right side) Comparison of the wave packet (a) and bunches of trajectories (b) projected on Q_x (bending) and Q_s (symmetric stretching) contour plots of the neutral PES.[114]

proposed by theory as a necessary condition for the separation of time scales of these processes.[181]

Notice that, in the above simulations, quantum coherence effects are not taken into account as a consequence of the classical approximation for the nuclei. This corresponds to the situations for which the signals can be simulated by an ensemble of independent trajectories where all anharmonicities are included but quantum effects are not incorporated. Therefore, in the case of Ag_3^-/Ag_3/Ag_3^+, it is valuable to compare the simulated signals, based on full quantum mechanical treatment of the dynamics of the nuclei employing the grid method for wave packet propagation,[114] with those obtained from classical trajectory simulations using the same energy surfaces.[112,113] The signals obtained from both methods for low temperature exhibit very similar features, as shown in Figure 6. They only differ in the relative intensities for geometric relaxation versus IVR. As expected, in the full quantum mechanical treatment, the IVR process is more delocalized than that in the classical treatment, giving rise to the lower intensity of the signal responsible for the IVR process, as shown on the right-hand side of Figure 6.

4.1.2. Tetramers

To illustrate the scope of the NeNePo technique, two examples, Ag_4 and Au_4, have been chosen for the presentation because they exhibit different structural properties in the anionic state and common properties in the neutral state. In the case of the silver tetramer, the global minima of the anion and of the neutral cluster assume related rhombic structures. Therefore, after photodetachment at low temperatures ($T \approx 50$ K), ensuring thermal distribution around the rhombic geometry, the pump step reaches the nonequilibrium rhombic configuration close to the global minimum of the neutral species, as shown on the left side of Figure 7. Notice that the initial temperatures which prevent the isomerization within the anionic state are mandatory, since the well defined initial state is a necessary condition to observe time scales and processes involved in the geometric relaxation of the neutral ground state. This condition does not allow one, for example, to monitor the isomerization into the T-form in the neutral ground state, since for this purpose an initial temperature of more than 700 K is needed, at which an isomerization in the ground anionic state would already occur. Consequently, for the low-temperature $T = 50$ K initial conditions, the probe in the Franck−Condon region with $E_{pr} = 6.41$ eV reveals the vibrational structure of the rhombic configuration after photodetachment. For the probe with, for example, $E_{pr} = 6.46$ eV, the dynamics in the vicinity of the neutral rhombic structure can be monitored. The simulated NeNePo-ZEKE signal at 6.41 eV for a probe duration of 50 fs shown in Figure 7 exhibits oscillations with a vibrational period of ∼175 fs, which is close to the frequency of the short diagonal stretching mode, indicating the occurrence of the geometric relaxation along this mode toward the global minimum. The analysis of the signal also reveals contributions from two other modes shown in Figure 7. In summary, the above example illustrates that an identification of the structure of a gas-phase neutral cluster in experimental NeNePo signals is possible due to its vibronic resolution.[119]

In contrast, the investigation of nuclear dynamics and simulation of NeNePo-ZEKE signals of Au_4 allow one to follow long amplitude motions leading to isomerization because the stable structures of Au_4^- and Au_4 assume linear (or closely related zigzag geometry) and rhombic forms, respectively.[119] Low-temperature initial conditions ($T \approx 50$) ensure that only the linear anionic structure contributes to the initial ensemble which is photodetached by the probe pulse, as shown in the scheme presented in Figure 8. The two-photon ionization or probe laser covering the energy range between ∼8.4 and 8.1 eV monitors the initiated relaxation dynamics on the neutral state involving linear, T-form, and rhombic isomers (cf. Figure 8).

Relaxation dynamics is influenced by the linear local minimum of the neutral species which is energetically reached after the photodetachment. The signal at $E_{pr} = 8.86$ eV, shown in Figure 8, reflects dynamics within the local linear isomer reached after photodetachment. It is characterized by oscillations corresponding to one of the symmetric stretching modes which is responsible for a nondephased relaxation process of the initial nonequilibrium ensemble. The intensity of the signal decreases after 1 ps, indicating occurrence of the relaxation process from linear to rhombic structure. Consequently, both signal intensities at $E_{pr} = 8.09$ eV and $E_{pr} = 8.27$ eV increase, reflecting the appearance of other isomers. A temporary identification of the rhombic structure at $E_{pr} = 8.09$ eV is possible only through a small maximum. Otherwise, structureless line shape indicates the presence of both rhombic and T-form isomers due to a large internal vibrational energy.

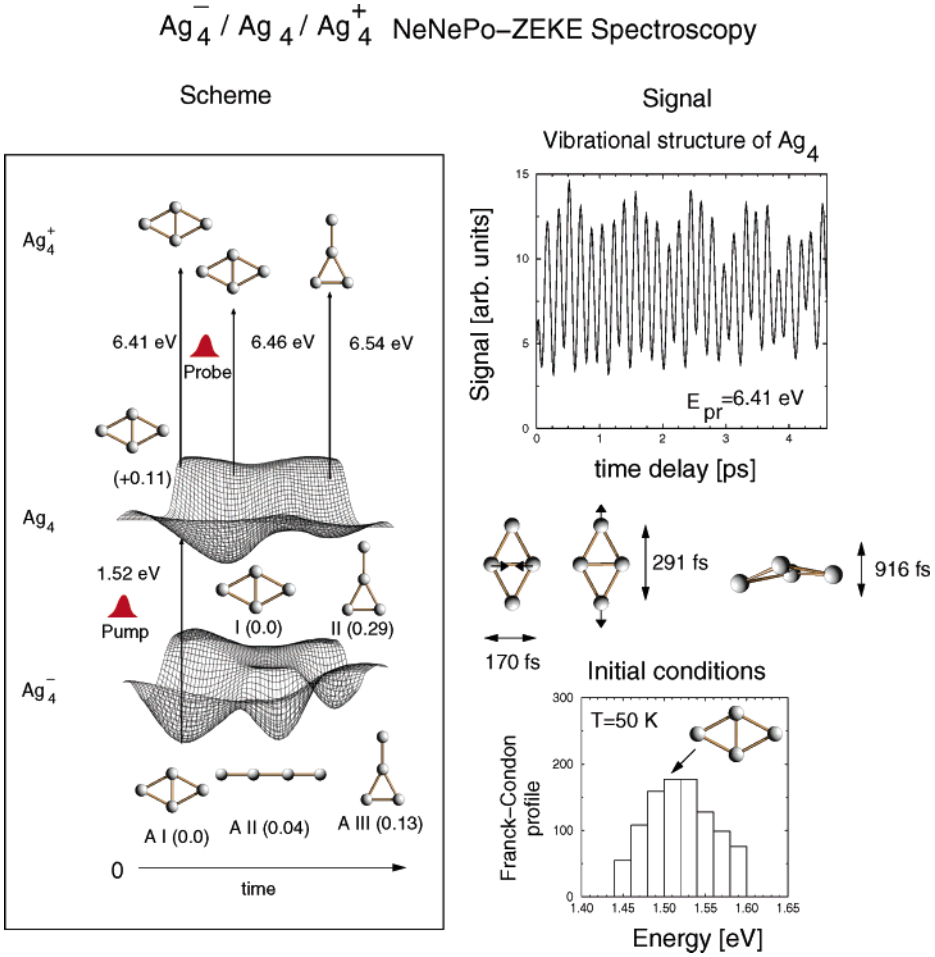

Figure 7. (left side) Scheme of multistate fs-dynamics for NeNePo pump−probe spectroscopy of $Ag_4^-/Ag_4/Ag_4^+$ with structures and energy intervals for the pump and probe steps. (top right side) Simulated NeNePo-ZEKE signals for the 50 K initial condition ensemble (bottom right side) at the probe energy of 6.41 eV and a pulse duration of 50 fs. Normal modes responsible for relaxation leading to oscillatory behavior of the signal are also shown (middle right side).[119]

It is interesting to point out that the absence of dephasing during the relaxation dynamics in the vicinity of the nonequilibrium state reached after photodetachment is the signature of the local minimum which has a different influence on the dynamics than the transition state does, for example in the case of Ag_3 and Ag_2Au.

Summary. Finally, the following question can be raised: what can be learned from multistate-ground state dynamics and from simulated NeNePo-ZEKE signals in general? First, the connection between three objectives can be established: the structural relation of anionic and neutral species, the influence of the nature of the nonequilibrium state reached after photodetachment, and the subsequent character of dynamics in the neutral ground state. Three different situations can occur in which the (i) transition state, (ii) global minimum, and (iii) local minimum can influence the dynamics after photodetachment. Second, different types of relaxation dynamics can be identified in NeNePo-ZEKE signals, which means that these processes can be, in principle, experimentally observed.

(i) In cases where the anionic structure is close to a transition state of the neutral electronic ground state (e.g. trimers), large amplitude motion toward the stable structure dominates the relaxation dynamics. In other words, the dynamics is incoherent but localized in phase space. IVR can be initiated as a consequence of the localized large amplitude motion. Large amplitude structural relaxation after the transition state (as occurs in the case of Ag_3 and Ag_2Au) is responsible for a pronounced single peak in NeNePo-ZEKE signals at a given time delay and probe excitation wavelengths. In addition, subsequent IVR processes can be identified, but only under ZEKE-like conditions.

(ii) In cases where the anionic structure is close to the global minimum (stable isomer) of the neutral electronic ground state, vibrational relaxation reflecting the structural properties of the neutral stable isomer (e.g. Ag_4) takes place. The dynamics can be dominated by one mode (e.g. Ag_4) or only by a few modes given by the geometric deviations between anionic and neutral species. Other modes and anharmonicities weakly contribute, leading to dephasing on a time scale up to several picoseconds (>2 ps for Ag_4). Vibrational relaxation gives rise to oscillations in NeNePo signals (for different pulse durations) which can be analyzed in terms of normal modes. Since the stable structure is characterized by the corresponding normal modes, this offers the opportunity to identify structural properties of gas-

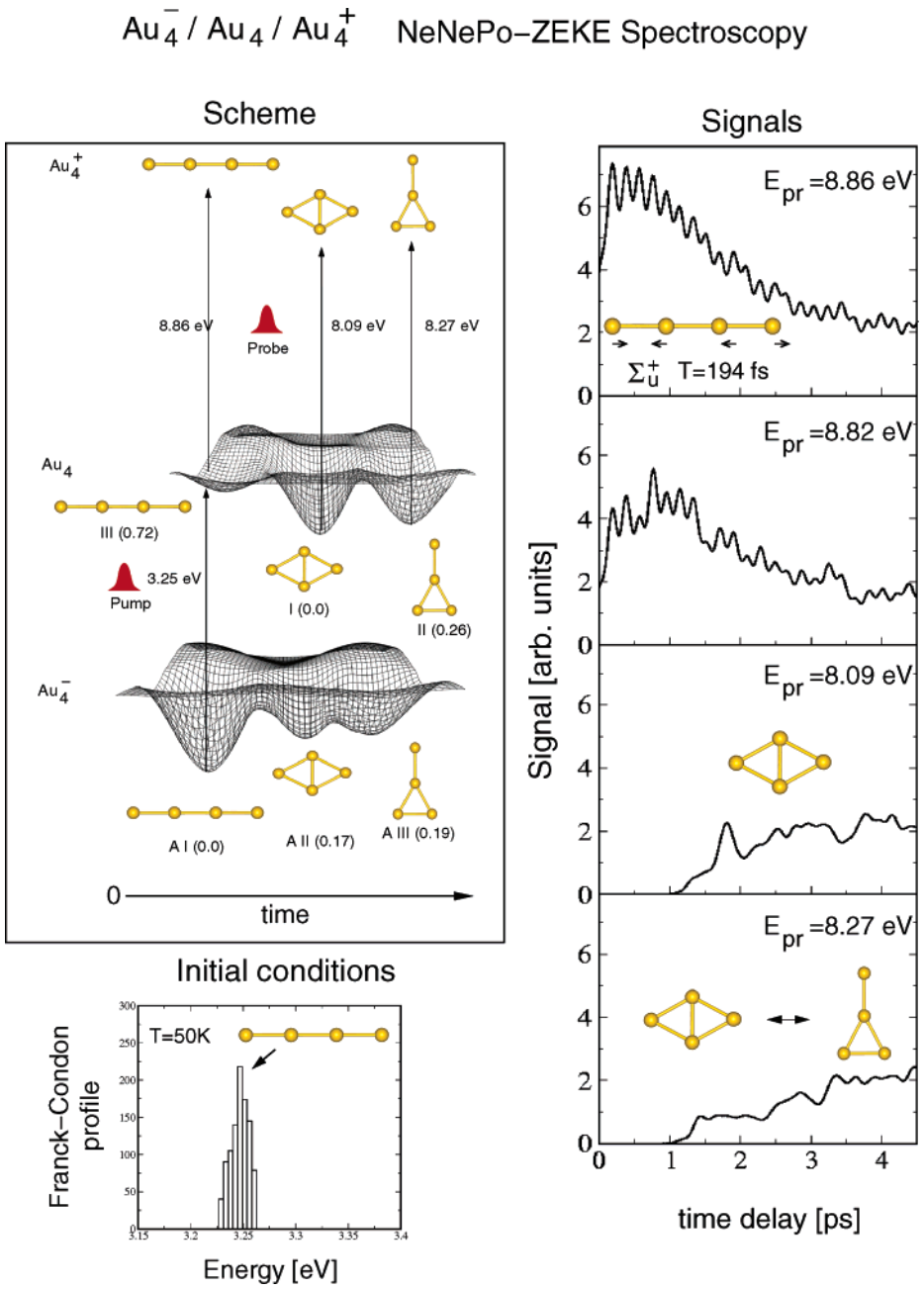

Figure 8. (top left side) Scheme of the multistate dynamics for NeNePo pump−probe spectroscopy of $Au_4^-/Au_4/Au_4^+$ with structures and energy intervals for the pump and probe steps. (right side) Simulated NeNePo-ZEKE signals for the 50 K initial condition ensemble (bottom left side) at different probe energies.[119]

phase clusters experimentally by the NeNePo technique.

(iii) In cases where the anionic structure (initial state) is close to a local minimum (energetically high lying isomer) of the neutral electronic ground state (e.g. Au_4), the character of the nonequilibrium state is governed by the local minimum. Vibrational relaxation within the local minimum is likely to dominate the ultrashort dynamics (on a time scale <1 ps for Au_4). Nondephased regular vibrational relaxation has been shown in the case of Au_4, where the pronounced activation of only one stretching mode takes place, since the normal modes of the anionic and neutral species are almost identical.

Moreover, the local minimum can act as a strong capture area for nuclear motion with time scales up to several picoseconds. As a consequence, isomerization processes toward other local minima and/or toward the global minimum structure are widely spread in time. In other words, structural relaxation dynamics is characterized as being incoherent and delocalized in phase space. Signals exhibit (at different excitation wavelengths of the probe laser) fingerprints for vibrational relaxation within the local minimum, providing structural information. After systems escape from the local minima, the time scales for the beginning of structural relaxation can be identified by the onset of signals at given probe wavelengths (≈1 ps Au_4), although the relatively structureless signals of low intensity can reflect the delocalized character of the structural relaxation.

Due to the aspects listed above, the NeNePo technique in connection with the optimal control schemes represents a promising technique to introduce the control of the chemical reactivity of clusters, such as oxidation of CO by noble metal oxide clusters, which is of relevance for heterogeneous catalysis.

4.2. Multistate Adiabatic Nuclear Dynamics Involving Electronic Excited and Ground States and Simulation of Pump–Probe and Pump-Dump Signals: Nonstoichiometric Alkali Halide Clusters

As briefly outlined in section 3.1 on time-dependent quantum chemistry, ab initio MD "on the fly" in excited states can be carried out in the framework of various wave function based or density functional based methods. The interplay between accuracy and computational demand still does not allow applications to arbitrarily chosen systems. Nevertheless, high accuracy and low computational demand can be achieved by an adequate choice of systems for which the description of the excited states is simple and for which the semiclassical approach to dynamics is a suitable approximation. In this case, the simulations of the signals based on the ab initio Wigner distribution approach described in section 3.2 offer a valuable method which allows one to describe and to discover different ultrafast processes, as will be illustrated below.

4.2.1. Sodium Fluoride Clusters with One Excess Electron

The structural and optical properties of nonstoichiometric alkali halide clusters have attracted the attention of many theoretical and experimental researchers[100−102,104,124,125,387−412] due to the localization of the excess electrons, which are not involved in ionic bonding. The prototypes for a particularly simple situation concerning the description of excited states are nonstoichiometric sodium fluoride clusters with a single excess electron, for example, Na_nF_{n-1}. In this case, a strong absorption in the visible-infrared energy interval occurs due to the excitations of the one excess electron placed in a large energy gap between occupied (HOMO) and unoccupied (LUMO) one-electron levels which resemble the "valence" and the "conductance" bands in infinite systems. Therefore, these clusters offer the opportunity to investigate optical properties of finite systems with some bulk characteristics such as F-color centers. Moreover, a simple but accurate description of the excited states is possible to achieve in the framework of the one-electron "frozen ionic bonds" approximation. In this method the optical response of the single excess electron can be explicitly considered, but in the field of the other $(n - 1)$ valence electrons involved in strongly polar ionic Na−F bonding.

The calculation of excited-state energies and of gradients based on the "frozen ionic bonds" approximation (as outlined in Appendix A) is, from a computational point of view, considerably less demanding in comparison with other approaches, such as RPA, CASSCF, or CI methods, and provides comparable accuracy. Therefore, this approach allows one to carry out adiabatic molecular dynamics in the excited state, by calculating the forces "on the fly" (cf. Appendix A) applicable to relatively large systems. This is particularly convenient for the simulation of time-dependent transitions for which an ensemble of trajectories is needed. Moreover, the fast computation of nonadiabatic couplings "on the fly" also allows one to carry out nonadiabatic MD as outlined in Appendix B. Of course, the application is limited to systems for which the "frozen ionic bonds" approximation offers an adequate description.

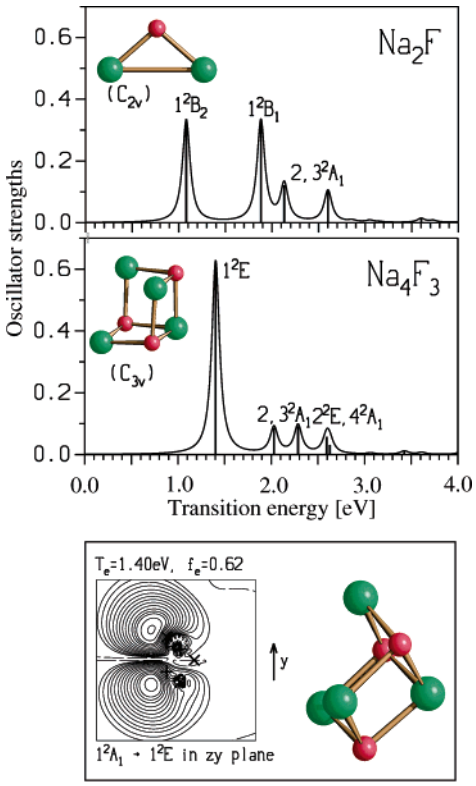

Figure 9. (top) Optically allowed transitions T_e in electronvolts and oscillator strength f_e obtained from the one-electron "frozen ionic bond" approximation for the stable ground-state structures of Na_2F and Na_4F_3 clusters.[115] (bottom) Contour plots of the transition density from the ground state to the first excited state, $1^2A_1 \rightarrow 1^2E$, defined as $D_{0n} = \int \rho_{0n}(\mathbf{r})\alpha \, d\beta$ with $\alpha \neq \beta = x, y, z$, where $\rho_{0n}(\mathbf{r}) = \int \psi_0(\mathbf{x}_1,...,\mathbf{x}_m)\ \psi_n(\mathbf{x}_1,...,\mathbf{x}_m)\ d\sigma_1\ d\mathbf{x}_2\ ...\ d\mathbf{x}_m$ facilitates comparison with $f_e \sim |\int \rho_{0n}(\mathbf{r})\alpha \, d^3\mathbf{r}|^2 = |\int D_{0n}\, d\alpha\, d\gamma|^2$ in the (z,y)-plane for the C_{3v} structure of the Na_4F_3 cluster. Solid and dashed lines label positive and negative values, while long-dashed lines indicate nodal curves. The crosses indicate the positions of the atoms corresponding to the geometry. Reprinted with permission from ref 115. Copyright 2001 American Institute of Physics.

On the basis of ab initio classical trajectories and assuming Gaussian femtosecond envelopes for the laser fields, analytic expressions for the time-resolved pump−probe and pump−dump signals in the framework of the Wigner distribution approach have been formulated in section 3.2.1. This ab initio Wigner distribution approach to adiabatic dynamics will be used in this section to illustrate the scope of the approach on examples of Na_nF_{n-1} clusters, first for those sizes for which adiabaticity is valid.

Na_2F versus Na_4F_3. These systems have been chosen for presentation of adiabatic dynamics in their first excited states. The corresponding simulated

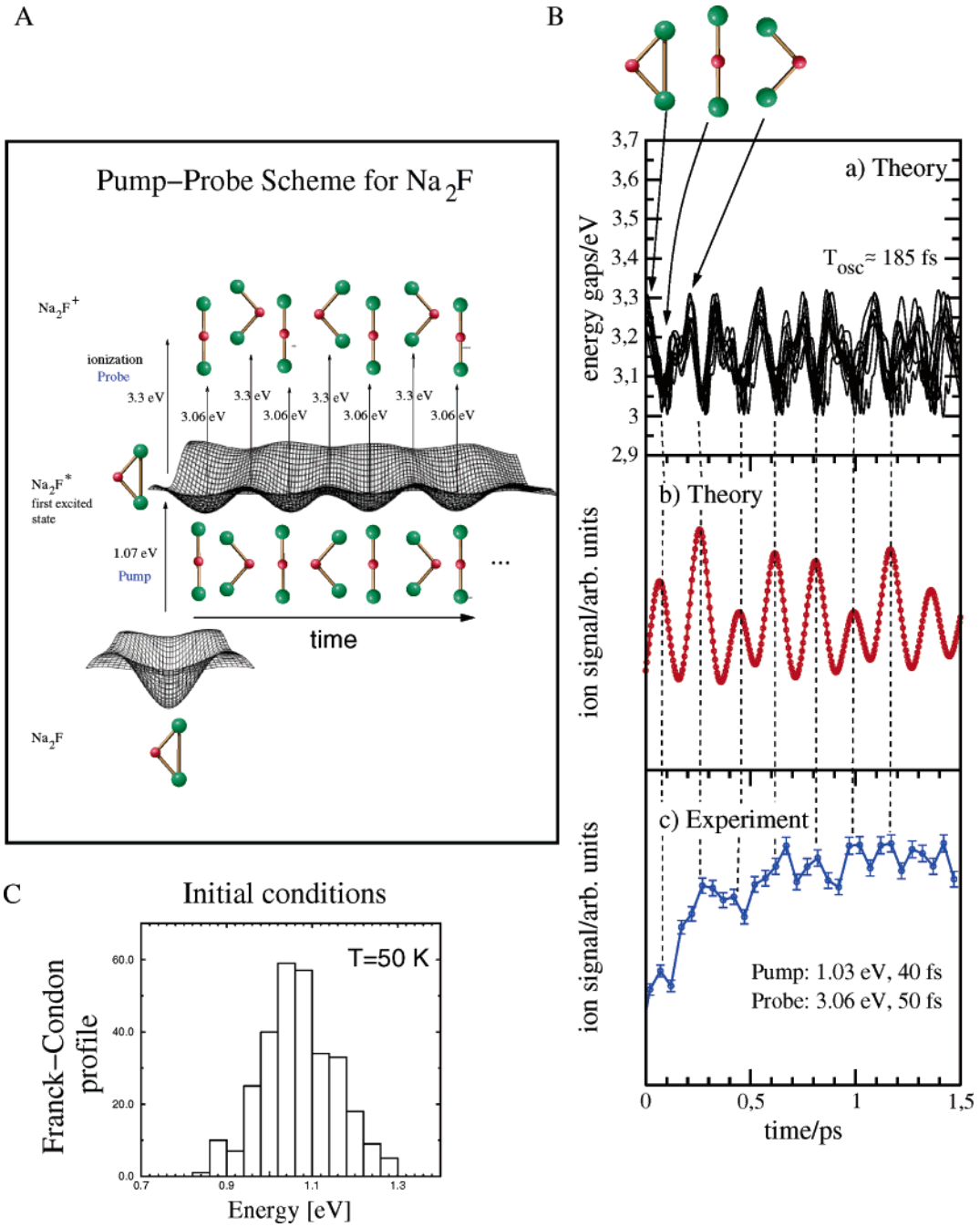

Figure 10. (A) Pump−probe NeExPo scheme for Na_2F involving the ground state (Ne), the electronic excited state (Ex), and the cationic ground state (Po). (B) Comparison of theoretical and experimental results:[120] (a) bunch of energy gaps between the first excited state of Na_2F and the cationic ground state during the dynamics in the first excited state; (b) simulated pump−probe signal; (c) experimentally observed transient. The involved cluster structures are shown in the top panel. (C) Temperature-dependent (T = 50 K) initial conditions; histogram of transition energies between the first excited state and the ground state.

pump−probe and pump−dump signals serve to address time scales of processes of different nature as well as methodological aspects. Despite the common absorption properties of both clusters shown in Figure 9, dynamics in the excited state is characterized by very different processes.[115] Metallic bond breaking occurs in the case of Na_2F. In contrast, just geometric deformation takes place in the case of Na_4F_3 without bond breaking which leads to relaxation of the cubic structure with the corner defect (cf. Figure 9). Therefore, from the time scale obtained for the breaking of the metallic Na−Na bond in Na_2F, the analogy concerning the time scale for breaking of delocalized bonds in metallic clusters can be drawn. Similarly, from time scales determined for localized lattice-defect relaxation after excitation in Na_4F_3, an analogy to dynamical behavior of F-centers in the bulk can be made. Moreover, classical versus quantum mechanical dynamics can be tested on the example of Na_2F, while the Na_4F_3 cluster serves as an adequate example for a moderately complex system for which the treatment of all degrees of freedom is computationally easy to achieve.

The vertical spectra obtained in the framework of the "frozen ionic bonds" approximation are shown in Figure 9. Using the same electronic structure ap-

proach (for details cf. ref 115), ab initio MD "on the fly" for excited electronic states can be performed and combined with the Wigner−Moyal representation of the vibronic density matrix, as outlined in section 3.2.1. Such an ab initio Wigner distribution approach to adiabatic dynamics allows for simulation of pump−probe signals using eq 24.

In the case of Na_2F, after vertical excitation, the conformational change in the first excited state occurs starting from the triangular ground state geometry and leading to the linear structure. Considerable lowering of the energy in the excited state occurs as shown in Figure 10A. A relatively small energy gap between the ground state and the first excited state is a consequence of an avoided crossing, obtained by breaking the Na−Na bond and overshooting the linear geometry connecting two equivalent triangular geometries. Despite the avoided crossing, the nonadiabatic coupling is weak and, therefore, adiabatic dynamics can be performed. In fact, this has been done by first using the ab initio Wigner distribution approach combined with the "frozen ionic bonds" approximation without precalculations of energy surfaces.[115,120] Later the quantum mechanical grid method for the propagation of nuclei in combination with precalculated energy surfaces based on the correlated wave function approach[124] was used.

The simple approach will be presented first. As the starting point, generation of a temperature-dependent initial Wigner phase space distribution on the neutral ground state is needed. A canonical thermal ensemble at a given temperature is suitable for low temperatures at which a harmonic approximation holds (cf. eq 47). This initial ensemble has to be brought to the first excite state with a Franck−Condon transition probability, involving the excitation energies from the neutral ground state to the first excited state as shown in Figure 10C. The propagation of this ensemble on the first excited state involves classical trajectory simulations. The probe window includes the time-dependent energy gaps between the cationic and the neutral excited states, taken at the propagated coordinate (cf. Figure 10B-a). The calculation of the signal requires a summation over the entire phase space (cf. Figure 10B-b).

The results presented in Figure 10B are based on simulations using an ensemble of 300 classical trajectories at an initial temperature of 300 K, which corresponds to experimental conditions.[120] The theoretically and experimentally obtained results are given in Figure 10B. The pulse duration and laser wavelength used in the experiment and in simulations are also shown in Figure 10B. The probe wavelength of 3.06 eV corresponds to the minimum of the first excited state with the linear geometry, as can be seen from Figure 10A. From the bunch of time-dependent energy gaps shown in Figure 10B-a, the periodic relaxation dynamics with a period of $\approx$185 fs can be identified. The maxima correspond to the bent structure, and the minima to the linear structure. At large times, anharmonicities in the bending mode introduce aperiodicity. Because the energy gaps are essential for determination of fs pump−probe signals, the oscillations in the simulated signal have the same period of 185 fs, as can be seen from Figure 10B-b. Since the linear geometries are probed for an ionization energy of 3.06 eV, they give rise to maxima in the signal. The periodic feature of the signal allows identification of the structural rearrangements from the triangular to the linear geometry during the butterfly type relaxation dynamics in the first excited state of Na_2F. This occurs due to the breaking of the Na−Na metallic bond, but the strong Na−F ionic bonds remain almost intact, which does not allow for fragmentation to take place. The period of 185 fs corresponds to half of the bending normal-mode frequency in the first excited state. Therefore, oscillations can be assigned primarily to the bending mode. Consequently, the IVR is very small, since the stretching modes do not significantly contribute. This means that the time scale for metallic bond breaking is $\sim$90 fs. A recorded transient Na_2F ion signal is shown in Figure 10B-c. The comparison of the theoretical pump−probe signal (Figure 10B-b) obtained from the ab initio Wigner distribution approach, combined with MD "on the fly" using the "frozen ionic bonds" approximation, with the experimentally obtained transient (Figure 10B-c) shows very good agreement. Both exhibit oscillations with a period of 185 fs, corresponding to a periodic butterfly-like rearrangement between bent and linear and back to bent geometries in the excited state due to the photoinduced metal bond breaking.[120] It is important to notice that theoretical predictions[115] have initiated the experimental work which confirmed predicted findings and, consequently, conceptually confirmed the proposed simple theoretical approach. In fact, theoretical results on Na_2F based on quantum mechanical dynamics and precalculated energy surfaces[124] fully support the theoretical results presented in Figure 10. Therefore, the conclusion can be drawn that excited-state dynamics in the framework of the "frozen ionic bonds" approximation, combined with the Wigner distribution approach, is capable of accurately describing processes on the femtosecond time scale for larger systems. This is particularly important if a selection of very few active modes for explicit treatment is not possible, since the precalculation of energy surfaces is, for all degrees of freedom, not realistic. This will be illustrated with the example of Na_4F_3.

For Na_4F_3 the optically allowed vertical transition to the first excited state with high intensity occurs due to fully localized excitation at the site of the halide vacancy. The geometric relaxation in the first excited state toward the minimum leads to the moderate lowering of the energy as shown in Figure 11. The energy gap between the ground state and the first excited state minimum is considerably larger than that in the case of Na_2F. This is due to the fact that no bond breaking occurs in the Na_4F_3, so that the energy of the ground state does not increase strongly.

The dynamics in the first adiabatic excited state "on the fly" for all degrees of freedom allows determination of time scales of geometric relaxation and of IVR for the optical excitation of the single excess electron localized at the corner defect of the cuboidal

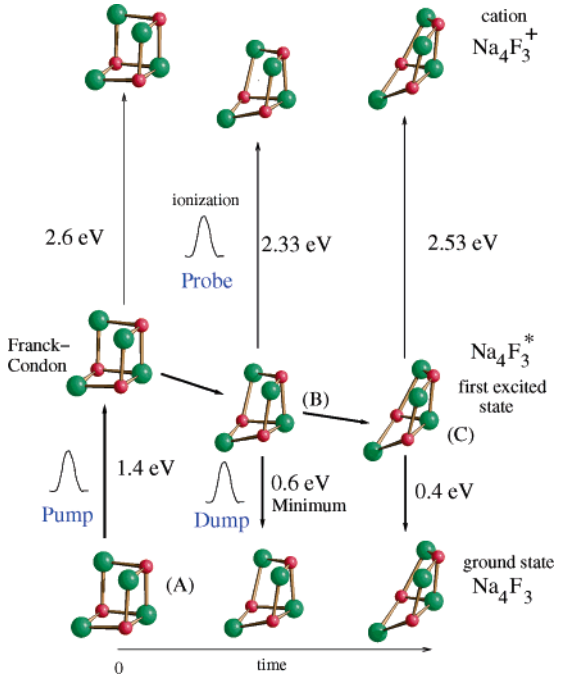

Figure 11. Scheme of the multistate fs-dynamics for the pump−probe NeExPo and the pump−dump NeExNe spectroscopy of Na_4F_3.[115] Thick arrows indicate dynamics on the first excited state starting from the initial cuboidal structure (A) toward the minimum energy "open cage" structure (B) including the even more deformed structure (C). Reprinted with perimission from ref 115. Copyright 2001 American Institute of Physics.

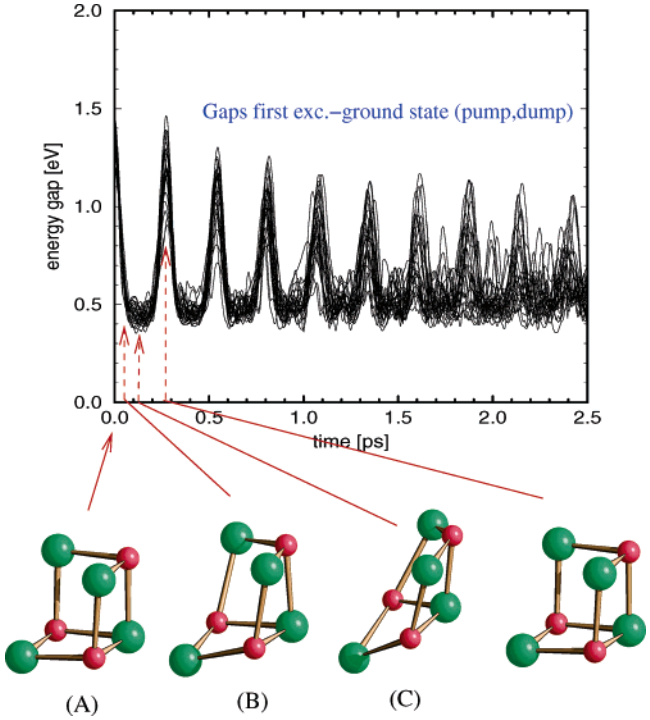

Figure 12. Bunch of energy gaps between the first excited state and the ground state of Na_4F_3 during the dynamics on the first excited state with the corresponding geometries obtained for the 30 K initial temperature.[115] Reprinted with perimission from ref 115. Copyright 2001 American Institute of Physics.

structure.[115] The pump−probe and pump−dump scheme is presented in Figure 11 with energies and structures of the minima in the ground state (A) and the first excited state (B). The structure of the minimum in the excited state is the strongly deformed "cage" of the cuboidal structure. The energy lowering from the vertical transition to the minimum of the excited state and the energy gaps between the ground state and the excited state for two different structures (B and C) are shown in Figure 12.

The Franck−Condon profile corresponding to the abundance of the energy gaps between the first excited state and the ground state for a 30 K initial ensemble is shown in Figure 13. This ensemble serves as an initial condition for the investigation of the dynamics in the first excited state. For the characterization of the ensemble dynamics, the bunches of energy gaps between the first excited state and the ground state are shown in Figure 12, since these quantities enter into the expression for the pump−dump signal. Regular cage oscillations can be monitored and are reflected in the periodical change of the gaps. However, for times beyond 1 ps, the periodicity is distorted due to the energy redistribution in other modes. This becomes clearly evident in the simulated pump−dump signals shown in Figure 14 for which the modified eq 24, as described in section 3.2.1, can be used.

The results of simulations are shown for three different dump laser energies: (i) $E_{du} = 1.2$ eV is close to the Franck−Condon region; (ii) $E_{du} = 0.6$ eV corresponds to the transition energy in the minimum of the first excited state; and (iii) $E_{du} = 0.8$ eV

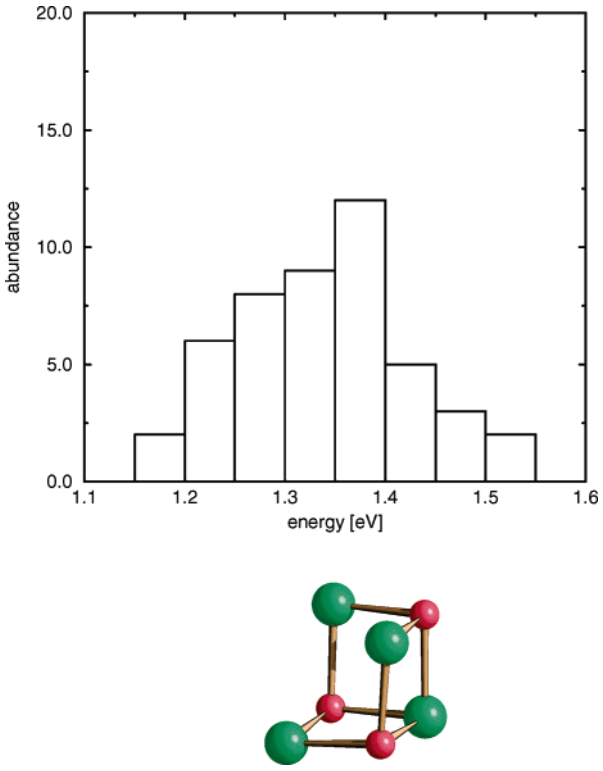

Figure 13. Histograms of the transition energies between the first excited state and the ground state of Na_4F_3 for a 30 K initial temperature ensemble.[115] Reprinted with perimission from ref 115. Copyright 2001 American Institute of Physics.

corresponds to an intermediate value. They allow one to reveal different types of IVR, as illustrated in Figure 14.[115] The time between the first maxima of

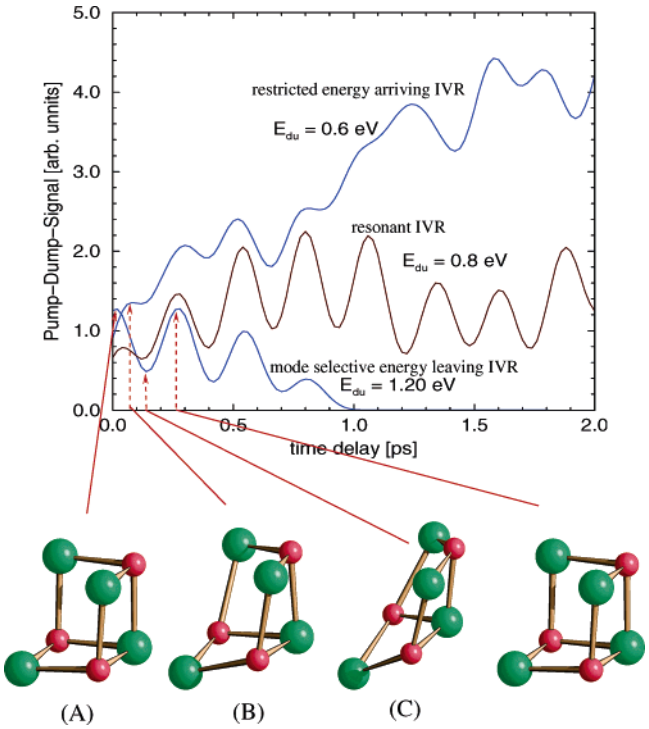

Figure 14. Simulated NeExNe pump−dump signals of a 30 K initial temperature ensemble of Na_4F_3 at different dump energies (E_{du}).[115] Reprinted with perimission from ref 115. Copyright 2001 American Institute of Physics. Assignment of structures to minima and maxima of signals indicate the time scales of geometric relaxation. Different types of IVR are indicated.

the signals calculated for $E_{du} = 1.2$ eV and $E_{du} = 0.6$ eV corresponds to the geometric relaxation time from the initially cuboidal structure (A) to the minimum of the first excited state ("cage" structure (B)). This amounts to <100 fs, indicating a very fast configurational relaxation. Furthermore, both the $E_{du} = 1.2$ eV signal and the $E_{du} = 0.8$ eV signal exhibit strong oscillations with a period of 260 fs. Therefore, these signals are sensitive to dynamical processes connected with the cage opening mode. In particular, the amplitudes of the maxima of the $E_{du} = 1.2$ eV signal (cf. Figure 14) are decreasing during the time evolution of the system, which indicates that reverting to the cuboidal structure is less often accomplished from one oscillation period to the other. The reason for this is the restricted energy leaving IVR of the cage opening mode. From the decrease of the signal, one can roughly estimate the time scale for this type of IVR to be about 1 ps. In contrast, the average amplitudes of the oscillations of the $E_{du} = 0.8$ eV signal remain almost constant. This indicates that a somewhat constant part of the phase space volume oscillates periodically above the minimum structure (B). However, the modulation of the oscillations in the $E_{du} = 0.8$ eV signal is due either to anharmonicity of the cage opening mode or to resonant IVR which arises from the coupling of the other modes to the still dominant cage opening mode. The "minimum-region" signal ($E_{du} = 0.6$ eV) is aperiodic after 1 ps, and the intensity increases significantly, indicating that the phase space occupation in the minimum of the first excited electronic state (open cage structure (B) in Figure 11) rises during the propagation caused by the energy flow into this region. This restricted energy arriving IVR differs from the one-mode selective energy leaving IVR of the cage opening mode. The former cannot be attributed to one specific vibrational mode, in contrast to the latter one. Consequently, the time scales of both IVR processes are different. However, as can be seen from Figure 14, the simulation time of 2 ps is too short in order to determine the time scale for the restricted energy arriving IVR. It is important to notice that, although the system has fifteen degrees of freedom, no features of dissipative IVR are present during the propagation time of 2 ps and at low initial temperatures. This analysis of the restricted IVR processes may be useful for the development of mode selective control mechanisms of these or similar systems with metallic−ionic and metallic−covalent bonds.

4.2.2. Sodium Fluoride Clusters with Two Excess Electrons

For the accurate description of excited electronic states and exploration of ultrafast processes in sodium fluoride clusters with two excess electrons (e.g. Na_nF_{n-2}), the electron correlation treatment of two electrons which are not involved in the ionic bonding is mandatory. The leading features of their electronic properties are closely connected with the structures they assume. For structures in which two excess electrons are delocalized, dominant transitions appear in the visible regime, similar to the cases of pure metallic species. For structures in which two excess electrons are more localized, the intense transitions are located in the infrared regime, similarly as for F-centers. The corresponding prototypes of excited states have been found for the planar C_{2v} deformed rhombic structure of the Na_3F (isomer I), which belongs to the "metallic" class, and for the 3D trigonal pyramid (isomer II) (cf. Figure 15) with the F atom capping the Na_3 subunit, giving rise to the structure with less metallic character, respectively.[100,102] Recent experimentally obtained absorption spectra of Na_3F[412] confirm previous theoretical predictions.[100,102] In Figure 15 comparison between experimental and theoretical findings allows one to assign the planar rhombic structure of Na_3F to the measured features. The theoretical results shown in Figure 15 have been obtained using TD-DFT calculations with the gradient corrected Perdew−Burke−Erznerhof (PBE) functional (cf. section 2.1).[411] This shows that the TD-DFT method provides reasonable accuracy for the excited states of Na_3F compared with the full-CI results for two electrons, shown also in Figure 15, or with MRD-CI results from the early work.[100,102]

Therefore, the TD-DFT procedure represents the solid basis for molecular dynamics "on the fly" in excited states of this system, provided that the multireference description (which is not needed for vertical transitions) remains unnecessary at the time scale of ultrafast processes. In fact, semiclassical simulations of the pump−probe signals have been performed in the framework of the ab initio Wigner distribution approach described in section 3.2.1 in order to compare them with available experimentally

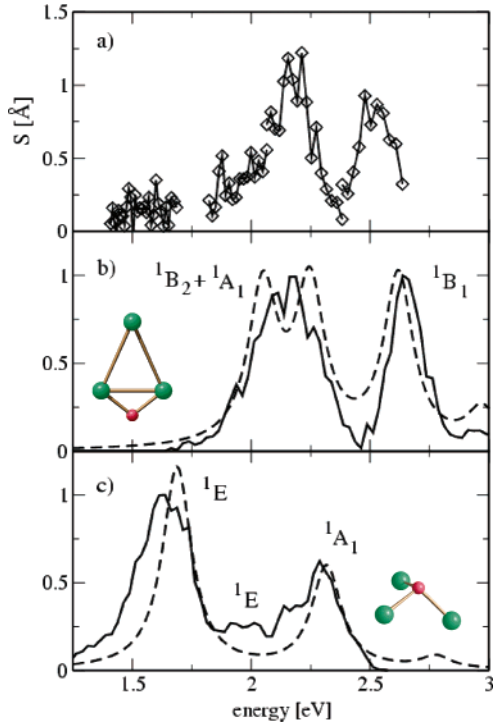

Figure 15. Comparison between experimental[412] (a) and theoretical[411] spectra (b and c) of Na_3F. Finite temperature absorption spectrum obtained from Monte Carlo simulation performed at 300 K (full line) and the TDDFT absorption spectrum (dashed line) obtained from a Lorentzian convolution of the vertical lines (b) for the rhombic isomer and (c) for the pyramidal isomer.

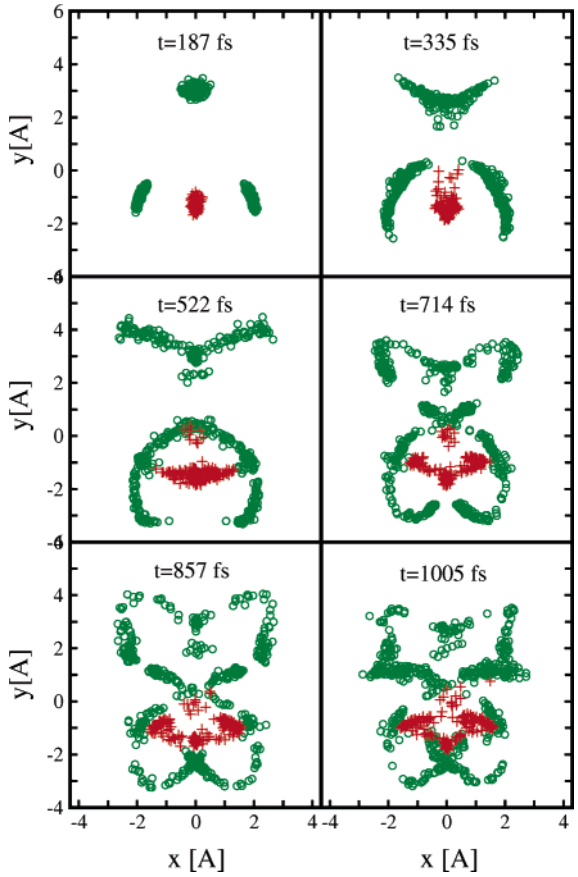

Figure 16. Snapshots of the atomic positions (F, +; Na, ○) propagated classically on the 1^1B_1 state for different times after the pump excitation.[125]

recorded spectra. For this purpose, an ensemble of trajectories was propagated on the third excited state of the 1^1B_1 symmetry (corresponding to the experimental probe energy) by solving the classical equations of motion. Forces were calculated "on the fly" in the framework of the TD-DFT method with the PBE functional and using an analytic formulation of the excited-state energy gradients.[211,212] The electronic excitation into the 1^1B_1 state induces geometric relaxation, which involves an oscillatory motion of the F-atom along the C_2 symmetry axis. The snapshots of the atomic positions at different times after the pump−pulse excitation for 200 trajectories are shown in Figure 16. As the initial condition, an ensemble corresponding to the temperature 50 K was generated by sampling the canonical Wigner distribution function in the harmonic approximation.[125] After 187 fs, the system reaches the configuration in which the Na−F−Na subunit is almost linear (cf. Figure 16), while, after 335 fs, the phase space density branches into two distinct parts. The larger part becomes reflected from the barrier which separates the C_{2v} structure from the pyramidal local minimum and oscillates back to the initial configuration with a period of ~320 fs. A smaller part of the phase density remains trapped in the basin corresponding to the pyramidal structure due to the flow of energy from the initially excited bending mode along the C_2 axis into other normal modes.

This periodical rearrangement is reflected in the pump−probe signal. Figure 17A shows the energy difference between the 1^1B_1 state and the cationic ground state as a function of time for 200 trajectories. As can be seen from eq 24, this quantity serves as a detection mechanism for the ultrafast vibrational dynamics; whenever this energy gap is smaller than the probe excitation energy, the system can be ionized, leading to an increase in the ion signal, which is shown in Figure 17B. To illustrate the connection between the dynamics and the pump−probe spectra, the times of the snapshots in Figure 16 were chosen in correspondence with the maxima and minima of the simulated ionization signal. Although the dynamics on the short time scale involves primarily the excitation of three totally symmetric normal modes, the classical simulations involving all degrees of freedom show that at later times also the nontotally symmetric modes start to participate in the dynamics, leading eventually to the breaking of some of the Na−Na bonds.[125]

A comparison between the experimentally measured pump−probe ion signal of Na_3F and theoretical simulations using the Wigner distribution approach, considering all degrees of freedom together with a quantum dynamical wave packet propagation in reduced dimensionality, is shown in Figure 17B. Assuming the constraint of the C_{2v} symmetry, three internal coordinates were used for the quantum wave packet propagation. Using a probe wavelength of 2.05 eV, the signals obtained from both theoretical approaches show strong oscillations, which are in good agreement with the experimental result,[412] for which $\omega_{pu} = 2.43$ eV and $\omega_{pr} = 2.04-2.08$ eV were used.[125]

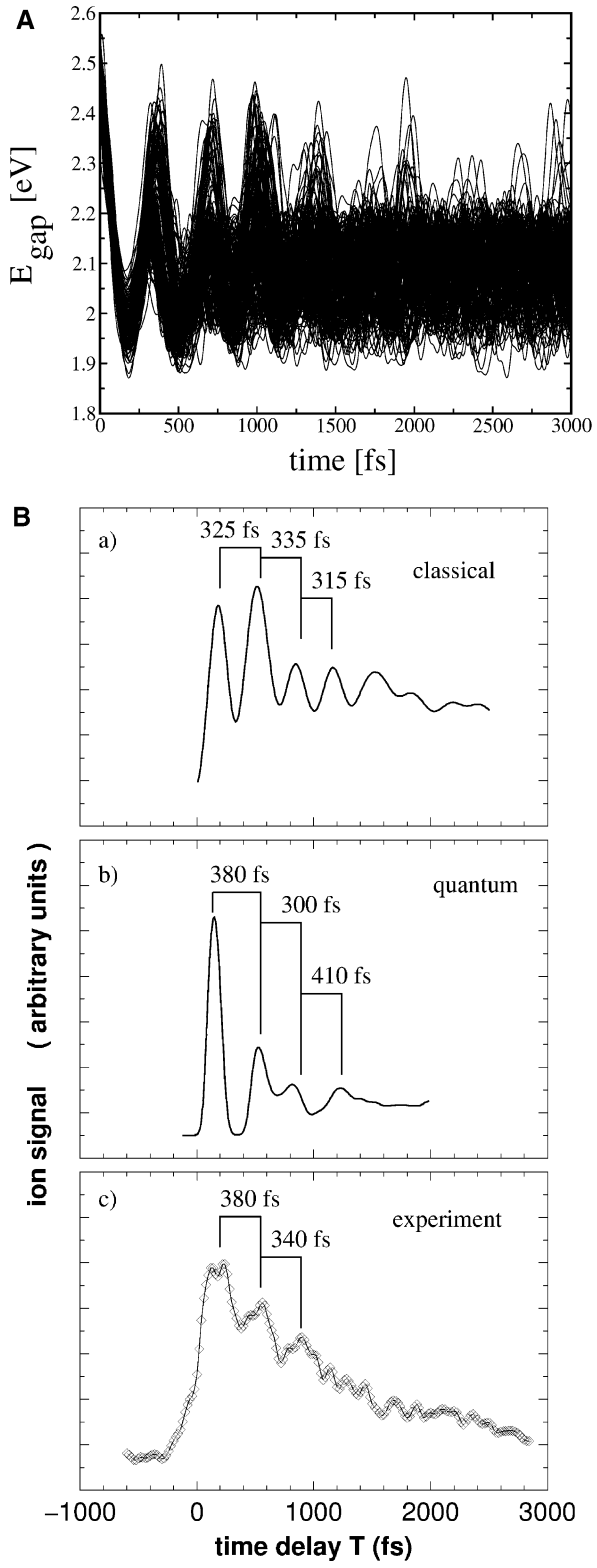

Figure 17. (A) Bunch of the energy gaps between the 1^1B_1 excited state of Na_3F and the cationic state during the dynamics in the 1^1B_1 state. (B) Comparison between theoretical pump−probe spectra of Na_3F obtained (a) from a semiclassical approach (combination of TDDFT and Wigner distribution approach) for all degrees of freedom and (b) from a quantum mechanical treatment for reduced dimensionality and (c) experimentally obtained signals.[125,412]

Despite small differences in the periods of the theoretical signals, both theoretical approaches agree upon the basic mechanism that is responsible for the observed oscillatory behavior. The signal reflects the ultrafast dynamics induced by the pump pulse which excites the rhombic structure of the cluster within the lower part of the 1^1B_1 state absorption band, causing a motion of the fluorine atom between outside and inside positions of the triangle formed by the three Na atoms. The ionization potential is smaller than the probe laser pulse at geometries corresponding to the fluorine atom being between two Na atoms. Therefore, the probe pulse can ionize the cluster, leading to the observed signal (cf. Figure 17B). After the fluorine atom has entered the Na_3 triangle, it rebounds and crosses the detection point a second time, arriving at almost the same geometry as in the case of the Franck−Condon transition (cf. Figure 16). The subsequent peaks in the ion signal correspond to the fluorine atom vibrating between these two geometries before it is trapped by IVR within the Na_3 triangle. For short times, the oscillations in the theoretical pump−probe signals are in very good agreement with the experimental ones. At later times, however, the simulated pump−probe signals remain constant while the experimental signal decays to zero. This is an indication that, at later times, other dynamical processes, such as relaxation via nonadiabatic transitions (not included in the simulations), play a significant role and eventually lead to depopulation of the 1^1B_1 state. This example illustrates that the Wigner distribution approach combined with MD "on the fly" based on the TD-DFT method provides the necessary accuracy for simulation of fs-signals and is applicable for systems with more degrees of freedom than the quantum mechanical propagation is able to handle.[125] This is true if the clusters do not contain very light atoms and if a sufficiently accurate description of the electronic properties is included.

4.3. Multistate Nonadiabatic Dynamics Involving Electronic Excited and Ground States: Simulation of Pump–Probe Signals

The breakdown of the Born−Oppenheimer approximation, due to avoided crossings or conical intersections between two electronic states, and consideration of nonadiabatic couplings and nonadiabaticity have been addressed in sections 3.1 and 3.2.2, for time-dependent quantum chemistry and nonadiabatic dynamics, respectively. The analytic expressions for the fs-signals involving nonadiabatic dynamics in the framework of the semiclassical Wigner distribution approach have been derived in section 3.2.2.

For this purpose, ab initio MD for at least two electronic states, as well as calculation of nonadiabatic couplings "on the fly", is needed if the adiabatic representation has been chosen.[116] Moreover, the connection between the analytic formulation of the first-order nonadiabatic couplings and one of the procedures for the treatment of nonadiabaticity must be established. In section 3.2.2 the MDQT, based on Tully's stochastic fewest switches procedure[349] (eqs 26−29), has been outlined, and eq 31 can be used for the simulation of pump−probe or pump−dump signals involving nonadiabatic dynamics using the Wigner distribution approach. The disadvantages of

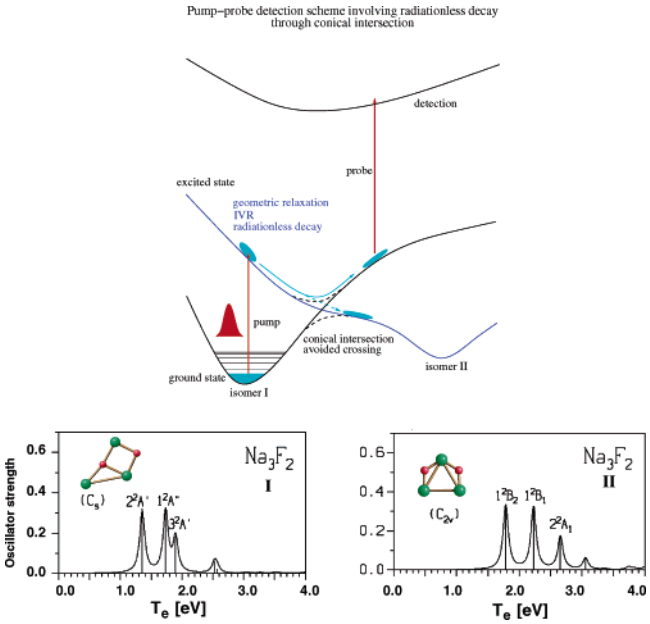

Figure 18. (top) Pump–probe scheme for the conical intersection. (bottom) Absorption spectra for two isomers (I and II) of Na_3F_2 obtained from the one-electron "frozen ionic bond" approximation.[116]

Tully's surface hopping approach and of the classical treatment of nuclei, which excludes the treatment of coherence effects, have also been addressed in section 3.2.2. However, in many systems involving radiationless isomerization processes through conical intersection from the first excited state, the quantum effects are washed out due to a high excess of energy, resulting in the high-temperature situation. In such cases, despite this limitation, the approach described above is reliable and practicable. It provides full information about underlying ultrafast processes from the analysis of the simulated signals, as will be shown for the example of the Na_3F_2 cluster.

4.3.1. Photoisomerization through Conical Intersection in the Na_3F_2 Cluster

The investigation of the nonadiabatic dynamics at the conical intersection between the first excited state and the ground state separating two isomers of Na_3F_2 (cf. Figure 18) offers an excellent opportunity to simulate fs pump–dump signals at a high level of accuracy. It also allows one to identify time scales of different ultrafast processes, including different kinds of bond breaking as well as radiationless transitions. For this purpose, it is adequate to use the combination of the Wigner–Moyal representation of the vibronic density matrix and ab initio multistate molecular dynamics in the ground state and in the first excited state without precalculation of energy surfaces, including the computation of the nonadiabatic couplings "on the fly". Analogous to adiabatic dynamics, an analytic formulation of nonadiabatic coupling in the framework of the "frozen ionic bonds" approximation, valid for nonstoichiometric alkali halide clusters with one excess electron which are used for calculation of nonadiabatic couplings "on the fly", is outlined in Appendix B.

At the same time, study of the dynamics in the first excited state of Na_3F_2 and the radiationless transition to the ground state allows for the prediction and verification of consequences of conical intersections in fs pump–probe signals in the gas-phase without the necessity to consider the environment. The latter complicates the issue, such as, for example, in the case of photochemistry in solution or in the case of the cis–trans photoisomerization of the visual pigment due to the influence of the protein cavity.[413,414]

Therefore, the photoisomerization in the Na_3F_2 cluster will be addressed in full complexity. First, the optical response (absorption spectra) and structural properties of the ground state and the first excited states of Na_3F_2 will be presented. Then, the conical intersection will be characterized. Finally, dynamics involving the passage through the conical intersection will be addressed, and simulated signals will be analyzed.

Optical Response Properties. The absorption spectra obtained for both isomers of Na_3F_2 using the "frozen ionic bonds" approximation (cf. Appendix A) are shown in Figure 18 and compare well with those calculated taking into account all valence electrons.[100] The lowest energy isomer I, with the ionic Na_2F_2 subunit to which the Na atom is bound (forming Na–Na and Na–F bonds), gives rise to the low energy intense transition in the infrared. This is a common feature found for Na_nF_{n-1} clusters due to the localized excitation of the one-excess electron, as addressed in section 4.2.1. In contrast, the transition to the first excited state of isomer II (C_{2v}) with the Na_3 subunit, which is bridged by two F atoms, has a higher energy close to the energies of transitions usually arising from excitations in metallic subunits. After the vertical transition at the geometry of isomer I, the geometric relaxation in the first excited state takes place, involving a breaking of the Na–Na bond leading to the first local minimum of the excited state (cf. Figures 19 and 20, structure A) with a moderate lowering of the energy. Afterward, the relaxation process proceeds to the absolute minimum with the linear geometry (cf. Figures 19 and 20, structure B), corresponding to the conical intersection, for which a further considerable decrease of energy takes place. The linear geometry of the conical intersection is also reached after vertical transition to the first excited state at the geometry of the second isomer with C_{2v} structure. Therefore, the investigation of the dynamics in the first excited state involves the breaking of metallic and ionic bonds starting from isomer I and just metallic bonds starting from isomer II, as well as the passage through the conical intersection.

As a consequence, one expects strong thermal motions within the ensemble, leading to phase space spreading and IVR. All processes can be monitored by a second ionizing probe pulse with excitation energies between ~2.9 and ~4.8 eV, as shown by the scheme given in Figure 19. The first value is close to the initial Franck–Condon transition region and probes the relaxation dynamics on the first excited electronic state before the branching process due to the conical intersection occurs. The latter value allows one to monitor the processes involved in the ground-state dynamics after passage through the conical intersection.

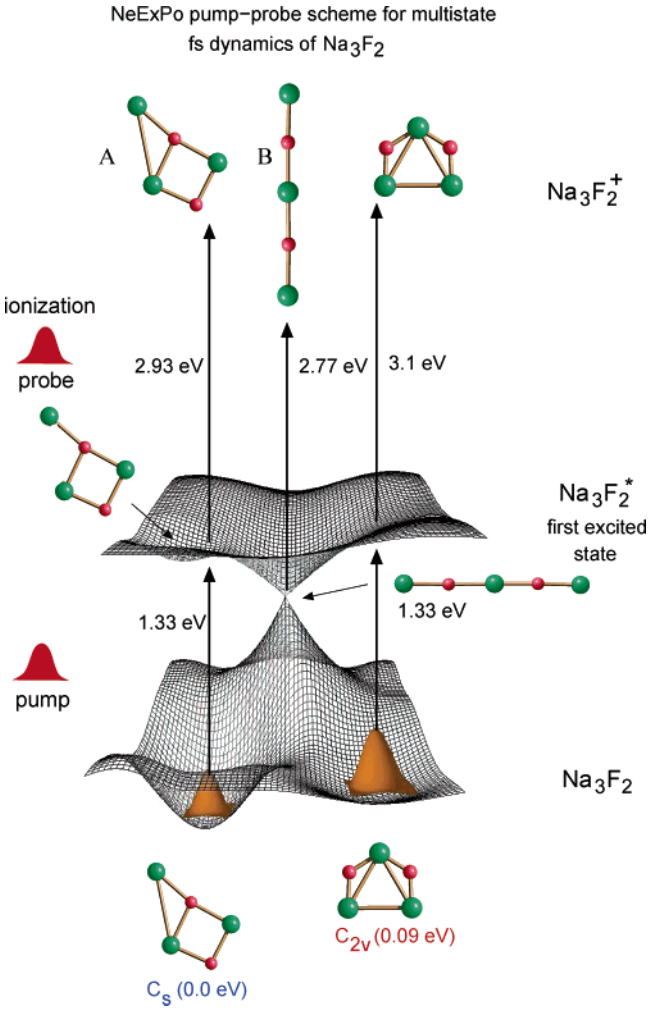

Figure 19. Scheme of the multistate fs-dynamics for NeExPo pump−probe spectroscopy of Na_3F_2 including the conical intersection with structures and energy intervals for the pump and probe steps.[116]

Conical Intersection. The algorithm introduced by Robb et al.[415] is very useful for the determination of the lowest energy structure and the energy at the intersection seam (cf. Figure 20) as well as for analyzing the topology of the intersection in the space spanned by the internal degrees of freedom. The results obtained for the linear geometry of Na_3F_2, which has $N = 10$ internal degrees of freedom, show that displacements in 8 out of the 10 directions almost do not change the energetic separation of the surfaces, while displacements in the orthogonal plane characterized by two directions, X_1 and X_2, strongly remove the energy degeneracy. X_1 is the gradient difference vector, and X_2 involves the coupling vector between the two states. In other words, the ground-state reaction pathways starting in the plane X_1X_2 connect the excited-state reactants with the two ground-state products. Thus, the intersection of the ground state and the first excited state has the shape of a double cone, with respect to X_1 and X_2, where the apex spans an eight-dimensional hyperline along which the energy is degenerate. The intersection seam is therefore $(N - 2)$ dimensional, as is characteristic for *conical intersections*.

The analysis of the wave functions of the ground state and the first excited state in the close neighborhood of the conical intersection yields positive and negative linear combinations of two "valence-bond-like" structures: $Na^+-F^--Na^+-F^--N^\bullet \pm Na^\bullet-F^--Na^+-F^--Na^+$. One of them contributes dominantly to the ground state, and the other one contributes to the first excited state, thus giving rise to two states with different symmetries. The location of the excess electron is indicated by the dot above the sodium atom. Of course, at the point of the conical intersection, the arbitrary linear combination of the above "valence bond" (VB) structures is possibly due to degeneracy. The two VB structures differ in the translocation of the single excess electron or of the charge from one end to the other of the linear system. In other words, the length of the linear chain is sufficiently long to allow for an energy gap closing, in analogy to the dissociation limit of the H_2^+ molecule for which the degeneracy of the ground state and the excited state occurs due to equal energies of the $H^\bullet-H^+$ and $H^+-H^\bullet$ structures. This means that, in the case that the linear molecule is not sufficiently long to minimize the repulsion, avoided crossing will take place, as occurs in Na_2F, which turns into the conical intersection for Na_3F_2. In other words, the presence of the conical intersection in the latter case through which the isomerization process can take place is the consequence of the electronic structure properties. Therefore, due to general characteristics, it can be found for other systems by designing the analogous electronic situation.

In fact, the analogy can be drawn to conical intersections found in organic photochemistry involving biradicaloid species, which are generated by partial breaking of double heterobonds due to geo-

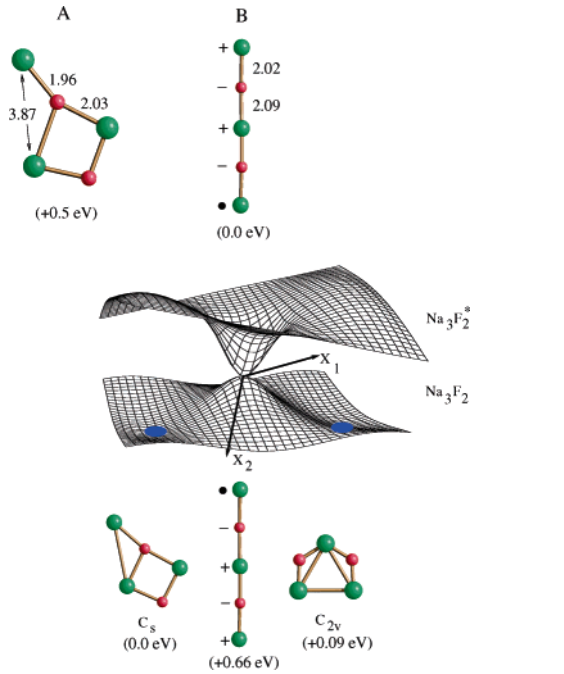

Figure 20. (top) Structures corresponding to the local minimum (with a broken Na···Na bond) and to the global minimum (linear) on the first excited state of Na_3F_2. (bottom) Sketch of the conical intersection between the first excited state ($Na_3F_2^*$) and the ground state characterized by the two vectors $\mathbf{X}_1$ and $\mathbf{X}_2$ together with the structures of the isomers and of the conical intersection and their relative energies.[116]

metric relaxation in the singlet excited states. The condition for the occurrence of conical intersections in so-called "critical biradicals" has been formulated in the framework of the two-orbital, two-electron model and can be fulfilled in the case that the electronegativity difference between the two centers is sufficient to minimize the repulsion between the ground state and the excited states.[317] This occurs in the protonated Shiff bases by twisting of the chromophore $H_2C-N^+H_2$ bond, leading to cis−trans isomerization. In this case, the ground and excited states at the conical intersection are characterized by "VB" structures $H_2C^{\bullet}-N^{\bullet+}H_2$ and $H_2C^+-N^{\bullet\bullet}H_2$, which differ in translocation of charge from one center to the other of the chromophore.[317] In fact, it has been confirmed experimentally that the conical intersection is responsible for the cis−trans isomerization of the retinal chromophore in the vision process.[413,414]

However, investigation of the nonadiabatic dynamics through the conical intersection of the Na_3F_2 cluster has advantages. The system has 10 degrees of freedom and permits the calculation of an ensemble of trajectories based on the accurate ab initio description of the excited and ground electronic states and on the corresponding MD. Thus, it provides the conceptual framework for fs-observables, such as fs pump−probe signals, which will be addressed below.

Nonadiabatic Dynamics. In the framework of the "frozen ionic bonds" approximation, all requested ingredients, such as gradients of energies as well as nonadiabatic couplings, are available. They have been formulated in Appendices A and B and can be straightforwardly inserted in eqs 26−29 and used for the nonadiabatic dynamics "on the fly" (e.g. passage through the conical intersection).[116]

To obtain initial conditions, a canonical thermal ensemble of 50 K can be determined by the Wigner distribution function of the electronic ground state including all normal modes ω_i, $i = 1, ..., 10$, of the C_s structure, corresponding to the total minimum of energy according to eq 47. The set of, for example, 100, initial conditions can be obtained by sampling the Wigner distribution function with respect to the coordinates $\mathbf{q}_0$ and momenta $\mathbf{p}_0$, which can be used for the classical trajectory simulations on the first excited state of Na_3F_2. The finite temperature of 50 K causes thermal deviations from the energy minimum C_s structure. These have been characterized by the histogram of the abundances of the energy gaps between the first excited electronic state and the ground state, corresponding to the Franck−Condon transition probabilities shown in Figure 21. The maximum corresponds to the energy gap value between the ground state and the first excited state at the C_s structure of Na_3F_2.

Important aspects of analysis of the nuclear dynamics will be addressed first. The simulation of the classical trajectory ensemble, consisting of a large number of sampled phase space points, can be started on the first excited electronic state. The geometric relaxation (over the local minimum) toward the linear structure corresponding to the conical intersection and its passage as well as the subsequent relaxation

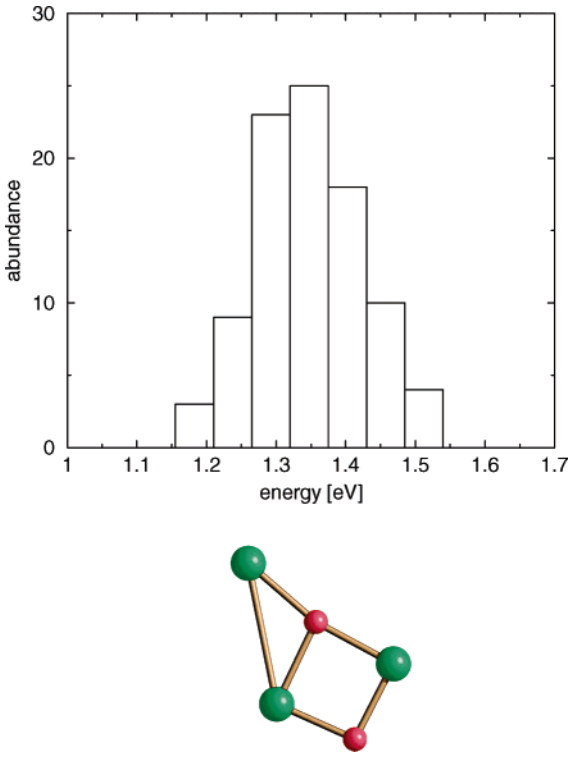

Figure 21. Franck−Condon transition probabilities in terms of abundances of the energy gaps between the first excited electronic state and the ground state of Na_3F_2 for a 50 K initial temperature ensemble.[116] Reprinted with perimission from ref 116. Copyright 2001 American Institute of Physics.

dynamics on the electronic ground state can be visualized by considering the phase space density of the cluster ensemble shown in Figure 22 for different propagation times. At the beginning, $t = 0$ fs, the phase space density is localized, corresponding to the C_s structure (cf. Figure 22). During the subsequent ∼90 fs, the distance between the Na−Na atoms elongates, indicating the bond breaking between both sodium atoms, and corresponds to a local minimum on the first excited state (cf. Figure 22). Consecutive ionic bond breaking between the Na and the F atoms of the Na_2F_2 subunit can be observed after 220 fs (cf. Figure 22) together with a small delocalization of the phase space density. After ∼400 fs, the region of the conical intersection corresponding to the linear structure is reached (cf. Figure 22). This triggers the branching of the phase space density from the excited electronic state to the ground state. At this stage, the system gaines an additional kinetic energy of ∼0.67 eV. Due to this large vibrational excess energy, strong anharmonicities between the vibrational modes are present, which are responsible for the phase space spreading. The subsequent relaxation dynamics on the electronic ground state is characterized by an even larger phase space spreading, particularly after 800 fs. This is due to the fact that the vibrational excess energy rose to ∼1.3 eV, which corresponds to an equilibrium temperature of ∼3400 K (cf. Figure 22). However, despite increasing phase space spreading, structural information of the cluster ensemble can be gained up to a propagation time of ∼800 fs by considering the center of mass positions of the atomic phase space distributions in Figure 22. In particular,

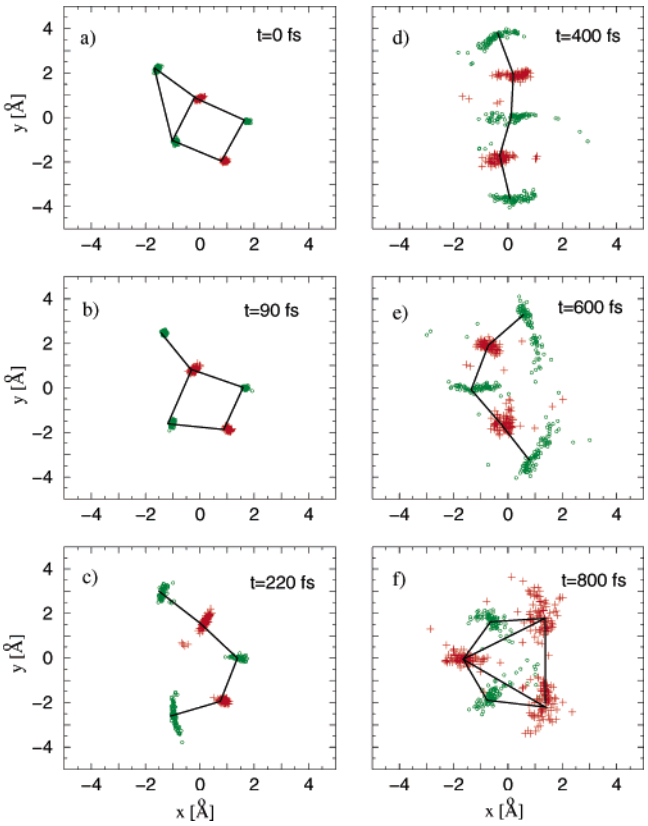

Figure 22. Snapshots of the phase space distribution (PSD) obtained from classical trajectory simulations based on the fewest-switches surface hopping algorithm of a 50 K initial canonical ensemble.[116] Na atoms are indicated by green circles and F atoms by red crosses. (a−c): Dynamics on the first excited state starting at the C_s structure (a) over the structure with a broken Na−Na bond (b) and, subsequently, over a broken ionic Na−F bond (c) and toward the conical intersection region (d). (d−f): Dynamics on the ground state after branching of the PSD from the first excited state leads to strong spatial delocalization. The C_{2v} isomer can be identified at ∼800 fs in the center-of-mass distribution (f).

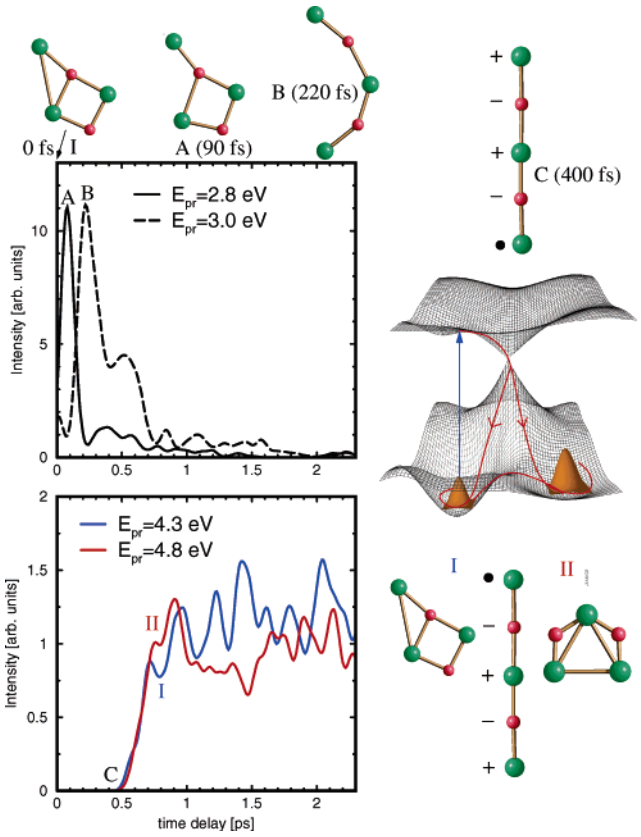

Figure 23. Simulated NeExPo pump−probe signals for the 50 K initial temperature Na_3F_2 ensemble at different excitation energies of the probe laser monitoring the geometric relaxation on the first excited state involving bond-breaking processes and passage through the conical intersection as well as geometric relaxation and IVR processes on the ground state after the passage (left side). The isomerization through the conical intersection is schematically illustrated on the right-hand side.

the "center of mass geometry" at 800 fs is close to the C_{2v} structure. However, due to the phase space spreading, there are also considerable deviations, and even geometries close to the C_s structure are involved in the phase space distribution of the cluster ensemble. As shown below, one can obtain detailed information about the ratio between these structures as well as energetic distributions in the cluster ensemble from pump−probe signals. For times beyond 1 ps, no structures can be identified in the phase space distribution. The ensemble is geometrically completely delocalized at least up to the propagation time of 2.5 ps, which is understandable due to the large vibrational excess energy.

In summary, the dynamics through the conical intersection represents an elementary physical event for the cluster ensemble in the sense that it initiates the transition from structurally and energetically localized behavior involving consecutive metallic and ionic bond breaking processes to delocalized behavior. Thus, the molecular dynamics might be divided into a reversible and an irreversible part separated by the passage through the conical intersection.

Pump−Probe Signals. Simulations of signals are based on eq 31, with energy gaps obtained from the classical trajectory simulations using the fewest switching surface hopping algorithm (eqs 26−29) for the ensemble at an initial temperature of 50 K (eq 47). To obtain comprehensive information on the dynamical processes of Na_3F_2, a zero pump pulse duration ($\sigma_{pu} = 0$) is suitable, which involves a complete excitation of the ground-state ensemble prepared at the initial temperature. The ultrafast structural relaxation processes involving the bond breaking can be resolved using a probe pulse duration of 50 fs. The simulations of the signals are shown for four different excitation energies (wavelengths) of the probe pulse in Figure 23:

(i) $E_{pr} = 2.8$ eV and $E_{pr} = 3.0$ eV correspond to transition energy values between the first excited state and the cationic state at the time of the Na−Na metallic and the Na−F ionic bond breaking, respectively (cf. Figure 19). Thus, the signals for the above transition energies provide information on the structural relaxation involving the bond breaking processes in the first excited state of Na_3F_2 before the conical intersection is reached. In fact, they exhibit maxima at ∼90 and ∼220 fs (cf. Figure 23), in agreement with the time scales for the metallic and ionic bond breaking obtained from the analysis

of the phase space distribution shown in Figure 22. Both signal intensities decrease rapidly after 0.4−0.5 ps, indicating the branching of the phase space density from the first excited electronic state to the ground state due to the conical intersection.

(ii) $E_{pr} = 4.3$ eV and $E_{pr} = 4.8$ eV (cf. Figure 19) correspond to transition energies between the ground state and the cationic state at the C_s geometry and the C_{2v} geometry, respectively. In such a way, the signals shown in Figure 23 monitor the ratio of both isomers in the phase space distribution after the passage through the conical intersection up to a time delay between pump and probe of ~1 ps. This time represents the limit up to which structural information can be resolved in the phase space distribution (cf. Figures 22 and 23). For larger time delays, the signals provide only information about the energetic redistribution, thus the IVR. In fact, the intensities of both signals start to increase after ~0.4 ps, since the ground state becomes populated, providing the time scale for the passage through the conical intersection (cf. Figure 23). Furthermore, the signal at $E_{pr} = 4.8$ eV exhibits a maximum at 0.8−0.9 ps, indicating the larger ratio of the C_{2v} structure in correspondence with the results obtained from the phase space distribution (cf. Figure 22). This signal drops rapidly after 0.9 ps, and the signal at $E_{pr} = 4.3$ eV increases, indicating that the C_s structure is more populated at 0.9−1.0 ps (cf. Figure 23). The latter also exhibits oscillatory features beyond 1 ps, corresponding to the IVR regime. This leads to the conclusion that a somewhat periodic energy flow is present in the cluster ensemble. However, due to the high vibrational excess energy, these oscillations cannot be attributed to particular normal modes.

In summary, these results provide information about the system in full complexity. They show that different ultrafast processes, which are initiated by the Franck−Condon pump pulse transition to the first excited electronic state, are involved in the dynamics of the Na_3F_2 cluster. These include geometric relaxation, consecutive bond breaking of metallic and ionic bonds, passage through the conical intersection, and IVR processes.[116] Moreover, the time scales of these processes can be identified in the pump−probe signals, and each of them can be selectively monitored by tuning the probe excitation energy. However, to populate only one of the isomers, the pathway has to be found which avoids a large excess of energy through the conical intersection. This offers the opportunity to tailor laser pulses that will drive the system into the desired target, and will be addressed in section 5. Similar situations can be expected in considerably larger systems, providing that the characteristic electronic aspects remain preserved.

4.4. Full Quantum Mechanical Multistate Dynamics of Small Systems and fs-Signals

The importance of using femtosecond lasers in probing molecular dynamics, in obtaining accurate spectroscopic information (e.g. vibrational and rotational structure), and in manipulating ultrashort processes has been successfully illustrated for the examples of diatomic and triatomic molecules. Pioneering experiments on the photodissociation reactions of ICN[185] and NaI performed by Zewail and coworkers,[186,187] on femtosecond temporal spectroscopy (FTS) on iodine I_2,[187] and on fs-time-resolved molecular multiphoton ionization on Na_2 by Gerber and co-workers[132,182] are typical examples which stimulated theoretical work to provide the basis for the identification of underlying ultrafast processes in the measured features. For this purpose, the methods developed by Williams and Imre[416,417] and Engel and Metiu[418,372,256] have been extremely useful.

In the case of NaI, different temporal behaviors of two reaction channels due to the crossing between the ionic ground state and the covalent excited state were identified by joint experimental and theoretical efforts.[185,186] Either the wave packet is trapped on the adiabatic excited state surfaces without crossing, or it crosses the diabatic surface. Therefore, the oscillations, dephasing, and recurrences are present, and the different natures of the dynamics at short and long times were identified. The early time behavior was reproduced by classical mechanics, but for dephasing and spread in the chaotic region, the quantized packet is necessary.[185,186] Comparison of experimental and theoretical results on the example of I_2[187,256] demonstrated the ability of femtosecond temporal spectroscopy (FTS) to provide high-resolution spectroscopic information in the time domain, allowing one, in principle, to solve the inversion problem, for example, reconstruction of the potential energy surface.[187]

In the fs-time-resolved multiphoton ionization experiments by Gerber and co-workers,[132,182] two different photoionization processes in measured pump−probe ionization and photofragmentation spectra have been identified. The first is the direct photoionization of an excited state in which one photon creates the wave packet in the first excited state ($A^1\Sigma_u^+$) and the two photon probe transfers that motion from the inner turning point via the second excited state ($2^1\Pi_g$) into the ionization continuum of Na_2^+ ($^2\Sigma_g^+$). The time-dependent quantum calculations reproduced the measured features, reflecting the wave packet harmonic motion in the bound $A^1\Sigma_u^+$ state for short times as well as the spreading and recurrences at longer times.[182] In the second process, two photons created a wave packet in the $2^1\Pi_g$ state and one photon transferred its motion from the outer turning point into the ionization and fragmentation continuum via a doubly excited bound Na_2^{**} state. In fact, it will be shown in section 5.2 that these experiments have provided the verification of the Tannor−Rice single-parameter control,[126,127] since for different time delays the different reaction channels, either $Na_2 \rightarrow Na_2^+ + e^-$ or $Na_2 \rightarrow Na^+ + Na + e^-$, were favored.

Joint experimental and theoretical studies of multiphoton ionization processes on K_2,[184] Cs_2,[419,420] and Li_2[138] revealed similarities and differences with processes found in Na_2, which stem from different characteristic features of the PES for excited states of neutral and cationic species of these systems as well as from experimental conditions. Furthermore,

the fs-dynamics of mixed dimers, such as the vibrational wave packet dynamics of the $A^1\Sigma^+$ state of NaK[188] and its fractional revivals,[189] has been investigated experimentally.

Upon increasing the size by adding only a single atom, pure and mixed alkali trimers offered a wealth of new phenomena which have been investigated experimentally using fs pump−probe spectroscopy and elucidated theoretically. They are connected (i) with the nonrigidity of nuclei, giving rise to multiple minima on the potential energy surface due to Jahn−Teller or pseudo-Jahn−Teller effects, and (ii) with the presence of many electronic states in a narrow energy interval requesting the consideration of nonadiabaticity. Therefore, despite their small size, trimers represent a challenge for experimental techniques and for theoretical treatments due to the interplay between their complex electronic structure and nuclear dynamics. The real time investigations of the ground and excited states of Na_3 trimers by fs-spectroscopy allowed identification of pseudorotational wave packet motions in some of the states (e.g. ground state[192] and (B) excited state[192]) as well as ultrafast fragmentations in other ones[421] (e.g. C- and D-state). Moreover, it has been recognized that the observations of the processes mentioned above are strongly dependent on experimental conditions, such as the duration of the laser pulses or the strength of the laser fields. For example, different fs pump−probe experimental spectra obtained for the B state of Na_3 using different pulse durations (such as short (300 fs) and long (3 ps)) were assigned to a fast symmetric stretching vibration and to slow pseudorotational wave packet motion, respectively. This is based on quantum mechanical calculations.[193] In addition to the variation of the pulse length, it has been shown theoretically that the change of the pulse strength or carrier frequency can be used to excite radial or pseudorotational motions in different states (e.g. ground or excited state).[194] In the case of K_3, the theoretical predictions of an excited state located at ~800 nm[195] initiated fs-experiments[196] which provided evidence that wave packet propagation and ultrafast photodissociation can occur simultaneously in the excited state, which could not have been accessed earlier by CW spectroscopy. Furthermore, photodissociation of excited Na_n ($n = 3-10$)[183,198] and K_n ($n = 3-9$)[197] clusters has been studied as a function of cluster size, demonstrating that different photodissociation dynamics occurs in these two series of clusters due to the different natures of their excited states. This has also been confirmed by time-resolved observation of bound−free transitions in mixed Na_2K and K_2Na trimers.[199] In the case of Na_2K, the vibrational dynamics in the predissociated state was monitored in addition to fragmentation of NaK, while, in the case of K_2Na, no wave packet dynamics was resolved due to the short lifetime of the predissociated excited state of this trimer. The above different characteristics of both mixed trimers are closely related to the different natures of the excited states of the Na_2- and K_2-subsystems.

Complementary theoretical investigation of dynamics in the excited state of Na_2K involves a large number of excited states which undergo nonadiabatic couplings. Preliminary results of pump−probe signals obtained from semiclassical nonadiabatic dynamics based on good quality 3D energy surfaces indicate that the fragmentation of NaK occurs, involving passage through conical intersections and avoided crossings. Therefore, despite the relatively good agreement between leading features of theoretical and experimental pump−probe spectra, it is still challenging to identify conditions under which fs pump−probe signals exhibit the signature of periodic motion within individual excited states.[422]

All these fs pump−probe investigations were prerequisites for applying different control schemes which will be addressed in section 5.

5. Tailored Laser Fields and Analysis of Processes by Control

5.1. Optimal Control Theory and Closed Loop Learning Control

As briefly outlined in section 2.3, tailored laser pulses are appropriate for exciting different superpositions of eigenstates by coherent control, creating wave packets which are directed to a desired target state. Optimal control theory (OCT)[240−244] and closed loop learning control (CLL),[245] which takes advantage of modern pulse shaping techniques,[11] have successfully been applied to systems of different complexity.[57−76,248,423] Both involve an iterative procedure as shown in Figures 24 and 25. The scheme for CLL used in experimental setups is also shown in Figure 25.

In optimal control theory, the optimized pulses are obtained from the functional in the framework of the variational method:[243]

$$J = \langle \psi(T)|\hat{P}|\psi(T)\rangle \tag{49}$$

J is the functional of the radiation field $\epsilon(t)$. Therefore, the maximization has to be carried out with respect to the variation of the functional form of $\epsilon(t)$ which involves temporal shape and spectral content. $\hat{P}$ is the projector operator which selects the desired target. For example, one can choose the model for two potential energy surfaces, and the ground state has two isomers (I and II), as shown in Figure 24.

A constraint that the energy per pulse is limited is given by

$$E = \int_0^T \mathrm{d}t\ |\epsilon(t)|^2 \tag{50}$$

which, together with eq 49, implies that the following functional must be optimized:

$$J_\alpha = \langle \psi(T)|\hat{P}_\alpha|\psi(T)\rangle - \lambda[\int_0^T \mathrm{d}t\ |\epsilon(t)|^2 - E], \quad \alpha = \text{isomer I, isomer II} \tag{51}$$

Here λ is a Lagrange multiplier.

If one imposes the constraint that the Schrödinger equation must be satisfied, the modified objective

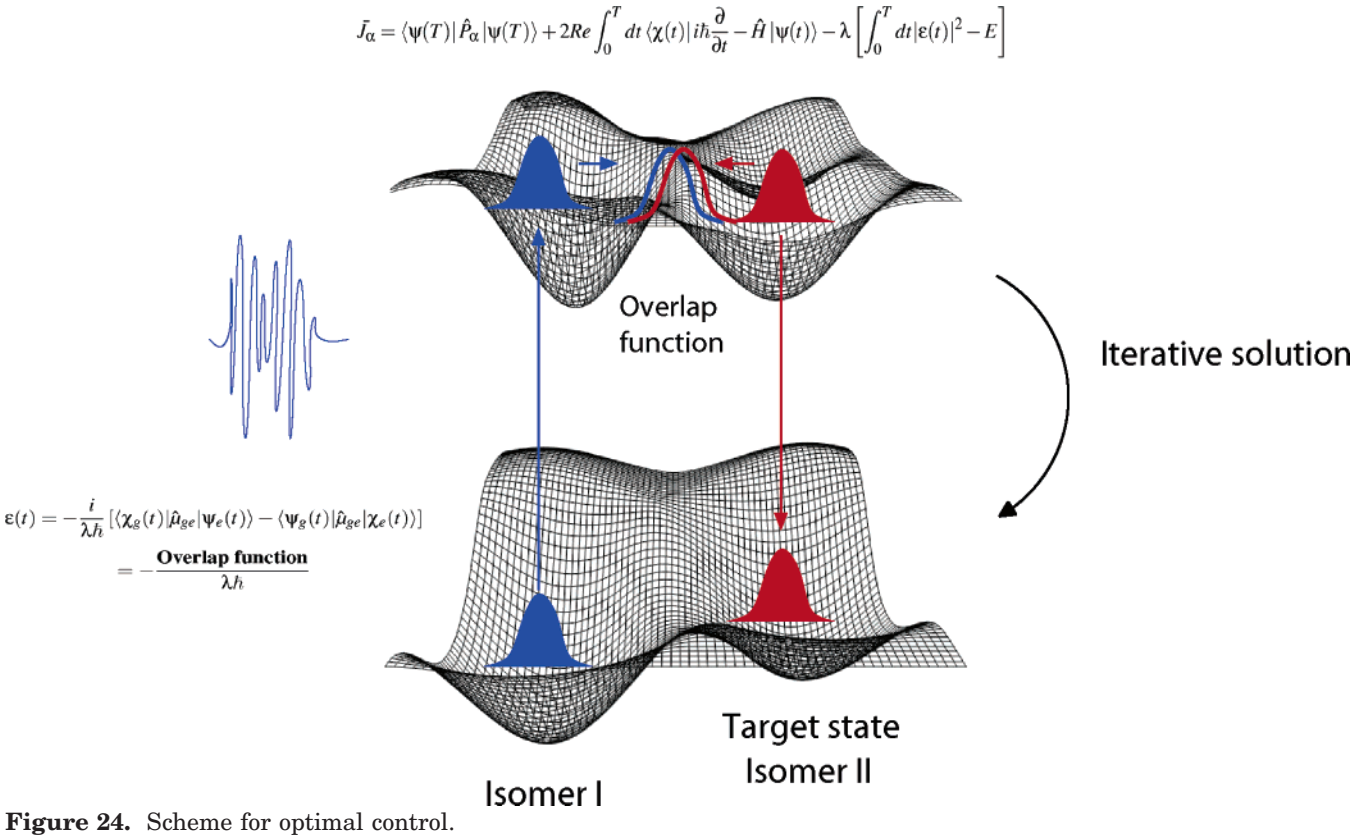

Figure 24. Scheme for optimal control.

functional, which should be optimized, takes the following form:

$$\overline{J_\alpha} = \langle\psi(T)|\hat{P}_\alpha|\psi(T)\rangle + 2Re\int_0^T \mathrm{d}t\left\langle\chi(t)\middle|i\hbar\frac{\partial}{\partial t} - \hat{H}\middle|\psi(t)\right\rangle - \lambda[\int_0^T \mathrm{d}t\ |\epsilon(t)|^2 - E] \quad (52)$$

If $\psi(t)$ satisfies the time-dependent Schrödinger equation, the second term on the right-hand side of eq 52 vanishes for any $\chi(t)$, and the third term is zero when $\epsilon(t)$ satisfies eq 50. Both of these terms allow variations of $\overline{J_\alpha}$ with respect to $\epsilon(t)$ and $\chi(t)$ independently to the first order in $\delta\epsilon(t)$.

The condition $\delta\overline{J_\alpha}/\delta\psi = 0$ generates a partial differential equation for the Lagrange multiplier function $\chi(t)$

$$i\hbar\frac{\partial\chi(t)}{\partial t} = \hat{H}\chi(t) \quad (53)$$

which is the time-dependent Schrödinger equation subject to the final condition

$$\chi(T) = \hat{P}_\alpha\psi(T) \quad (54)$$

and a partial differential equation for $\psi(t)$

$$i\hbar\frac{\partial\psi(t)}{\partial t} = \hat{H}\psi(t) \quad (55)$$

subject to the initial condition

$$\psi(0) = \psi_0 \quad (56)$$

Finally, the optimal applied field is defined by the condition $\delta\hat{J}_\alpha/\delta\epsilon(t) = 0$, which leads to

$$\epsilon(t) = -\frac{i}{\lambda\hbar}[\langle\chi_g(t)|\hat{\mu}_{ge}|\psi_e(t)\rangle - \langle\psi_g(t)|\hat{\mu}_{ge}|\chi_e(t)\rangle] \quad (57)$$

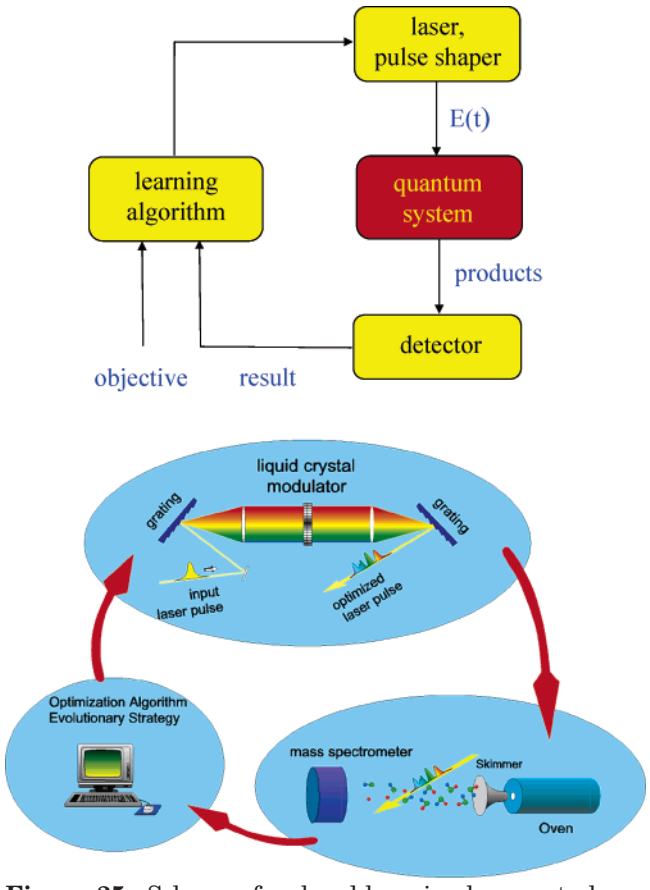

Figure 25. Schemes for closed learning loop control.

with

$$\lambda^2 = \frac{1}{E}\int_0^T \mathrm{d}t\ |\langle\chi_e(t)|\hat{\mu}_{eg}|\psi_g(t)\rangle - \langle\psi_e(t)|\hat{\mu}_{eg}|\chi_g(t)\rangle|^2 \quad (58)$$

where μ_{eg} is the dipole operator and the indices e and g label the excited-state and the ground-state energy surfaces. The equation of motion of the coupled amplitudes on the two potential energy surfaces reads

$$i\frac{\partial}{\partial t}\begin{pmatrix}\psi_e\\ \psi_g\end{pmatrix} = \begin{pmatrix}\hat{H}_e & \hat{V}_{ge}\\ \hat{V}_{eg} & \hat{H}_g\end{pmatrix}\begin{pmatrix}\psi_e\\ \psi_g\end{pmatrix} \quad (59)$$

with the interaction potential $\hat{V}_{ge}$ defined as $\hat{\mu}_{ge}\epsilon(t)$.

The numerical calculations then involve an iterative procedure which includes the following:

(i) initial guess for the pulse shape $\epsilon(t)$;

(ii) integration of the Schrödinger equation forward starting from the initial condition in the ground state;

(iii) application of the projector operator which selects the target (the exit channel to $\psi(t)$) to obtain $\chi(t)$ as an initial value for backward propagation;

(iv) propagation of $\chi(t)$ backward in time;

(v) during the propagation, calculation of the overlap function

$$O(t) = i[\langle\chi_e(t)|\hat{\mu}_{eg}|\psi_g(t)\rangle - \langle\psi_e(t)|\hat{\mu}_{eg}(t)|\chi_g(t)\rangle] \quad (60)$$

and

(vi) after completion of the backward propagation, renormalization of the result needed to obtain the new pulse

$$\epsilon(t) = O(t)\left(\frac{1}{E}\int_0^T \mathrm{d}t\ \left|O(t)\right|^2\right)^{-1/2} \quad (61)$$

(vii) iterative procedures starting from step ii should be repeated until convergence has been achieved. The above outlined procedure in the simplified form is schematically given in Figure 24 (cf. refs 237 and 243).

Of course the CLL technique represents a powerful tool for optimization of the desired yield, but it does not provide information about the quantum system itself or about the processes involved. As shown in Figure 25, the laser system and the pulse shaper are used to produce the electric field $\epsilon(t)$ which interacts with the quantum system initiating photochemical or photophysical processes. After detection of the products, a learning algorithm based on evolutionary algorithms[246,247] produces a new electric field based on experimental input and the defined objective. This loop is then repeated until the optimized laser pulses give rise to the aimed yield. This technique opened new roads in the field, in particular, concerning the optimization of the yield of the chosen reactivity channels.[11] Furthermore, technological developments such as laser pulse compression and pulse cleaning techniques (cf. ref 11 and references therein) are valuable for producing stable pulse forms. This is particularly important in the case of complex systems. However, only the comparison between the tailored pulses obtained from optimal control theory (OCT) and those obtained from the CLL technique can provide insight into the processes and the system itself and, therefore, can also address the inversion problem.

There are two important aspects which we wish to address in connection with the scope of optimal control theory. The question to be answered is whether the shapes of the optimized pulses can be used to unravel mechanisms of underlying processes, in particular when several excited states are involved. If the answer is positive, the control can be employed as a tool for analysis. This issue will be addressed in section 5.2. Moreover, for the systems with increasing complexity, the question is raised whether conditions can be found under which the controllability can be ensured. In this context, the required information about the complex systems, in terms of multidimensional potential energy surfaces, is usually not available. However, development of dynamics "on the fly" has drastically changed the situation. In particular, for a very short pulse limit, the classical quantum mechanical correspondence between a trajectory and a wave packet can be used to describe the system and its time evolution. The ensemble of classical trajectories of a Wigner swarm representing the wave packet accurately mimics the quantum mechanical flow of amplitude, permitting use of semiclassical simulations in connection with optimal control theory. This simplified picture has an enormous advantage because it provides information about the system and time-dependent processes involved, as will be shown in section 5.3.

5.2. Single-Parameter and Multiparameter Control in Small Systems: Analysis of Processes by Control

Investigation of simple systems offers a possibility to learn how to use control as a tool for analyzing the underlying processes. Therefore, metallic dimers[136−141,154,191,250,424] and diatomic molecules[250,272] have been studied in numerous contributions. This is due to the fact that they are suitable model systems for establishing scopes of different control schemes and because they became easily accessible to experimental pulse shaping techniques.[142−153] In fact, experimental work on Na_2,[183] using one-parameter control, was the first confirmation of the simple Tannor−Rice control scheme.[126,127] By varying the time delay between the first and second pulses, Gerber and co-workers investigated competition between ionization and dissociative ionization of Na_2 ($Na_2 \rightarrow Na_2^+ + e^-$ versus $Na_2 \rightarrow Na^+ + Na + e^-$; cf. section 4.4). Consequently, the ratio of molecular to atomic ion products Na_2^+/Na^+ oscillates with the change in the time delay between the pump and probe pulses with the period determined by the motion of the wave packet as shown in Figure 26. Control over the branching between the Na^+/Na_2^+ channels was also achieved by using the given laser wavelengths. With these, a different sequence of states in Na_2, which involves a double minimum potential energy surface, was reached, as shown in

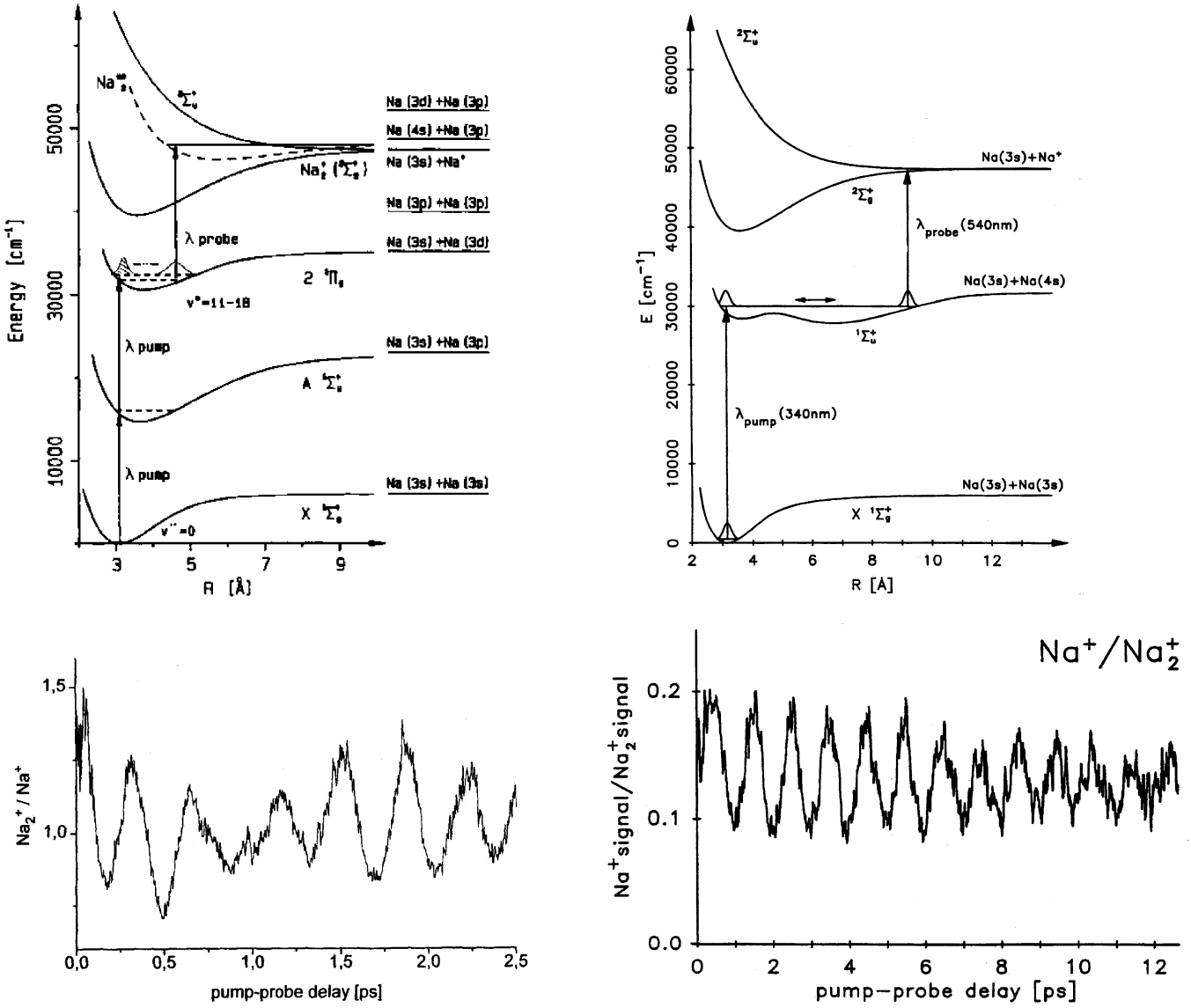

Figure 26. (top) Potential energy curves for Na_2 and Na_2^+ illustrating the Tannor−Rice control of the photoionization in Na_2 involving the $2^1\Pi_g$ state (left side) and the $2^1\Sigma_u^+$ state (right side). (bottom) Corresponding ratios of Na^+ and Na_2^+ as a function of the time delay between pump and dump pulses.[132,133,236] Reprinted with permission from ref 236. Copyright 1997 Wiley-VCH.

Figure 26.[236] Similarly, the variation of the delay time between the pulses was used by Herek, Materny, and Zewail[134] to switch between different channels for the photofragmentation of NaI, leading to the same product

$$NaI^* \rightarrow [Na\cdots I]^* \rightarrow Na(^2S_{1/2}) + I(^3P_{3/2}) \quad \text{and}$$

$$NaI^* \rightarrow [Na\cdots I]^* \xrightarrow{h\nu} [Na\cdots I]^{**} \rightarrow Na(^2S_{1/2}) + I(^3P_{3/2})$$

Encouraged by confirmation of the control concept, two-parameter control was considered in order to manipulate different processes in dimers and diatomic molecules. In addition to the pump−probe time delay, the second control parameter involved the pump[142,143] or probe[136,137] wavelength, the pump−dump delay,[139,144,145] the laser power,[191] the chirp,[138,146] or the temporal width[140] of the laser pulse. Optimal pump−dump control of K_2 has been carried out theoretically in order to maximize the population of certain vibrational levels of the ground electronic state using one excited state as an intermediate pathway.[141,250,272,424] The maximization of the ionization yield in mixed alkali dimers has been performed first experimentally using closed loop learning control[148,147,153] (CLL) and then theoretically in the framework of optimal control theory (OCT).[154]

Since optimized pulses obtained from OCT and CCL are available for NaK, it is instructive to present these results for two purposes. First, it is possible to show under which conditions the shaped pulses are reproducible. Second, the connection between the forms of the shaped pulses and different ionization pathways can be established. This allows determination of the mechanism for the maximization of the ionization yield under the participation of several excited states.

For this purpose, optimization of laser fields for controlling the photoionization in NaK will be outlined. This will be performed in the framework of optimal control theory[243] using full quantum me-

chanical treatment. This involves the combination of (i) electronic structure, (ii) dynamics, and (iii) optimal control considering (iv) experimental conditions.

(i) Accurate potential energy surfaces for the ground and excited states of NaK[425,426] as well as for the cationic ground state[154] are needed prerequisites for the consideration of the ionization process.[154] The calculations using the ab initio full CI method for the valence electrons and an effective core potential with core-polarization (ECP−CPP), together with suitable AO basis sets, are adequate for this purpose. Investigation of photoionization processes in the energy interval of 4.83 eV, corresponding to three photons of 1.61 eV used in experiments, involves the three excited states $2^1\Sigma^+$, $3^1\Pi$, and $6^1\Sigma^+$ of the neutral NaK, which are resonant with one- and two-photon energies, respectively.

(ii) Quantum dynamics simulations can be carried out by representing the wave function on a grid and using a nonperturbative approach based on a Chebychev polynomial expansion of the time evolution operator.[367] The interaction with the time-dependent electric field involves the ground state and three excited states of the neutral NaK as well as a manifold of cationic states. The treatment within the dipole approximation and the rotating wave approximation (RWA) is justified in the weak field regime. The rotational motion can be neglected because of the large atomic masses and short time scales involved.

The outlined procedure involves the following steps. The Hamiltonian $\hat{H}$ is given in the Born−Oppenheimer and dipole approximation

$$\hat{H}(t) = \hat{T} + \hat{V} - \hat{\mu}_{ge}\epsilon(t) \quad (62)$$

where $\hat{T}$ is the operator of the nuclear kinetic energy, $\hat{V}$ stands for the potential energy curves of the considered electronic states (both operators are diagonal), and $\hat{\mu}_{ge}$ is the transition dipole moment between the considered electronic states and is off diagonal.

In the rotating wave approximation, a cosine-like real electric field can be replaced by

$$\epsilon_{RWA}(t) = \frac{1}{2}A(t)e^{i\omega t} \quad (63)$$

The time propagation follows the principle of a successive application of the time evolution operator

$$|\Psi(t_0 + n\Delta t)\rangle = \prod_{j=0}^{n-1}\hat{U}(t_0 + (j+1)\Delta t, t_0 + j\Delta t)|\Psi(t_0)\rangle \quad (64)$$

with

$$\hat{U}(t + \Delta t, t) = e^{-i\hat{H}(t)\Delta t} \quad (65)$$

assuming that the Hamiltonian does not change significantly within time Δt and can be replaced by piecewise constant terms.

After a normalization of the eigenvalue spectrum of $\hat{H}$ to the range [−1, 1], the polynomial expansion of the normalized time evolution operator $e^{-i\hat{H}'\Delta t'}$ can be obtained by means of the Chebychev propagator

$$e^{-i\hat{H}'\Delta t'} \approx \sum_{n=0}^{N}(2 - \delta_{0,n})(-i)^n J_n(\Delta t')\, T_n(\hat{H}') \quad (66)$$

where T_n represents the n-th Chebychev polynom and $J_n(\Delta t')$ are Bessel functions of the first kind of order n. Since the Bessel function decreases exponentially if the order n becomes larger than the argument $\Delta t'$, an exponential convergence of the expansion coefficients of eq 66 can be achieved.

(iii) The objective of the optimal control is the maximization of the photoionization yield, and the target operator corresponds to the total occupation of the cationic states. For this purpose, eq 52 has to be used, in which the last term on the right-hand side can be modified by introducing the penalty factors which allow one to respect appropriate experimental conditions.[243] For the transition dipole moments between the excited electronic states of the neutral species and the ground state of the cation, different approximations can be introduced.[136−138,140,191,419] For example, the constant value of 5 D is in the range of transition dipole moments between electronic states of the neutral NaK and is sufficiently large to provide the robustness of the optimized pulses according to ref 427. The influence of the nuclear distance-dependent transition dipole moments should be tested. This is available, for example, for NaI[140] and was found to be negligible.

However, an explicit treatment of the electronic continuum for the cationic ground state is very important. It dramatically influences the optimization of the ionization process, and therefore, it is mandatory for the appropriate treatment. For this purpose, the electronic continuum can be discretized by introducing several replicas of the cationic ground state. For example, in the case of NaK, 14 replicas, with energy differences of 95 cm^{-1} in the range from 1075 to 2310 cm^{-1}, for the electron kinetic energies (eKEs) cover both the direct and the sequential photoionization from the outer turning points of the involved electronic states. For the optimization of the pulses, the Krotov algorithm[428] can be employed.

(iv) In the experiment, NaK dimers were produced in an adiabatic coexpansion of sodium−potassium vapor and argon carrier gas through a nozzle into the vacuum. To obtain mainly dimers, the oven temperature and the argon pressure have to be chosen appropriately (e.g. 650 °C and to 2 bar, respectively). To excite and ionize the neutral alkali dimers, the femtosecond laser beam was focused onto the molecular beam. The produced ions were mass selected and detected. The laser pulses were produced by a Ti:sapphire oscillator (Tsunami; Spectra Physics) with a repetition rate of 80 MHz, a central wavelength of 770 nm, a spectral width of 8.5 nm (fwhm), and a pulse intensity of about 1 GW/cm^2 in the interaction region. These data show that the experiments were carried out in the weak field regime. Such experimental conditions can be taken into account in the theoretical treatment, and the magnitude of the simulated laser field can be adjusted to the experimental values according to the method

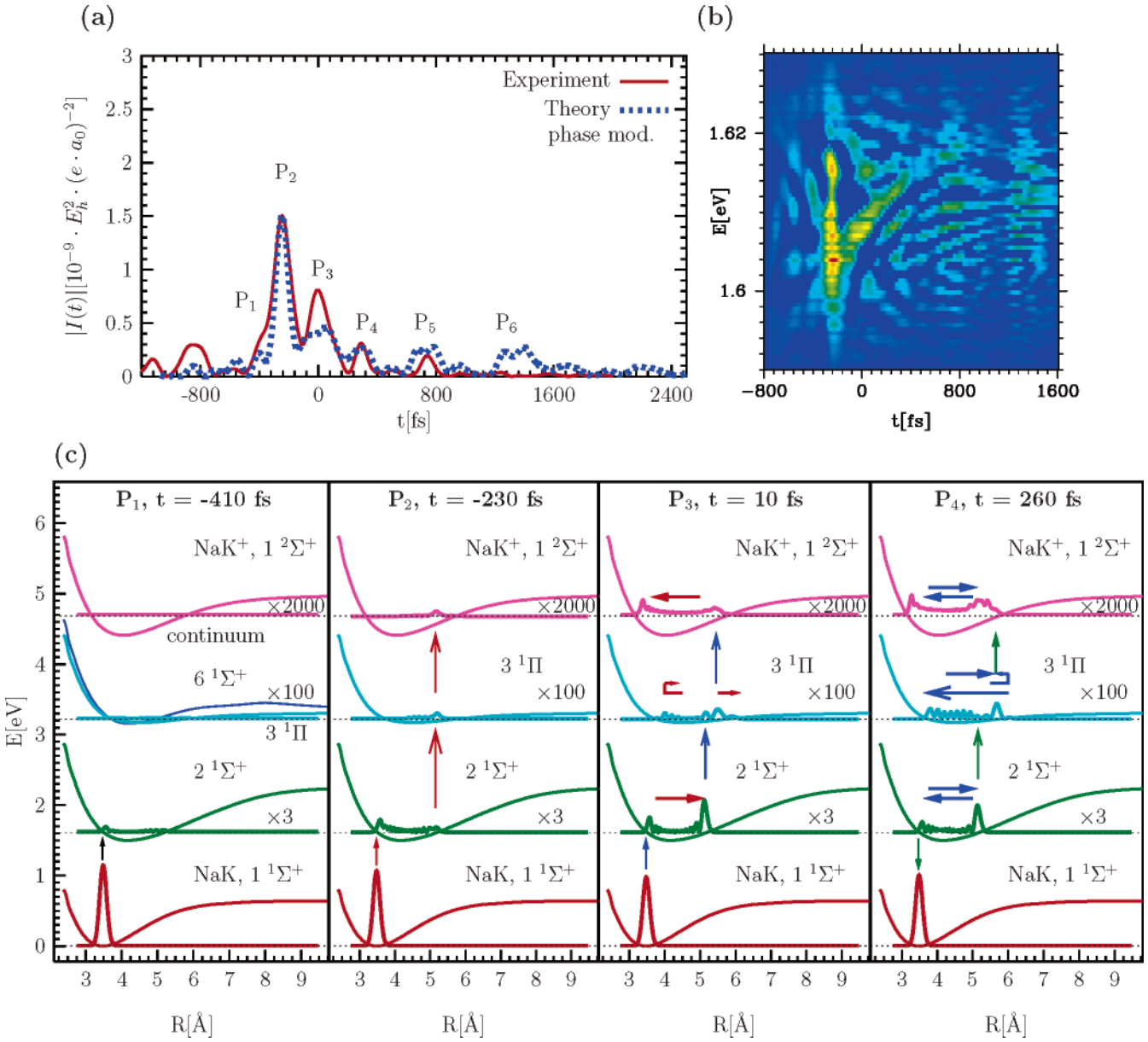

Figure 27. (a) Comparison of the theoretically (dotted line) optimized phase-modulated pulse (starting with the experimentally optimized pulse) with the experimentally (solid line) optimized pulse, using the CLL procedure; (b) Wigner–Ville distribution of the theoretically optimized pulse; (c) snapshots of the wave packet propagation corresponding to P_1 (−410 fs), P_2 (−230 fs), P_3 (10 fs), and P_4 (260 fs).[154]

given in ref 147. The experimental pulse shaper consists of a liquid crystal modulator mask with a resolution of 128 pixels located in the Fourier plane of a zero dispersion compressor. The experimentally optimized pulses were obtained by a nondeterministic evolutionary algorithm modulating only the phase. For further details on the experimental setup, see ref 147. It is important to know that the obtained ion yields stay almost constant for repeated optimization runs, whereas the optimized pulse shapes may slightly differ. The best pulse form under the given experimental conditions that has been mostly obtained in the performed optimizations is shown in Figure 27. The error of the optimization factor due to molecular beam fluctuation is estimated to be 5%. The temporal intensity of the acquired experimentally optimized pulse was obtained from the experimental cross-correlation signal and served as an initial guess for the theoretical optimization.

Theoretically optimized pulses in the framework of OCT,[154] obtained according to the procedure outlined in section 5.1 using experimentally optimized pulses as an initial guess, are shown in Figure 27. They are compared with the experimentally optimized pulse using the CLL technique described above, which provided an increase of the ion yield by 60% with respect to that generated by a transform limited pulse. The leading features of both phase modulated pulses obtained from OCT and CLL are in good agreement, as shown in Figure 27a. The snapshots of the wave packet propagation under the influence of the theoretically optimized pulse (Figure 27c) serve to assign the subpulses to underlying processes and to reveal the mechanism responsible for the population of the cationic state.

The role of the P_1 subpulse is to transfer a part of the population from the ground electronic state to the first excited $2^1\Sigma^+$ state. This creates a wave packet

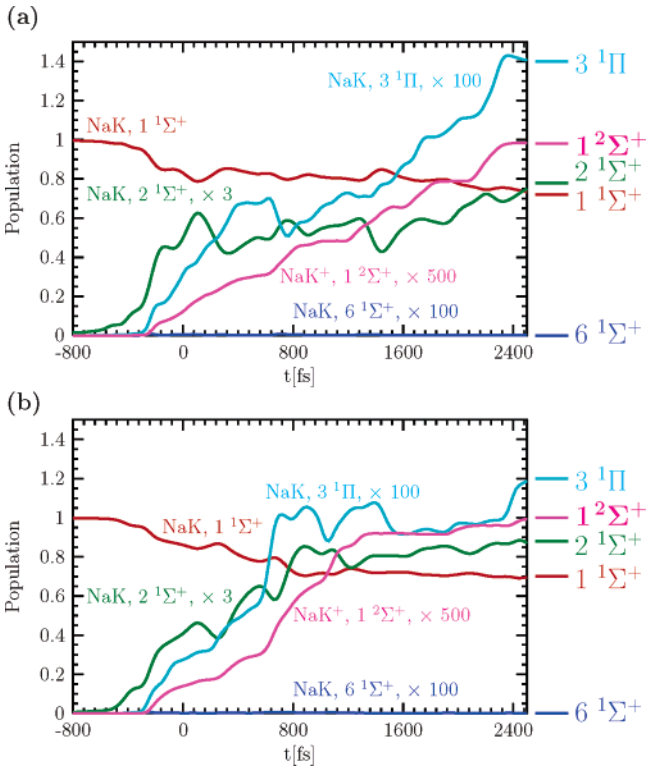

Figure 28. Time-dependent population of participating electronic states of the neutral and cationic NaK, obtained from simulations with an initial guess using (a) the experimentally optimized pulse[154] or (b) two Gaussian pulses.[154]

in the $2^1\Sigma^+$ state which propagates almost to the outer turning point within 180 fs. Subsequently, at the outer turning point, the dominant P_2 subpulse simultaneously transfers the population to the $3^1\Pi$ state by a one-photon process as well as to the cationic ground state by a resonant two-photon process, as can be seen in Figure 27c. In addition, the P_2 subpulse increases the population of the $2^1\Sigma^+$ state at the inner turning point. Subsequently, the P_3 subpulse brings the wave packet to the $3^1\Pi$ state after the outer turning point has been reached. In contrast to the dominant subpulse P_2, the P_3 subpulse also transfers population to the cationic state by the one-photon sequential processes, since the split part of the wave packet, before being transferred by P_2, propagates on the $3^1\Pi$ state as well. At later times, for example, at P_4, the superposition of the wave packets complicates the propagation by interference, as can be seen from the corresponding snapshot.

The separation of the early subpulses up to P_4 reflects the motion on the $2^1\Sigma^+$ state with a periodicity of ~440 fs (oscillation period in the $2^1\Sigma^+$ state), while after the P_4 subpulse the periodicity is disturbed by the influence of the $3^1\Pi$ state. The described steps leading to the desired population of the cationic state can also be identified from the analysis of the state populations displayed in Figure 28a. Notice that, besides excitation, dump processes also appear (see Figure 28a). Due to the increased population of the $2^1\Sigma^+$ and $3^1\Pi$ states, the dump processes appear at 200, 800, and 1360 fs from the $2^1\Sigma^+$ state to the ground state and at 700 fs from the $3^1\Pi$ state to the $2^1\Sigma^+$ state. Consequently, a staircaselike behavior in the populations of these states is present. Moreover, the later subpulses cause a substantial increase in the population of the cationic states, showing the important contributions of the later subpulses with low intensities.

On the basis of the above analysis of the underlying dynamics driven by the optimized pulse, the following mechanism for the optimal ionization process of NaK can be proposed. It involves an electronic transition followed by a direct two-photon ionization from the outer turning point of the $2^1\Sigma^+$ state. This behavior supports the proposed explanation of the experimental optimal pulse shape given in experimental publications.[151,152] However, according to the analysis of the theoretically optimized pulses described above, the sequential one-photon ionization process mediated by the $3^1\Pi$ state takes over the important role at later times.

Additional insight into the energetic and temporal structure of the optimal pulse can be gained from the Wigner−Ville representation shown in Figure 27b. The dominant feature is the increase of the photon energy with time. This up-chirp in the energy regime of 1.59−1.63 eV can be qualitatively explained by an overlap between the propagating wave packet on the $3^1\Pi$ state and the successively higher lying vibronic levels of the cationic state. For an identification of the quantitative features, amplitude and phase modulations would be more adequate. However, the X-FROG trace obtained from the experimental result[152] also shows a pronounced up-chirp, in full agreement with the features displayed in Figure 27b. Moreover, the up-chirp was found to enhance the NaK ion signal according to recent chirp-dependent experiments.[150]

To verify the robustness of theoretically optimized pulses, the results obtained using two Gaussian pulses separated by 660 fs, as an initial guess, are compared with experimental results in Figure 29. The experimental pulse is again roughly reproduced, and the leading features of the theoretical pulse remain unchanged with respect to those obtained by an experimentally optimized pulse as an initial guess (cf. Figure 27). The main differences between the optimized pulses obtained with distinct initial guesses concern the relative intensities of the weaker subpulses, which lead only to very small relative changes in the time-dependent populations (cf. Figure 28b). The Wigner−Ville representations of both theoretically optimized pulses are almost identical, verifying the robustness of the derived pulses and therefore the validity of the proposed mechanism. These findings were obtained only if the continuum of the cationic state was taken into account as described above.

In summary, the agreement between experimentally and theoretically optimized pulses, which is independent of the initial guess, shows that the shapes of the pulses can be used to deduce the mechanism of the processes underlying the optimal control. In the case of optimization of the ionization process in NaK, this involves a direct two-photon resonant process followed by sequential one-photon processes at later times. These findings obtained on the simple system are promising for using the shapes

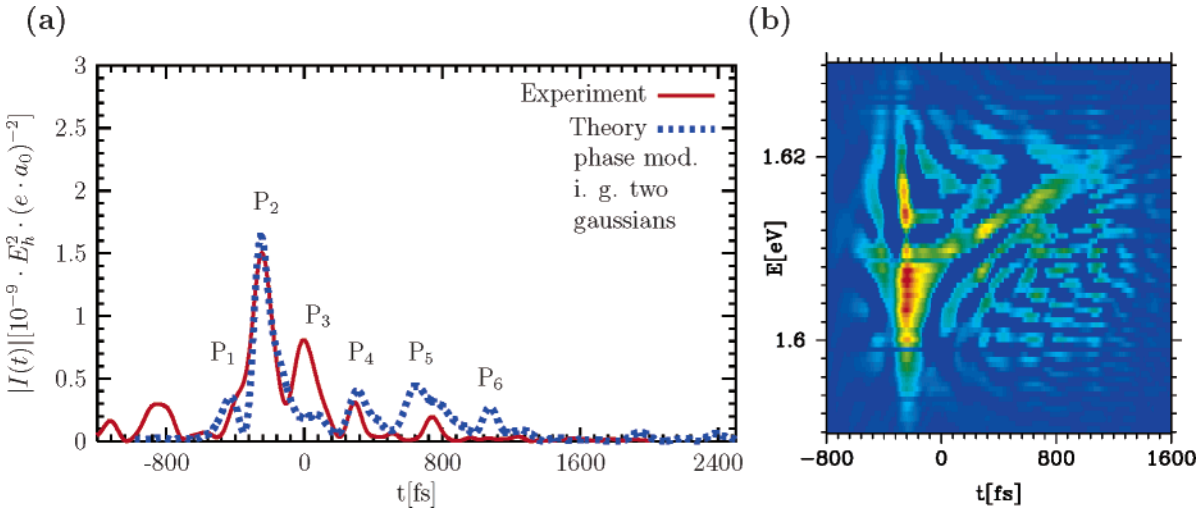

Figure 29. (a) Comparison of the theoretically (dotted line) optimized phase-modulated pulse (starting with two Gaussian pulses) with the experimentally (solid line) optimized pulse, using the CLL procedure; (b) Wigner−Ville distribution of the theoretically optimized pulse.[154]

of tailored pulses to reveal the nature of processes involved in the optimal control of more complex systems. This will be addressed in the next section.

As already mentioned in section 4.4, the electronic structure of excited states of alkali trimers is very complex due to conical intersections and avoided crossings. Consequently, the description of nuclear dynamics is very demanding. In this context, quantum optimal control of the photodissociation of Li_2-Na from the stable acute geometry to the near-degenerate obtuse triangular geometry over the excited state has been carried out based on two-dimensional energy surfaces.[424,429] The analysis of the optimized pulse revealed a fundamental pump−dump cycle. A similar study was performed for the collision pair Na + H_2 with the aim of forming a localized wave packet near the conical intersection of the ground state (Na(3S) + H_2) and the excited state (Na(3P) + H_2). Stepwise excitation of the collision pair at different intersection distances is reflected in optimized pulses.[430]

Experimentally, the control of the population of differently bound electronic states of Na_3 was achieved by linearly chirped fs-laser pulses of low intensity.[149] In the case of unchirped or slightly downchirped excitation pulses (with ~300 fs duration), the wave packet propagation takes place in the B state, and the symmetric stretching mode can be identified in the pump−probe spectrum.[149] In the case of the 400 fs downchirped pulse, the leading blue spectral component creates a wave packet in the B state, which is dumped by the red spectral tail into the vibrational excited state of the electronic ground state. Additionally, the symmetric stretching mode is reflected in the pump−probe spectrum. This finding confirms also the Tannor−Kosloff−Rice scheme.[126,127,239,243]

In addition to the control of the molecular dynamics in bound electronic states of Na_3, control of the photofragmentating heteronuclear trimer Na_2K was also experimentally achieved.[147−150] Manipulation of different branching ionization and fragmentation pathways of the photoexcited Na_2K was successfully performed in the framework of the CLL optimal control scheme for the multiphoton process.[147−150] The optimal laser field controls the yield of the resulting parent and fragment ions. The pulse structure is extremely rich and should contain information about underlying processes. The intensity of the subpulses correlates with the number of photons involved in the process, and the temporal structure of the pulses should be connected with the vibronic properties of the molecule or the fragment. To use the shape of the pulse for identification of underlying processes, it would be necessary to optimize the pulses theoretically and to compare them with experimentally optimized pulses. This would extend the use of the control as a tool for analysis of processes in small systems but with complex electronic structures.

5.3. Complex Systems: Optimal Control and Analysis of Processes by Control

It is still a central issue if and under which conditions optimal control involving more than one electronic state can be achieved for systems with increasing complexity. For these systems, energy landscapes of the ground and excited states can substantially differ from each other. Therefore, the first issue to be addressed concerns the existence of a connective pathway between the initial state and the objective which is reached via a different electronic state. In addition, even if the connective pathway is ensured, the optimal path must be found. Moreover, the method used for nuclear dynamics and the tailored pulses should involve a realistic computational demand. Therefore, new strategies for optimal control are needed. An attractive possibility is based on the concept of the intermediate target[121,431] in the excited state, which is defined as a localized ensemble (wave packet) corresponding to the maximum overlap between the forward propagating ensemble on the electronic excited state (starting from the initial state) and the backward propagated ensemble from the objective in the ground state at optimal time delay between both pulses.

In the case that separation of active from passive degrees of freedom cannot be made for complex systems and therefore a large number of them have to be treated explicitly, the classical nuclear dynamics is the only realistic approach. Quantum corrections can also be introduced under the given circumstances. Moreover, the classical MD "on the fly" can be extremely useful for realization of new strategies for optimal control, such as construction of the intermediate target, as will be shown below. The role of the intermediate target is to guarantee the connective pathway between the initial state and the objective and to use the localized ensemble in the excited state to select the appropriate parts of both energy surfaces involved. This is directly related to the inversion problem.[187,256−259] In the case of the pump−dump control for two-phase unlocked ultrafast fields in the weak response regime, the intermediate target serves first to optimize the pump pulse. Therefore, it is possible to decouple optimization of the pump and the dump pulses, which is very advantageous from the computational point of view. An appropriate tool for realization of the strategy for optimal control of complex systems based on the concept of the intermediate target is the density matrix formulation of the OCT. It combines the Wigner−Moyal representation of the vibronic density matrix with ab initio molecular dynamics (MD) "on the fly" in the electronic excited states and the ground states without precalculation of both energy surfaces. This method, labeled as the ab initio Wigner distribution approach, was outlined in section 3.2. It is applicable to complex systems provided that the adequate quantum chemical procedures can be used for dynamics in excited states. Moreover, due to available analysis based on MD, the shapes of the optimized pulses can be directly connected with underlying ultrashort processes. After the outline of the theoretical basis for this optimal control strategy, the concept of the intermediate target will be applied to optimize the pump and dump pulses for driving the isomerization process in the nonstoichiometric Na_3F_2 cluster, avoiding conical intersection between the ground state and the first excited state and maximizing the yield in the second isomer.

Intermediate Target as a New Strategy for Optimal Control in Complex Systems. The optimal control strategy described here aims to optimize the temporal shapes of phase-unlocked pulses (pump and dump) and the time delay between them, t_d. These tailored fields should be capable of driving the system, starting from the lowest energy isomer over the first excited state, to the second isomer (objective) at the time delay t_d with maximal yield for systems with an arbitrary number of degrees of freedom.

The form of the pump and dump pulses in the optimal phase-unlocked pump−dump control is $\epsilon_{P(D)}(t) = E_{P(D)}(t)\ \exp(-i\omega_{eg}t) + E^*_{P(D)}(t)\ \exp(i\omega_{eg}t)$, where $E_{P(D)}$ is a slowly varying envelope of the fields, and ω_{eg} is the energy difference between the minima of the excited and the ground states. The objective in the ground state is described in the Wigner representation by an operator $\hat{A} = A(\Gamma)|g\rangle\langle g|$. $A(\Gamma)$ is the Wigner transform of the objective in the phase space $\Gamma = \{q_i, p_i\}$ of coordinates and momenta, and $|g\rangle\langle g|$ is the ground-state projection operator. $A(\Gamma)$ can be defined, for example, as

$$A(p,q) = \prod_{i=1}^{N} \frac{1}{\sqrt{2\pi}\Delta q_i} e^{-(q_i-\bar{q}_i)^2/2(\Delta q_i)^2} \Theta\left(E_{\min} - \sum_{i=1}^{N} \frac{p_i^2}{2m_i}\right) \quad (67)$$

where $\bar{q}_i$ labels Cartesian coordinates of the second isomer and Δq_i are deviations. The role of the function Θ is to ensure that the kinetic energy is below the lowest isomerization barrier E_{min}. This corresponds to the spatial localization of the phase space density and arbitrary distribution of momenta. The optimized pulses can be obtained from the functional

$$J(t_f) = A(t_f) - \lambda_P \int_0^{t_f} |E_P(t)|^2\, dt, \quad -\lambda_D \int_0^{t_f} |E_D(t)|^2\, dt \quad (68)$$

where $A(t_f)$ is the yield at time t_f, which can be calculated for weak fields in second-order perturbation theory.[260,268,432] It involves the propagated excited- and ground-state ensembles induced by the pump and dump pulses, the time-dependent energy gaps between the two states, and the initial distribution of the phase space in the Wigner representation. Optimal field envelopes can be obtained by calculating the extrema from the control functional (eq 68) by performing the variation procedure.[260−263,265−269,423,432−434] This leads to the pair of coupled integral equations for the field envelopes:

$$\int_0^{t_f} d\tau'\, M_P(\tau,\tau';E_D)\, E_P(\tau') = \lambda_P E_P(\tau) \quad (69)$$

$$\int_0^{t_f} d\tau'\, M_D(\tau,\tau';E_P)\, E_D(\tau') = \lambda_D E_D(\tau) \quad (70)$$

The integral kernels corresponding to material response functions are given by

$$M_P(\tau,\tau';E_D) = \int\int d^2\,\Gamma_0 \int_0^{t_f} d\tau'' \int_0^{\tau''} d\tau'''\, A(\Gamma_g(t_f-\tau''; \Gamma_e(\tau'''-\tau;\Gamma_0)))e^{i(\omega_{eg}-U_{eg}(\Gamma_e(\tau'''-\tau;\Gamma_0)))(\tau''-\tau''')} \times e^{i(\omega_{eg}-U_{eg}(\Gamma_0))(\tau-\tau')}\rho_{gg}(\Gamma_0)\, E_D(\tau''')\, E_D{}^*(\tau'') \quad \tau \geq \tau' \quad (71)$$

$$M_D(\tau,\tau';E_P) = \int\int d^2\,\Gamma_0 \int_0^{\tau'} d\tau'' \int_0^{\tau''} d\tau'''\, A(\Gamma_g(t_f-\tau; \Gamma_e(\tau'-\tau'';\Gamma_0)))e^{i(\omega_{eg}-U_{eg}(\Gamma_e(\tau'-\tau'';\Gamma_0)))(\tau-\tau')} \times e^{i(\omega_{eg}-U_{eg}(\Gamma_0))(\tau''-\tau''')}\rho_{gg}(\Gamma_0)\, E_P(\tau''')\, E_P^*(\tau'') \quad \tau \geq \tau' \quad (72)$$

Γ_e and Γ_g correspond to propagated excited- and ground-state ensembles, and U_{eg} is the time-dependent energy gap between the excited state and the ground state. Both equations depend on the pump and dump pulses, and therefore, they are coupled integral equations which can, in principle, be solved iteratively, yielding optimized pump and dump pulses. This is computationally unrealistic even for systems of moderate complexity because the coupled classical simulations on the ground and excited states have

to be performed. The calculation of objective A in eqs 71 and 72 requires the propagation of the ensemble on the ground state Γ_g, starting at different initial conditions. These conditions are obtained from the propagated ensemble Γ_e of the excited state at each time step. Therefore, the strategy involves decoupling of eqs 71 and 72, which is possible only in the short pulse regime on the femtosecond time scale and is outlined below.

(i) In the zeroth-order approximation of an iterative procedure and in the ultrafast regime, it is justified to calculate the kernel functions M_P and M_D with strongly localized pulse envelopes $E_P \approx \delta(t)$ and $E_D \approx \delta(t - t_d)$. Then, the zeroth-order material response functions take the following forms:

$$M_P^{(0)}(\tau,\tau') = \int\int \mathrm{d}^2\,\Gamma_0 A(\Gamma_g(t_f-t_d;\Gamma_e(t_d-\tau;\Gamma_0))) \times \mathrm{e}^{i(\omega_{eg}-U_{eg}(\Gamma_0))(\tau-\tau')}\rho_{gg}(\Gamma_0) \qquad \tau \geq \tau' \quad (73)$$

$$M_D^{(0)}(\tau,\tau') = \int\int \mathrm{d}^2\Gamma_0\, A(\Gamma_g(t_f-\tau;\Gamma_e(\tau';\Gamma_0))) \times \mathrm{e}^{i(\omega_{eg}-U_{eg}(\Gamma_e(\tau';\Gamma_0)))(\tau-\tau')}\rho_{gg}(\Gamma_0) \qquad \tau \geq \tau' \quad (74)$$

The pump and dump pulses are decoupled. Consequently, the pump pulse optimization involves the propagation on the excited state $\Gamma_e(t_d-\tau;\Gamma_0)$ from $\tau = 0$ until $\tau = t_d$, starting with Γ_0 (initial ensemble; eq 73). For the dump optimization, according to eq 74, the dynamics on the ground state $\Gamma_g(t_f-\tau;\Gamma_e(t_d))$ has to be carried out for $\tau' = t_d$ until t_f with the initial conditions given by the ensemble of the excited state $\Gamma_e(t_d)$ at t_d, which corresponds to the intermediate target. $\Gamma_e(t_d)$ at t_d can be determined from the maximal overlap between a forward propagated ensemble from the first isomer on the excited state and a backward propagated ensemble on the ground state from the second isomer.

(ii) Equations 69 and 73 yield an optimal pump pulse which localizes phase space density at the intermediate target.

(iii) The optimized dump pulse projects the intermediate target to the ground state and optimally localizes the phase space density into the objective (second isomer) at a final time t_f. This means that the connective pathway between the initial state and the objective is guaranteed by the intermediate target at a time t_d. For this purpose, the function $A(\Gamma_g(t_f-t_d);\Gamma_e(t_d))$ must have nonvanishing contributions, as follows from eqs 73 and 74. This procedure can be continued iteratively, but it is most likely that the zeroth- and first-order iterations lead to sufficient accuracy. The concept of the intermediate target represents a new strategy which ensures that the objective with maximal yield can be reached by optimizing pump and dump pulses independently. This allows the application of the optimal pump−dump control to complex systems and ensures controllability, provided that the intermediate target can be found, which is illustrated below.

Optimal Control of Photoisomerization in Na_3F_2. The isomerization in Na_3F_2 through conical intersection between the first excited state and the ground state, as discussed in section 4.3, provides a system with a high internal energy (~0.65 eV) which populates both isomers and does not allow population of the second isomer only through this process.[116] Therefore, the described optimal control strategy based on the intermediate target concept serves as an adequate tool to find the optimal pathway, allowing one to populate isomer II with maximal yield and suppressing the pathway through the conical intersection.[121]

For this purpose, the initial ensemble of isomer I has to be generated. Then the intermediate target involving excited- and ground-state dynamics has to be determined. Finally, the pump and dump pulses have to be optimized. For the initial ensemble, a 50 K, canonical ensemble in the ground state of isomer I in the Wigner representation can be constructed using, for example, a set of ~1000 coordinates and momenta. In the pump step (1.33 eV), the ensemble can first be propagated on the excited state (for example, 300 fs). To determine the intermediate target and the optimal time delay t_d, the ensemble has to be dumped to the ground state (in steps of, e.g., 25 fs) and subsequently propagated (for, e.g., 1 ps). It can be shown that isomer II is reached by the ensemble at $t_d = 250$ fs and the residence time of at least 500 fs can be achieved. The ensemble averaged geometry which determines the coordinates of the intermediate target is shown in Figures 30 and 31. Notice that the "geometry" of the intermediate target is closely related to that of the transition state separating two isomers on the ground state. In this case, the role of the intermediate target ensuring the connective pathway from the initial state and the objective over the excited state is evidenced by its relation to the transition state. The averaged kinetic energy in the intermediate target corresponds to ~75% of the isomerization barrier in the ground state. This guarantees that, after the dump, the ensemble will remain localized in the basin of isomer II.

The optimization of the pump pulse leads to a localization of the phase space density around the intermediate target. For the intermediate target operator in the Wigner representation (eq 73), a minimum uncertainty wave packet can be assumed:

$$A(p_i,q_i) = \prod_{i=1}^{3N=15} \frac{1}{2\pi\Delta p_i \Delta q_i} \mathrm{e}^{-(q_i-\bar{q}_i)^2/2(\Delta q_i)^2} \mathrm{e}^{-(p_i-p_i)^2/2(\Delta p_i)^2} \quad (75)$$

The material response function $M(\tau,\tau')$ for the pump pulse (eq 73) can be calculated, for example, on a time grid of 1 fs and can be symmetrized and diagonalized according to eq 69. In this case, the largest eigenvalue was obtained to be 0.82, corresponding to the globally optimized pulse, which has 82% efficiency to localize the ensemble in the intermediate target.

The shape of the optimized pump pulse, shown in Figure 30, is characterized by two portions corresponding to ~70 and ~10 fs. Fourier and Wigner−Ville transforms of the pump pulse, shown also in Figure 30, provide physical insight. Comparison of the Fourier transform with the Franck−Condon profile of isomer I shows that the excitation of the

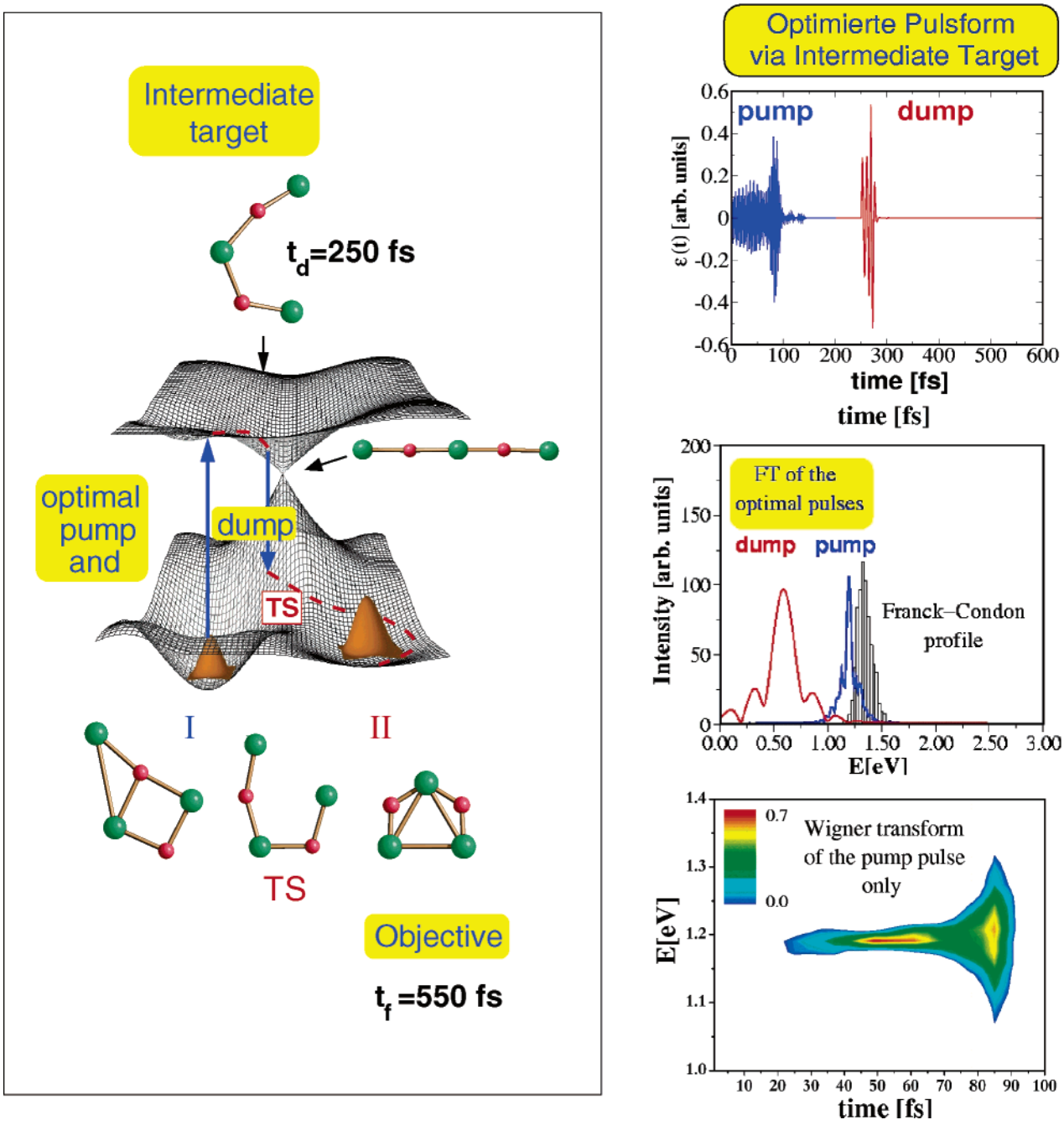

Figure 30. Scheme for pump−dump optimal control in the Na_3F_2 cluster with geometries of the two ground-state isomers and of the transition state separating them, the conical intersection, and the intermediate target (left side). The optimal electric field corresponding to the pump and dump pulses[121] (upper panel, right side). The mean energy of the pump pulse is 1.20 eV, and the mean energy of the dump pulse is 0.6 eV. Fourier transforms of the optimal pump and dump pulses and the Franck−Condon profile for the first excited state corresponding to the excitation energy T_e = 1.33 eV (middle panel, right side). Wigner transform of the optimal pump pulse (bottom panel, right side).

low lying vibrational modes at ∼1.2 eV of the initial ensemble is dominantly responsible for reaching the intermediate target. This spectral region corresponds to lower lying vibrational modes which open the C_s structure of isomer I by breaking the Na−Na bonds and one of Na−F bonds. The Wigner−Ville transform shows that this energetically sharp transition corresponds to the first temporal portion of ∼70 fs of the pump pulse. In contrast, a very short second portion after 80−90 fs of ∼10 fs is energetically much wider. It is related to the tails of the Fourier transform, which are symmetric with respect to the 1.2 eV transition, reflecting equally distributed velocities in the initial ensemble.

The dump pulse optimization leads to a spatial localization of the phase space density in the objective (isomer II). For this purpose, the intermediate target operator (eq 75) can be propagated on the ground

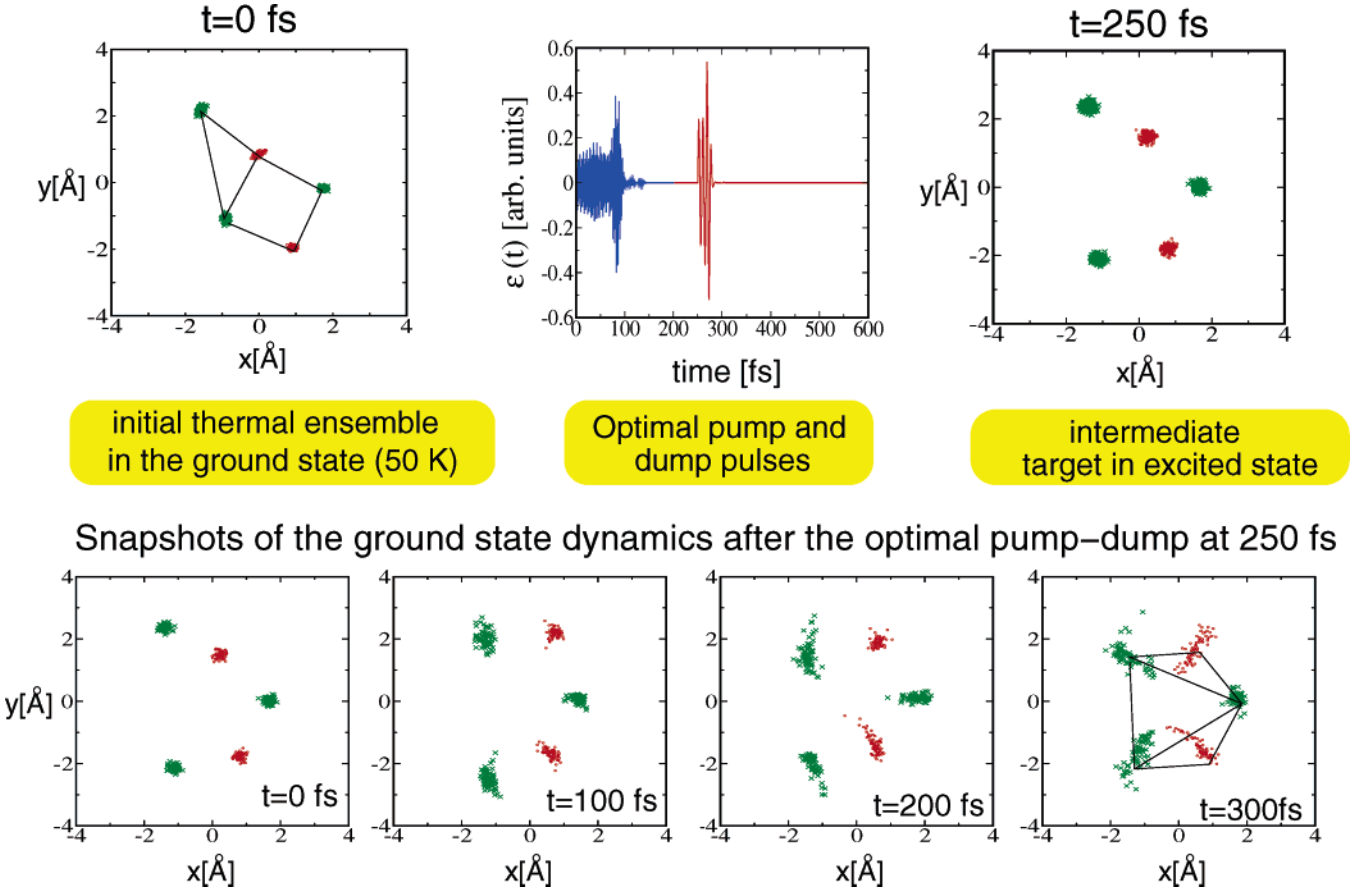

Figure 31. Initial thermal ensemble, optimal pump and dump pulses, intermediate target (upper panels). Snapshots of the dynamics obtained by propagating the ensemble corresponding to the intermediate target after the optimized pump–dump at 250 fs on the ground state showing the localization of the phase space density in the basin corresponding to isomer II[121] (lower panels).

state, and the dump pulse is obtained from eqs 70 and 74. The largest eigenvalue, for example, of 0.78, can be obtained. This corresponds to 78% efficiency of localization of isomer II. The optimized dump pulse is very short (~20 fs; cf. the part of the signal after t_d = 250 fs in Figure 30). This means that the time window around t_d for depopulation of the excited state is very short. Otherwise, the system would gain a large amount of energy in the excited state (leading to a conical intersection). The Fourier transform of the dump pulse is centered around 0.6 eV, corresponding to the Franck–Condon transition at t_d. Finally, to illustrate the efficiency of optimized pulses, snapshots of the ground state ensemble propagated after the dump process are shown in Figure 31. It can clearly be seen that the phase space density is localized in isomer II (objective) after t_d + 200 fs = 450 fs.

Using the strategy for optimal pump–dump control based on the intermediate target, it is possible to show that optimized pulses drive the isomerization process in the desired objective (isomer II), suppressing the pathway through the conical intersection. This means that the complex systems are controllable, provided that the intermediate target exists. The analysis of the MD and of the tailored pulses allows identification of the mechanism responsible for the selection of appropriate vibronic modes necessary for the optimal control.

In summary, optimal control of fs-processes, involving two electronic states, driven by tailored pump and probe or dump pulses requires identification of the connective pathway between the initial state and the objective and finding the optimal pathway. This is possible if the intermediate target in the excited state can be found, which selects the appropriate parts of energy surfaces to ensure both requirements mentioned above. This was illustrated for the example of Na_3F_2, for which the optimal pump and dump pulses populate the objective (isomer II) with maximal yield, taking the optimal pathway and avoiding the conical intersection. The identification of the mechanism responsible for the shape of the pulses serves as a guide toward understanding the experimentally obtained tailored fields which still represents a challenging task for future work. In this way, the control is used not only to achieve the desired yield but also to identify and to analyze the underlying ultrafast processes responsible for favoring one pathway and for suppressing the others. Control as a tool for analysis complements the CLL technique and sheds light on the black box.

6. Summary and Outlook

Analysis and control of ultrafast processes in atomic clusters in the size regime in which "each atom counts" are of particular importance from a conceptual point of view and for opening new per-

spectives for many applications in the future. Simultaneously, this research area challenges the development of theoretical and computational methods from different directions, including quantum chemistry, molecular dynamics, and optimal control theory, removing borders among them. Moreover, it provides stimulation for new experiments.

By changing cluster size, and therefore structural and optical properties, different ultrafast processes can be monitored, and their time scales can be determined. They include bond breaking, geometric relaxation of different natures, IVR, isomerization, and reaction channels. These processes can be identified by analyzing adiabatic or nonadiabatic dynamics and simulated fs-signals. Therefore, the conditions under which the identified processes are experimentally observed can be precisely determined. This predictive power of theory can be directly used for conceptual planning of experiments, as illustrated in several examples in this review. Moreover, the tailored fields obtained in the framework of optimal control theory can drive selected processes, such as direct versus sequential ionization, isomerization toward one of the isomers, or the chosen reaction channel for which particular bond breaking or new bonding rearrangements promote the emanation of the reaction products.

Theoretical methods which combine ab initio MD "on the fly" with the Wigner distribution approach, which is based on classical treatment of nuclei and on quantum chemical treatment of electronic structure, represent an important theoretical tool for analysis and control of ultrashort processes in complex systems. Moreover, the possibility to include, in principle, quantum effects for nuclei by introducing corrections makes this approach attractive for further developments. However, for this purpose, new proposals for improving the efficient inclusion of quantum effects for nuclei and fast but accurate calculations of MD "on the fly" in the electronic excited states are mandatory. Both aspects represent attractive and important theoretical research areas for the future.

The strategies based on localization of the wave packet or ensemble (e.g., an intermediate target), ensuring the connective pathway between the initial state and the target in complex systems involving at least two different electronic states, are attractive for the following reasons. They allow simplification of optimization of pump and dump pulses for complex systems. They also permit selection of important parts of energy surfaces, which makes the inversion problem accessible. Finally, the analysis of the underlying dynamics makes it possible to assign the shapes of optimized pulses to processes, allowing one to unravel the mechanisms responsible for optimal control. This also allows the use of optimal control schemes as analysis tools for complex systems, which is an important conceptual issue with a promising perspective for applications in biomolecules, clusters, or even their complexes.

Due to the structure−reactivity relationships of clusters, the reactive centers can be identified. Furthermore, their size selectivity can be exploited for invoking reactions toward organic and inorganic molecules or for finding the cooperative effects needed for promoting these reactions. This research direction opens new roads for using tailored laser fields to drive the laser induced selective chemical reactions involving clusters. It also takes advantage of their functional properties, which might invoke a large impact in different application areas.

7. Acknowledgment

We thank our co-workers Drs. M. Hartmann, J. Pittner, B. Schäfer-Bung, and D. Reichardt, who have substantially contributed to the work included in this review. The fruitful cooperation with our experimental collegues Prof. L. Wöste, Dr. S. Vajda, and Dr. T. M. Bernhardt is highly appreciated. We extend our thanks to our theoretical collegues, Prof. J. Jortner, Dr. A. Heidenreich, Prof. P. Fantucci, Prof. C. Meier, Dr. M.-C. Heitz, and Prof. F. Spiegelman. Finally, we thank Mrs. Michele Kimble for correcting the manuscript. This work has been supported by Deutsche Forschungsgemeinschaft (DFG) SFB 450 "Analysis and control of ultrafast photoinduced reactions". R.M. acknowledges the financial support by the DAAD.

8. Appendix A: Analytic Derivatives for Excited States and Adiabatic Molecular Dynamics in the "Frozen Ionic Bonds" Approximation

For nonstoichiometric sodium fluoride clusters with a single excess electron (Na_nF_{n-1}), the "frozen ionic bond" approximation for $n - 1$ electrons involved in ionic bonding allows one to describe the ground state of the system at the restricted open shell Hartree−Fock (ROHF) level, yielding canonical MOs φ_i. The excited states are obtained as eigenstates of an effective one-excess-electron Hamiltonian $\hat{h}'$ containing Coulomb and exchange operators with the core. The corresponding matrix elements h'_{ij} in the MO basis φ_i form a submatrix of the Fock matrix and can be obtained straightforwardly, modifying the standard self-consistent field (SCF) program in such a way that after the convergence of the neutral restricted open shell Hartree−Fock (ROHF) SCF procedure has been achieved, one additional closed shell SCF iteration can be performed, yielding the closed shell Fock matrix. In analogy, the code for the Fock matrix derivative can be modified to compute derivatives of the $\mathbf{h}'$ matrix elements.

The wave functions ψ_i of the individual states of the one excess electron are then obtained as eigenfunctions of $\hat{h}'$ and can be expressed as

$$\psi_i = \sum_{j=o}^{M} D_{ji}\varphi_j \quad (i = o, ..., M) \tag{76}$$

where o labels the open shell singly occupied HOMO, and $\mathbf{D}$ is an unitary matrix which diagonalizes $\mathbf{h}'$

$$\mathbf{h}'\mathbf{D} = \mathbf{D}\mathbf{E}, \quad \mathbf{E} \equiv \mathrm{diag}(\epsilon_i) \tag{77}$$

The eigenvalues ϵ_i are the energies of the one excess electron, and their differences correspond to transition energies. Therefore, the total energy of an excited

state has the following form:

$$E_i = E_{\mathrm{SCF}} + \epsilon_i - \epsilon_{\mathrm{o}} \tag{78}$$

where ϵ_{o} is the ground-state energy of the one excess electron. Note that although the energy difference $\epsilon_i - \epsilon_{\mathrm{o}}$ might resemble use of the simple Koopmans theorem, the energy levels of the excess electron ϵ_i are (with the exception of ϵ_{o}) not equal to the SCF MO energy levels. They correspond to the solution of the excited states of the one excess electron, which feels the constant field of the remaining electrons, being "frozen" in the ground state.

The eigenvectors D_{ji} are used to obtain the transition density matrix $\gamma_{h,l}(jk)$ between the h-th and the l-th states

$$\gamma_{h,l}(j,k) = D^*_{jh} D_{kl} \tag{79}$$

from which transition moments and, subsequently, the oscillator strengths are computed. The total computational cost for the calculation of the absorption spectrum involving the transition energies and oscillator strengths amounts to the ROHF calculation, the single closed shell iteration, and a few matrix multiplications needed for the calculation of transition moments. An excellent agreement between the spectra of Na_2F and Na_4F_3 obtained from the MRCI[100] method, correlating all electrons, and those obtained from the "frozen ionic bond" approximation confirms the accuracy of the latter.

For the calculation of the gradient of the total energy given by eq 78, in addition to the gradient of the ROHF SCF energy, the derivatives of the excess electron energies $\nabla_{\mathbf{R}}\epsilon_i$ are needed. Using the definition of the orbital energies ϵ_i

$$\epsilon_i = \langle \psi_i | h' | \psi_i \rangle \tag{80}$$

$$= \sum_{j,k} (D^\dagger)_{ij} h'_{ij} D_{ki} \tag{81}$$

one obtains

$$\nabla_{\mathbf{R}}\epsilon_i = \sum_{jk} [(\nabla_{\mathbf{R}} D^\dagger)_{ij} h'_{jk} D_{ki} + (D^\dagger)_{ij} h'_{jk} \nabla_{\mathbf{R}} D_{ki} + (D^\dagger)_{ij} (\nabla_{\mathbf{R}} h'_{jk}) D_{ki}] \tag{82}$$

$$= \sum_j \epsilon_i [(\nabla_R D^\dagger)_{ij} D_{ji} + (D^\dagger)_{ij} \nabla_R D_{ji}] + \sum_{jk} (D^\dagger)_{ij} (\nabla_{\mathbf{R}} h'_{jk}) D_{ki} \tag{83}$$

Since the term in square brackets corresponds to a derivative of the normalization condition

$$\sum_{jk} (D^\dagger)_{ij} D_{jk} = \delta_{ik} \tag{84}$$

it remains only the second term

$$\nabla_{\mathbf{R}}\epsilon_i = \sum_{jk} (D^\dagger)_{ij} (\nabla_{\boldsymbol{R}} h'_{jk}) D_{ki} \tag{85}$$

which requires the calculation of derivatives of the effective one-excess-electron Hamiltonian $\nabla_{\mathbf{R}} h'_{jk}$. They are identical to the derivatives of the closed shell Fock matrix $\mathbf{F}$ obtained from the cation $Na_nF_{n-1}^+$ with the converged orbitals of the neutral system Na_nF_{n-1}. The gradient

$$\nabla_{\mathbf{R}} h'_{ij} = \nabla_{\mathbf{R}} h_{ij} + \sum_c [2\nabla_{\mathbf{R}}(ij|cc) - \nabla_{\mathbf{R}}(ic|cj)] \tag{86}$$

with one-electron (h_{ij}) and two-electron integrals in the MO basis is therefore reduced to known expressions.

$$\nabla_{\mathbf{R}} h'_{ij} = h'^{\mathbf{R}}_{ij} + \sum_k (U^{\mathbf{R}}_{ki} h'_{kj} + U^{\mathbf{R}}_{kj} h'_{ik}) + \sum_k \sum_l U^{\mathbf{R}}_{kl} A_{ij,kl} \tag{87}$$

$$h'^{\mathbf{R}}_{ij} = h^{\mathbf{R}}_{ij} + \sum_k \{2(ij|kk)^{\mathbf{R}} - (ik|jk)^{\mathbf{R}}\} \tag{88}$$

$$A_{ij,kl} = 4(ij|kl) - (ik|jl) - (il|jk) \tag{89}$$

In the above equations, the summations over k, l indices run from 1 to M, while i,j indices are confined to o, ..., M. The quantities $U^{\mathbf{R}}_{kl}$ in eq 87 describe the influence of geometry changes on the SCF eigenvectors $C_{\alpha i}$, which are defined as

$$\nabla_{\mathbf{R}} C_{\alpha i} = \sum_{j=1}^{M} C_{\alpha j} U^{\mathbf{R}}_{ji} \tag{90}$$

and are obtained as solutions of the extended general restricted open shell coupled perturbed Hartree−Fock (CPHF) equations. These are part of program packages for computation of analytic second derivatives of the ROHF energy.[204] Notice that the "extended" CPHF equations are needed in order to obtain the $U^{\mathbf{R}}_{ki}$ quantities where the k, i indices may correspond both to occupied and to virtual orbitals, which are not necessary for the analytic second derivatives of the ROHF energy. The appropriate computational procedure is described in refs 435 and 436. The quantities $h^{\mathbf{R}}_{ij}$, $(ij|kk)^{\mathbf{R}}$, and $(ik|jk)^{\mathbf{R}}$ in eq 88 represent derivatives of one- and two-electron integrals in the AO basis transformed into the MO basis (not including derivatives of the SCF eigenvectors)

$$h^{\mathbf{R}}_{ij} = \sum_{\mu\nu}^{AO} C_{\mu i} C_{\nu j} \nabla_{\mathbf{R}} h_{\mu\nu} \tag{91}$$

$$(ij|kl)^{\mathbf{R}} = \sum_{\mu\nu\rho\sigma}^{AO} C_{\mu i} C_{\nu j} C_{\rho k} C_{\sigma l} \nabla_{\mathbf{R}} (\mu\nu|\rho\sigma) \tag{92}$$

To summarize, the derivative of the effective one-excess-electron Hamiltonian can be built just like the derivative of the Fock matrix in CPHF equations for a closed shell system (of the cation), but using the SCF eigenvectors $C_{\alpha j}$ and the $U^{\mathbf{R}}_{ji}$ coefficients obtained from ROHF and extended CPHF calculation of the open shell neutral system.

Once the analytic gradient of the one-excess-electron energy is known, the velocity Verlet time propagation algorithm (cf. eqs 1 and 2) can be employed in order to solve equations of motion and

to compute the classical trajectories of the nuclei in the adiabatic electronic excited states.

9. Appendix B: Analytic Expression for Nonadiabatic Couplings in the "Frozen Ionic Bonds" Approximation and Nonadiabtic Dynamics

Inclusion of nonadiabatic effects in the molecular dynamics requires the calculation of the first-order nonadiabatic couplings $(\nabla_{\mathbf{R}})_{ij} \equiv \langle\psi_i|\nabla_{\mathbf{R}}|\psi_j\rangle$ between the electronic states ψ_i and ψ_j.

The nonadiabatic couplings employing the expansion of the ψ_j functions into the MO basis φ_i (cf. eq 76) contain two terms:

$$\langle\psi_j|\nabla_{\mathbf{R}}|\psi_i\rangle = \sum_k D^*_{kj}\nabla_{\mathbf{R}}D_{ki} + \sum_{kl} D^*_{lj}D_{ki}\langle\varphi_l|\nabla_{\mathbf{R}}|\varphi_k\rangle \quad (93)$$

The derivation of each of them will be briefly outlined.

The first term on the right-hand side involves the derivatives of the eigenvectors of the effective one-excess-electron Hamiltonian matrix $\nabla_{\mathbf{R}}D_{ki}$, which can be obtained from the derivative of the effective one-excess-electron Hamiltonian $\nabla_{\mathbf{R}}h'_{ij}$ (cf. eq 86). For this purpose, vector $\mathbf{E}$ for the diagonal matrix elements of eigenvalues ϵ_i of the Hamiltonian $\mathbf{h}'$ is introduced, and $\mathbf{D}$ is the unitary matrix of the corresponding eigenvectors:

$$\mathbf{h}'\mathbf{D} = \mathbf{D}\mathbf{E} \quad (94)$$

$$\mathbf{D}^\dagger\mathbf{D} = 1 \quad (95)$$

The derivative of the eigenvalues can be obtained by multiplying eq 94 by $\mathbf{D}^\dagger$ from the left and performing the derivative (taking into account that the derivative of the normalization condition (eq 95) is zero):

$$(\nabla_{\mathbf{R}}\mathbf{E})_{ii} = (\mathbf{D}^\dagger\nabla_{\mathbf{R}}\mathbf{h}'\mathbf{D})_{ii} \quad (96)$$

Notice that eq 96 holds only for the diagonal elements of the matrix $\mathbf{E}$, while an analogous equation for the whole matrix $\nabla_{\mathbf{R}}\mathbf{E}$ is not valid.

To obtain the derivative of eigenvectors $\nabla_{\mathbf{R}}\mathbf{D}$, the solution has to be searched in the following form:

$$\nabla_{\mathbf{R}}\mathbf{D} = \mathbf{D}\mathbf{X} \quad (97)$$

Since $\mathbf{D}$ is unitary, $\mathbf{X}$ is uniquely defined, and the derivative of the normalization condition (eq 95) implies the antihermiticity of $\mathbf{X}$:

$$\mathbf{X}^\dagger + \mathbf{X} = 0 \quad (98)$$

Performing the derivative of eq 94

$$(\nabla_{\mathbf{R}}\mathbf{h}')\mathbf{D} + \mathbf{h}'(\nabla_{\mathbf{R}}\mathbf{D}) = (\nabla_{\mathbf{R}}\mathbf{D})E + \mathbf{D}\nabla_{\mathbf{R}}\mathbf{E} \quad (99)$$

and multiplying this equation by $\mathbf{D}^\dagger$ from the left using eqs 94 and 97, one obtains

$$\mathbf{X}\mathbf{E} - \mathbf{E}\mathbf{X} = \mathbf{D}^\dagger(\nabla_{\mathbf{R}}\mathbf{h}')\mathbf{D} - \nabla_{\mathbf{R}}\mathbf{E} \equiv \mathbf{Y} \quad (100)$$

The right-hand side matrix is labeled by $\mathbf{Y}$; it can be easily verified that it is Hermitian, and due to eq 96, it has zeros on its diagonal. Since the matrix $\mathbf{E}$ is diagonal, eq 100 can be explicitly solved for the matrix elements of $\mathbf{X}$

$$X_{ij} = \frac{Y_{ij}}{E_{jj} - E_{ii}} \qquad (i \neq j);\ X_{ii} = 0 \quad (101)$$

Notice that this equation is in agreement with the requirement of the antihermiticity of $\mathbf{X}$ (eq 98). Furthermore, if the eigenvalues of the $\mathbf{h}'$ matrix are degenerate, the denominator in eq 101 becomes zero, which is in agreement with the fact that eigenvectors corresponding to the same eigenvalue are not uniquely defined. The explicit expression for the matrix elements of $\mathbf{X}$, eq 101, together with eq 97 yields the needed derivative of eigenvectors $\nabla_{\mathbf{R}}\mathbf{D}$.

For the second term on the right-hand side of eq 93, the expansion from the MO basis into the AO basis is used:

$$\varphi_i = \sum_\alpha C_{\alpha i}\chi_\alpha \quad (102)$$

which yields

$$\langle\varphi_j|\nabla_{\mathbf{R}}|\,\varphi_i\rangle = \sum_{\alpha\beta} C^*_{\beta j}S_{\beta\alpha}\nabla_{\mathbf{R}}C_{\alpha i} + \sum_{\alpha\beta} C^*_{\beta j}C_{\alpha i}\langle\chi_\beta|\nabla_{\mathbf{R}}|\chi_\alpha\rangle \quad (103)$$

where $S_{\beta\alpha}$ is the overlap matrix and the derivatives of the SCF eigenvectors $\nabla_{\mathbf{R}}C_{\alpha i}$ can be obtained from the extended coupled perturbed Hartree−Fock coefficients $\mathbf{U}^{\mathbf{R}}$, which have already been outlined for the adiabatic MD in Appendix A. The first term on the right-hand side of eq 103 thus simplifies in the matrix notation to

$$\mathbf{C}^\dagger\mathbf{S}\nabla_{\mathbf{R}}\mathbf{C} = \mathbf{C}^\dagger\mathbf{S}\mathbf{C}\mathbf{U}^{\mathbf{R}} = \mathbf{U}^{\mathbf{R}} \quad (104)$$

where the orthonormality of the SCF eigenvectors $\mathbf{C}^\dagger\mathbf{S}\mathbf{C} = 1$ has been used.

The evaluation of the second term on the right-hand side of eq 103 requires the integrals in the contracted Cartesian Gaussian AO basis:

$$\chi_\alpha = \sum_\gamma K_{\gamma\alpha}\phi_\gamma \quad (105)$$

Since the contraction coefficients $K_{\gamma\alpha}$ are constant, the transformation to a primitive basis ϕ_γ is simple:

$$\langle\chi_\beta|\nabla_{\mathbf{R}}|\chi_\alpha\rangle = \sum_{\gamma\delta} K_{\gamma\alpha}K_{\delta\beta}\langle\phi_\delta|\nabla_{\mathbf{R}}|\phi_\gamma\rangle \quad (106)$$

The integrals in the primitive AO basis $\langle\phi_\delta|\nabla_{\mathbf{R}}|\phi_\gamma\rangle$ vanish, unless the derivative is taken with respect to the nuclear coordinate of the atom, at which the ϕ_γ function is centered. Introducing the shorthand notation

$$S(\delta;i_\gamma,j_\gamma,k_\gamma,\zeta_\gamma) = \int (x - X_\delta)^{i_\delta}(y - Y_\delta)^{j_\delta} \times (z - Z_\delta)^{k_\delta}\mathrm{e}^{-\zeta_\delta|r-R_\delta|^2}(x - X_\gamma)^{i_\gamma}(y - Y_\gamma)^{j_\gamma} \times (z - Z_\gamma)^{k_\gamma}\mathrm{e}^{-\zeta_\gamma|r-R_\gamma|^2}\,\mathrm{d}x\,\mathrm{d}y\,\mathrm{d}z \quad (107)$$

the nonvanishing x component can be written as

$$\left\langle \phi_\delta \left| \frac{\partial}{\partial X_\gamma} \right| \phi_\gamma \right\rangle = -i_\gamma S(\delta; i_\gamma - 1, j_\gamma, k_\gamma, \zeta_\gamma) + 2\zeta_\gamma S(\delta; i_\gamma + 1, j_\gamma, k_\gamma, \zeta_\gamma) \quad (108)$$

and analogous equations for the y and z components hold. The AO derivative coupling integrals are thus transformed to overlap integrals over Cartesian Gaussian functions with different angular momenta, which are well-known (see, e.g., ref 204).

In summary, the implementation of simple analytic expressions derived for nonadiabatic couplings in the framework of the "frozen ionic bonds" approximation allows one to carry out nonadiabatic dynamics at low computational demand.

10. References

(1) Zewail, A. H. *Femtochemistry*; World Scientific: Singapore, 1994.
(2) Manz, J., Wöste, L., Eds. *Femtosecond Chemistry*; VCH Verlagsgesellschaft mbH: Weinheim, Germany, 1995; Vols. 1 and 2.
(3) Chergui, M., Ed. *Femtochemistry*; World Scientific: Singapore, 1996.
(4) Sundström, V., Ed. *Nobel Symposium Book: Femtochemistry and Femtobiology: Ultrafast Reaction Dynamics at Atomic Scale Resolution*; World Scientific: Imperial College Press: London, 1997.
(5) Zewail, A. H. *J. Phys. Chem. A* **2000**, *104*, 5660.
(6) Zare, R. N. *Science* **1998**, *279*, 1875.
(7) Shank, C. V. *Opt. Lett.* **1987**, *12*, 483.
(8) Fleming, G. R. *Chemical Applications of Ultrafast Spectroscopy*; Oxford University Press: 1986.
(9) Fleming, G. R.; Joo, T.; Cho, M.; Zewail, A. H.; Lehotkov, V. S.; Marcus, R. A.; Pollak, E.; Tannor, D. J.; Mukamel, S. *Adv. Chem. Phys.* **1986**, *101*, 141.
(10) Wynne, K.; Hochstrasser, R. M. *Adv. Chem. Phys.* **1999**, *107*, 263.
(11) Brixner, T.; Gerber, G. *ChemPhysChem* **2003**, *4*, 418.
(12) Bonačić-Koutecký, V.; Fantucci, P.; Koutecký, J. *Chem. Rev.* **1991**, *91*, 1035.
(13) Castleman, A. W., Jr.; Bowen, K. H., Jr. *J. Phys. Chem.* **1996**, *100*, 12911.
(14) Jortner, J. *Faraday Discuss.* **1997**, *108*, 1.
(15) Landman, U. *Int. J. Mod. Phys.* **1992**, *B6*, 3623.
(16) Haberland, H., Ed. *Clusters of Atoms and Molecules*; Springer Series in Chemical Physics 52; Springer-Verlag: Berlin, Heidelberg, New York, 1994.
(17) Ekardt, W., Ed. *Metal Clusters*; John Wiley & Sons: Chichester, 1999.
(18) Jena, P., Khanna, S. N., Rao, B. K., Eds. *Cluster and Nanostructure Interfaces*; World Scientific: Singapore, 1999.
(19) Guet, C., Hobza, P., Spiegelman, F., David, F., Eds. *Atomic clusters and nanoparticles*; NATO Advanced Study Institute; Springer-Verlag: Berlin, Heidelberg, and EDP Sciences; Les Ulis, Paris, Cambridge, 2001.
(20) Castleman, A. W., Jr.; Keesee, R. G. *Chem. Rev.* **1986**, *86*, 589.
(21) Zhong, Q.; Castleman, A. W., Jr. *Chem. Rev.* **2000**, *100*, 4039.
(22) Stolow, A.; Bragg, A. E.; Neumark, D. M. *Chem. Rev.* **2004**, *104*, 1719.
(23) Dermota, T. E.; Zhong, Q.; Castleman, A. W., Jr. *Chem. Rev.* **2004**, *104*, 1861.
(24) König, L.; Rabin, I.; Schulze, W.; Ertl, G. *Science* **1996**, *274*, 1353.
(25) Felix, C.; Sieber, C.; Harbich, W.; Buttet, J.; Rabin, I.; Schulze, W.; Ertl, G. *Chem. Phys. Lett.* **1998**, *313*, 105.
(26) Rabin, I.; Schulze, W.; Ertl, G.; Felix, C.; Sieber, C.; Harbich, W.; Buttet, J. *Chem. Phys. Lett.* **2000**, *320*, 59.
(27) Felix, C.; Sieber, S.; Harbich, W.; Buttet, J.; Rabin, I.; Schulze, W.; Ertl, G. *Phys. Rev. Lett.* **2001**, *86*, 2992.
(28) Harbich, W.; Felix, C. *C. R. Phys.* **2002**, *3*, 289.
(29) Sanchez, A.; Abbet, S.; Heiz, U.; Schneider, W. D.; Hakkinen, H.; Barnett, R. N.; Landman, U. *J. Phys. Chem. A* **1999**, *103*, 9573.
(30) Abbet, S.; Heiz, U.; Hakkinen, H.; Landman, U. *Phys. Rev. Lett.* **2001**, *86*, 5950.
(31) Abbet, S.; Ferrari, A. M.; Giordano, L.; Pacchioni, G.; Hakkinen, H.; Landman, U.; Heiz, U. *Surf. Sci.* **2002**, *514*, 249.
(32) Stegemann, B.; Bernhardt, T.; Kaiser, B.; Rademann, K. *Surf. Sci.* **2002**, *511*, 153.
(33) Bernhardt, T. M.; Stegemann, B.; Kaiser, B.; Rademann, K. *Angew. Chem.* **2003**, *115*, 209.
(34) Kaiser, B.; Stegemann, B. *ChemPhysChem* **2004**, *5*, 37.
(35) Nieman, G. C.; Parks, E. K.; Richtsmeier, S. C.; Liu, K.; Pobo, L. G.; Riley, S. J. *High Temp. Sci.* **1986**, *22*, 115.
(36) Kinne, M.; Rademann, K. *Phys. Chem. Chem. Phys.* **1998**, *284*, 263.
(37) Fielicke, A.; Rademann, K. *J. Phys. Chem. A* **2000**, *104*, 6979.
(38) Fielicke, A.; Rademann, K. *Phys. Chem. Chem. Phys.* **2002**, *4*, 2621.
(39) Sun, Q.; Rao, B. K.; Jena, P.; Stolcic, D.; Ganteför, G.; Kawazoe, Y. *Chem. Phys. Lett.* **2004**, *387*, 29.
(40) Sun, Q.; Jena, P.; Kim, Y. D.; Fischer, M.; Ganteför, G. *J. Chem. Phys.* **2004**, *120*, 6510.
(41) Stolcic, D.; Fischer, M.; Ganteför, G.; Kim, Y. D.; Sun, Q.; Jena, P. *J. Am. Chem. Soc.* **2003**, *125*, 2848.
(42) Stolcic, D.; Kim, Y. D.; Ganteför, G. *Chem. Phys. Lett.* **2004**, *383*, 80.
(43) Hagen, J.; Socaciu, L. D.; Le Roux, J.; Popolan, D.; Bernhardt, T. M.; Wöste, L.; Mitrić, R.; Bonačić-Koutecký, V. *J. Am. Chem. Soc.* **2004**, *126*, 3442.
(44) Socaciu, L. D.; Hagen, J.; Bernhardt, T. M.; Wöste, L.; Heiz, U.; Hakkinen, H.; Landman, U. *J. Am. Chem. Soc.* **2003**, *125*, 10437.
(45) Zemski, K.; Justes, D. R.; Castleman, A. Q., Jr. *J. Phys. Chem. B* **2002**, *106*, 6136.
(46) Justes, D. R.; Mitrić, R.; Moore, N. A.; Bonačić-Koutecký, V.; Castleman, A. W., Jr. *J. Am. Chem. Soc.* **2003**, *125*, 6289.
(47) Xu, J.; Rodgers, M. T.; Griffin, J. B.; Armentrout, P. B. *J. Chem. Phys.* **1998**, *108*, 9339.
(48) Engeser, M.; Weiske, T.; Schröder, D.; Schwarz, H. *J. Phys. Chem. A* **2003**, *107*, 2855.
(49) Jortner, J. *Z. Phys. D* **1992**, *24*, 247.
(50) De Heer, W. A. *Rev. Mod. Phys.* **1993**, *65*, 611.
(51) Wales, D. J. *J. Chem. Phys.* **1990**, *92*, 4283.
(52) Wales, D. J.; Berry, R. S. *J. Chem. Phys.* **1990**, *92*, 4473.
(53) Berry, R. S. *C. R. Phys.* **2002**, *3*, 319.
(54) Schmidt, M.; Haberland, H. *C. R. Phys.* **2002**, *3*, 327.
(55) Haberland, H. In *Atomic clusters and nanoparticles*; Guet, C., Hobza, P., Spiegelman, F., David, F., Eds.; NATO Advanced Study Institute; Springer-Verlag: Berlin, Heidelberg, and EDP Sciences: Les Ulis, Paris, Cambridge, 2001.
(56) Wales, D. J. *Energy landscapes*; Cambridge University Press: Cambridge, U.K., 2003.
(57) Baumert, T.; Brixner, T.; Seyfried, V.; Strehle, M.; Gerber, G. *Appl. Phys. B* **1997**, *65*, 779.
(58) Assion, A.; Baumert, T.; Bergt, M.; Brixner, T.; Kiefer, B.; Seyfried, V.; Strehle, M.; Gerber, G. *Science* **1998**, *282*, 919.
(59) Hornung, T.; Meier, R.; Motzkus, M. *Chem. Phys. Lett.* **2000**, *326*, 445.
(60) Vajda, S.; Rosendo-Francisco, P.; Kaposta, C.; Krenz, M.; Lupulescu, L.; Wöste, L. *Eur. Phys. J. D* **2001**, *16*, 161.
(61) Levies, R. J.; Menkir, G. M.; Rabitz, H. *Science* **2001**, *292*, 709.
(62) Yelin, D.; Meshulach, D.; Silberberg, Y. *Opt. Lett.* **1997**, *22*, 1793.
(63) Efimov, A.; Moores, M. D.; Beach, N. M.; Krause, J. L.; Reitze, D. H. *Opt. Lett.* **1998**, *23*, 1915.
(64) Brixner, T.; Strehle, M.; Gerber, G. *Appl. Phys. B* **1999**, *68*, 281.
(65) Zeek, E.; Maginnis, K.; Backus, S.; Russek, U.; Murnane, M. M.; Mourou, G.; Kapteyn, H. C.; Vdovin, G. *Opt. Lett.* **1999**, *24*, 493.
(66) Zeek, E.; Bartels, R.; Murnane, M. M.; Kapteyn, H. C.; Backus, S.; Vdovin, G. *Opt. Lett.* **2000**, *25*, 587.
(67) Efimov, A.; Moores, M. D.; Mei, B.; Krause, J. L.; Siders, C. W.; Reitze, D. H. *Appl. Phys. B* **2000**, *70*, 133.
(68) Zeidler, D.; Hornung, T.; Proch, D.; Motzkus, M. *Appl. Phys. B* **2000**, *70*, 125.
(69) Meshulach, D.; Yelin, D.; Silberberg, Y. *J. Opt. Soc. Am. B* **1998**, *15*, 1615.
(70) Meshulach, D.; Silberberg, Y. *Nature* **1998**, *396*, 239.
(71) Meshulach, D.; Silberberg, Y. *Phys. Rev. A* **1999**, *60*, 1287.
(72) Hornung, T.; Meier, R.; Zeidler, D.; Kompa, K. L.; Proch, D.; Motzkus, M. *Appl. Phys. B* **2000**, *71*, 277.
(73) Weinacht, T. C.; White, J. L.; Bucksbaum, P. H. *J. Phys. Chem. A* **1999**, *103*, 10166.
(74) Weinacht, T. C.; Ahn, J.; Bucksbaum, P. H. *Nature* **1999**, *397*, 233.
(75) Bartels, R.; Backus, S.; Zeek, E.; Misoguti, L.; Vdovin, G.; Christov, I. P.; Murnane, M. M.; Kapteyn, H. C. *Nature* **2000**, *164*.
(76) Kunde, J.; Baumann, B.; Arlt, S.; Morier-Genoud, F.; Siegner, U.; Keller, U. *Appl. Phys. Lett.* **2000**, *77*, 924.
(77) Dantus, M.; Lozovoy, V. V. *Chem. Rev.* **2004**, *104*, 1813.
(78) Daniel, C.; Full, J.; Gonzalez, L.; Lupulescu, C.; Manz, J.; Merli, A.; Vajda, S.; Wöste, L. *Science* **2003**, *299*, 536.
(79) Bonačić-Koutecký, V.; Pittner, J.; Reichardt, D.; Fantucci, P.; Koutecký, J. In *Metal Clusters*; Ekardt, W., Ed.; John Wiley & Sons, Ltd.: 1999; p 91.
(80) Ekardt, W.; Schöne, W. D.; Pacheco, J. M. In *Metal Clusters*; Ekardt, W., Ed.; John Wiley & Sons: Chichester, U.K., 1999.
(81) Yannouleas, C.; Landman, U.; Barnett, R. N. In *Metal Clusters*; Ekardt, W., Ed.; John Wiley & Sons: Chichester, U.K., 1999.
(82) Ballone, P.; Andreoni, W. In *Metal Clusters*; Ekardt, W., Ed.; John Wiley & Sons: Chichester, U.K., 1999.

(83) Bonačić-Koutecký, V.; Češpiva, L.; Fantucci, P.; Koutecký, J. *J. Chem. Phys.* **1993**, *98*, 7981.
(84) Bonačić-Koutecký, V.; Češpiva, L.; Fantucci, P.; Koutecký, J. *J. Chem. Phys.* **1994**, *100*, 490.
(85) Bonačić-Koutecký, V.; Burda, J.; Ge, M.; Mitrić, R.; Zampella, G.; Fantucci, R. *J. Chem. Phys.* **2002**, *117*, 3120.
(86) Bonačić-Koutecký, V.; Veyret, V.; Mitrić, R. *J. Chem. Phys.* **2001**, *115*, 10450.
(87) Mitrić, R.; Hartmann, M.; Pittner, J.; Bonačić-Koutecký, V. *Eur. Phys. J.* **2003**, *24*, 45.
(88) Wallace, W. T.; Wyrwas, R. B.; Whetten, R. L.; Mitrić, R.; Bonačić-Koutecký, V. *J. Am. Chem. Soc.* **2003**, *125*, 8408.
(89) Justes, D. R.; Castleman, A. W., Jr.; Mitrić, R.; Bonačić-Koutecký, V. *Eur. Phys. J. D* **2003**, *24*, 331.
(90) Fielicke, A.; Mitrić, R.; Meijer, G.; Bonačić-Koutecký, V.; von Helden, G. *J. Am. Chem. Soc.* **2003**, *125*, 15716.
(91) Kimble, M. L.; Castleman, A. W., Jr.; Mitrić, R.; Bürgel, C.; Bonačić-Koutecký, V. *J. Am. Chem. Soc.* **2004**, *126*, 2526.
(92) Sieber, C.; Buttet, J.; Harbich, W.; Félix, C.; Mitrić, R.; Bonačić-Koutecký, V. *Phys. Rev. A* **2004**, *70*, 04121.
(93) Häkkinen, H.; Landman, U. *Phys. Rev. B* **2000**, *62*, R2287.
(94) Häkkinen, H.; Landman, U. *J. Am. Chem. Soc.* **2001**, *123*, 9704.
(95) Häkkinen, H.; Yoon, B.; Landman, U.; Li, X.; Zhai, H. J.; Wang, L.-S. *J. Phys. Chem. A* **2003**, *107*, 6168.
(96) Yoon, B.; Häkkinen, H.; Landman, U. *J. Phys. Chem. A* **2003**, *107*, 4066.
(97) Häkkinen, H.; Yoon, B.; Landman, U.; Li, X.; Zhai, H. J.; Wang, L.-S. *J. Phys. Chem. A* **2003**, *107*, 6168.
(98) Bonačić-Koutecký, V.; Češpiva, L.; Fantucci, P.; Fuchs, C.; Koutecký, J.; Pittner, J. *Comments At. Mol. Phys.* **1995**, *31*, 233.
(99) Bonačić-Koutecký, V.; Pittner, J.; Fantucci, P.; Guest, M. F.; Koutecký, J. *J. Chem. Phys.* **1996**, *104*, 1427.
(100) Bonačić-Koutecký, V.; Pittner, J.; Koutecký, J. *Chem. Phys.* **1996**, *210*, 313.
(101) Bonačić-Koutecký, V.; Pittner, J.; Koutecký, J. *Z. Phys. D* **1997**, *40*, 441.
(102) Bonačić-Koutecký, V.; Pittner, J. *Chem. Phys.* **1997**, *225*, 173.
(103) Stolcic, D.; Fischer, M.; Ganteför, G.; Kim, Y. D.; Sun, Q.; Jena, P. *J. Am. Chem. Soc.* **2003**, *125*, 2848.
(104) Landman, U.; Scharf, D.; Jortner, J. *Phys. Rev. Lett.* **1985**, *54*, 1860.
(105) Barnett, R. N.; Landman, U.; Cleveland, C. L.; Jortner, J. *Phys. Rev. Lett.* **1987**, *59*, 811.
(106) Jungwirth, P.; Gerber, B. *Chem. Rev.* **1999**, *99*, 1583.
(107) Ermoshin, V. A.; Kazansky, A. K.; Engel, V. *J. Chem. Phys.* **1999**, *111*, 7807.
(108) Ermoshin, V. A.; Engel, V.; Meier, C. *J. Chem. Phys.* **2000**, *113*, 5770.
(109) Häkkinen, H.; Moseler, M.; Landman, U. *Phys. Rev. Lett.* **2002**, *89*, 033401-1.
(110) Moseler, M.; Häkkinen, H.; Landman, U. *Phys. Rev. Lett.* **2002**, *89*, 176103.
(111) Ellert, C.; Schmitt, M.; Schmidt, C.; Reinert, T.; Haberland, H. *Phys. Rev. Lett.* **1995**, *75*, 1731.
(112) Hartmann, M.; Pittner, J.; Bonačić-Koutecký, V.; Heidenreich, A.; Jortner, J. *J. Chem. Phys.* **1998**, *108*, 3096.
(113) Hartmann, M.; Pittner, J.; Bonačić-Koutecký, V.; Heidenreich, A.; Jortner, J. *J. Phys. Chem.* **1998**, *102*, 4069.
(114) Andrianov, I.; Bonačić-Koutecký, V.; Hartmann, M.; Manz, J.; Pittner, J.; Sundermann, K. *Chem. Phys. Lett.* **2000**, *318*, 256.
(115) Hartmann, M.; Pittner, J.; Bonačić-Koutecký, V. *J. Chem. Phys.* **2001**, *114*, 2106.
(116) Hartmann, M.; Pittner, J.; Bonačić-Koutecký, V. *J. Chem. Phys.* **2001**, *114*, 2123.
(117) Hartmann, M.; Mitrić, R.; Stanca, B.; Bonačić-Koutecký, V. *Eur. Phys. J. D* **2001**, *16*, 151.
(118) Bonačić-Koutecký, V.; Hartmann, M.; Pittner, J. *Eur. Phys. J. D* **2001**, *16*, 133.
(119) Mitrić, R.; Hartmann, M.; Stanca, B.; Bonačić-Koutecký, V.; Fantucci, P. *J. Phys. Chem. A* **2001**, *105*, 8892.
(120) Vajda, S.; Lupulescu, C.; Merli, A.; Budzyn, F.; Wöste, L.; Hartmann, M.; Pittner, J.; Bonačić-Koutecký, V. *Phys. Rev. Lett.* **2002**, *89*, 213404.
(121) Mitrić, R.; Hartmann, M.; Pittner, J.; Bonačić-Koutecký, V. *J. Phys. Chem. A* **2002**, *106*, 10477.
(122) Bonačić-Koutecký, V.; Mitrić, R.; Hartmann, M.; Pittner, J. *Int. J. Quantum Chem.* **2004**, *99*, 408.
(123) Henriksen, N. E.; Engel, V. *Int. Rev. Phys. Chem.* **2001**, *20*, 93.
(124) Heitz, M.-C.; Durand, G.; Spiegelman, F.; Meier, C. *J. Chem. Phys.* **2003**, *118*, 1282.
(125) Heitz, M.-C.; Durand, G.; Spiegelman, F.; Meier, C.; Mitrić, R.; Bonačić-Koutecký, V. *J. Chem. Phys.* **2004**, *121*, 9906.
(126) Tannor, D. J.; Rice, S. A. *J. Chem. Phys.* **1985**, *83*, 5013.
(127) Tannor, D. J.; Rice, S. A. *Adv. Chem. Phys.* **1988**, *70*, 441.
(128) Paramonov, G. K.; Savva, V. A. *Phys. Lett.* **1983**, *97A*, 340.
(129) Brumer, P.; Shapiro, M. *Faraday Discuss. Chem. Soc.* **1986**, *82*, 177.
(130) Shapiro, M.; Brumer, P. *J. Chem. Phys.* **1986**, *84*, 4103.
(131) Peirce, A. P.; Dahleh, M. A.; Rabitz, H. *Phys. Rev. A* **1988**, *37*, 4950.
(132) Baumert, T.; Buhler, B.; Grosser, M.; Thalweiser, R.; Weiss, V.; Wiedenmann, E.; Gerber, G. *J. Phys. Chem.* **1991**, *95*, 8103.
(133) Baumert, T.; Gerber, G. *Isr. J. Chem.* **1994**, *34*, 103.
(134) Herek, J. L.; Materny, A.; Zewail, A. H. *Chem. Phys. Lett.* **1994**, *228*, 15.
(135) Shnitman, A.; Sofer, I.; Golub, I.; Yogev, A.; Shapiro, M.; Chen, Z.; Brumer, P. *Phys. Rev. Lett.* **1996**, *76*, 2886.
(136) Schwoerer, H.; Pausch, R.; Heid, M.; Engel, V.; Kiefer, W. *J. Chem. Phys.* **1997**, *107*, 9749.
(137) Nicole, C.; Bouchene, M. A.; Meier, C.; Magnier, S.; Schreiber, E.; Girard, B. *J. Chem. Phys.* **1999**, *111*, 7857.
(138) Pesce, L.; Amitay, Z.; Uberna, R.; Leone, S. R.; Kosloff, R. *J. Chem. Phys.* **2001**, *114*, 1259.
(139) Shen, Z. W.; Chen, T.; Heid, M.; Kiefer, W.; Engel, V. *Eur. Phys. J. D* **2001**, *14*, 167.
(140) Grègoire, G.; Mons, M.; Dimicoli, I.; Piuzzi, F.; Charron, E.; Dedonder-Lardeux, C.; Jouvet, C.; Matenchard, S.; Solgadi, D.; Suzor-Weiner, A. *Eur. Phys. J. D* **1998**, *1*, 187.
(141) Hornung, T.; Motzkus, M.; de Vivie-Riedle, R. *J. Chem. Phys.* **2001**, *115*, 3105.
(142) Rodriguez, G.; Eden, J. G. *Chem. Phys. Lett.* **1993**, *205*, 371.
(143) Rodriguez, G.; John, P. C.; Eden, J. G. *J. Chem. Phys.* **1995**, *103*, 10473.
(144) Pausch, R.; Heid, M.; Chen, T.; Kiefer, W.; Schwoerer, H. *J. Chem. Phys.* **1999**, *110*, 9560.
(145) Pausch, R.; Heid, M.; Chen, T.; Kiefer, W.; Schwoerer, H. *J. Raman Spectrosc.* **2000**, *31*, 7.
(146) Uberna, R.; Amitay, Z.; Loomis, R. A.; Leone, S. R. *Faraday Discuss.* **1999**, *113*, 385.
(147) Vajda, S.; Bartelt, A.; Kaposta, E.-C.; Leisner, T.; Lupulescu, C.; Minemoto, S.; Rosenda-Francisco, P.; Wöste, L. *Chem. Phys.* **2001**, *267*, 231.
(148) Bartelt, A.; Minemoto, S.; Lupulescu, C.; Vajda, S.; Wöste, L. *Eur. Phys. J. D* **2001**, *16*, 127.
(149) Vajda, S.; Lupulescu, C.; Bartelt, A.; Budzyn, F.; Rosendo-Francisco, P.; Wöste, L. In *Femtochemistry and Femtobiology*; Douhal, A., Santamaria, J., Eds.; World Scientific Publishing: Singapore, 2002.
(150) Bartelt, A.; Lindinger, A.; Lupulescu, C.; Vajda, S.; Wöste, L. *Phys. Chem. Chem. Phys.* **2003**, *5*, 3610.
(151) Lupulescu, C.; Lindinger, A.; Plewicky, M.; Merli, A.; Weber, S. M.; Wöste, L. *Chem. Phys.* **2004**, *296*, 63.
(152) Bartelt, A. Steuerung der Wellenpaketdynamik in kleinen Alkaliclustern mit optimierten Femtosekundenpulsen. Ph.D. Thesis, Freie Universität Berlin, 2002.
(153) Ballard, J. B.; Stauffer, H. U.; Amitay, Z.; Leone, S. R. *J. Chem. Phys.* **2002**, *116*, 1350.
(154) Schäfer-Bung, B.; Mitrić, R.; Bonačić-Koutecký, V.; Bartelt, A.; Lupulescu, C.; Lindinger, A.; Vajda, S.; Weber, S. M.; Wöste, L. *J. Phys. Chem. A* **2004**, *108*, 4175.
(155) Bardeen, C. J.; Yakovlev, V. V.; Wilson, K. R.; Carpenter, S. D.; Weber, P. M.; Warren, W. S. *Chem. Phys. Lett.* **1997**, *280*, 151.
(156) Brixner, T.; Damrauer, N. H.; Niklaus, P.; Gerber, G. *Nature* **2001**, *414*, 57.
(157) Daniel, C.; Full, J.; González, L.; Kaposta, E.-C.; Krenz, M.; Lupulescu, C.; Manz, J.; Minemoto, S.; Oppel, M.; Rosenda-Francisco, P.; Vajda, S.; Wöste, L. *Chem. Phys.* **2001**, *267*, 247.
(158) Damrauer, N. H.; Dietl, C.; Krampert, G.; Lee, S. H.; Jung, K. H.; Gerber, G. *Eur. Phys. J. D* **2002**, *20*, 71.
(159) Herek, J. L.; Wohlleben, W.; Cogdell, R. J.; Zeidler, D.; Motzkus, M. *Nature* **2002**, *417*, 553.
(160) Zewail, A. H. *Faraday Discuss. Chem. Soc.* **1991**, *91*, 207.
(161) Mokhtari, A.; Cong, P.; Herek, J. L.; Zewail, A. H. *Nature* **1990**, *348*, 225.
(162) Dantus, M.; Bowman, R. M.; Gruebele, M.; Zewail, A. H. *J. Chem. Phys.* **1989**, *91*, 7489.
(163) Weaver, A.; Metz, R. B.; Bradforth, S. E.; Neumark, D. M. *J. Chem. Phys.* **1990**, *93*, 5352.
(164) Metz, R. B.; Neumark, D. M. *J. Chem. Phys.* **1992**, *97*, 962.
(165) Neumark, D. M. *Acc. Chem. Res.* **1993**, *26*, 33.
(166) Greenblatt, B. J.; Zanni, M. T.; Neumark, D. M. *J. Chem. Phys.* **1999**, *111*, 10566.
(167) Zanni, M. T.; Greenblatt, B. J.; Davis, A. V.; Neumark, D. M. *J. Chem. Phys.* **1999**, *111*, 2991.
(168) Neumark, D. M. *Annu. Rev. Phys. Chem.* **2001**, *52*, 255.
(169) Greenblatt, B. J.; Zanni, M. T.; Neumark, D. M. *J. Chem. Phys.* **2000**, *112*, 601.
(170) Wester, R.; Davis, A. V.; Bragg, A. E.; Neumark, D. M. *Phys. Rev. A* **2002**, *65*, 051201.
(171) Frischkorn, C.; Bragg, A. E.; Davis, A. V.; Wester, R.; Neumark, D. M. *J. Chem. Phys.* **2001**, *115*, 11185.
(172) Burnett, S. M.; Stevens, A. E.; Feigerle, C. S.; Lineberger, W. C. *Chem. Phys. Lett.* **1983**, *100*, 124.
(173) Ervin, K. M.; Ho, J.; Lineberger, W. C. *J. Chem. Phys.* **1989**, *91*, 5974.
(174) Wenthold, P. G.; Hrovat, D.; Borden, W. T.; Lineberger, W. C. *Science* **1996**, *272*, 1456.

(175) Wolf, S.; Sommerer, G.; Rutz, S.; Schreiber, E.; Leisner, T.; Wöste, L.; Berry, R. S. *Phys. Rev. Lett.* **1995**, *74*, 4177.
(176) Berry, R. S.; Bonačić-Koutecký, V.; Gaus, J.; Leisner, T.; Manz, J.; Reischl-Lenz, B.; Ruppe, H.; Rutz, S.; Schreiber, E.; Vajda, S.; de Vivie-Riedle, R.; Wolf, S.; Wöste, L. *Phys. Rev. Lett.* **1997**, *101*, 101.
(177) Boo, D. W.; Ozaki, Y.; Andersen, L. H.; Lineberger, W. C. *J. Phys. Chem. A* **1997**, *101*, 6688.
(178) Pontius, N.; Bechthold, P. S.; Neeb, M.; Eberhardt, W. *Phys. Rev. Lett.* **2000**, *84*, 1132.
(179) Ihee, H.; Lobatsov, V. A.; Gomez, U. M.; Goodman, B. M.; Srinivasan, R.; Ruan, C.; Zewail, A. H. *Science* **2001**, *291*, 458.
(180) Chen, L. X.; Jäger, W. J. H.; Jennings, G.; Gosztola, D. J.; Munkholm, A.; Hessler, J. P. *Science* **2001**, *292*, 262.
(181) Bernhardt, T. M.; Hagen, J.; Socaciu, L. D.; Le Roux, J.; Popolan, D.; Vaida, M.; Wöste, L.; Mitrić, R.; Bonačić-Koutecký, V.; Heidenreich, A.; Jortner, J. *ChemPhysChem*, in press.
(182) Baumert, T.; Grosser, R.; Thalweiser, R.; Gerber, G. *Phys. Rev. Lett.* **1991**, *67*, 3753.
(183) Baumert, T.; Röttgermann, C.; Rothenfusser, C.; Thalweiser, R.; Weiss, V.; Gerber, G. *Phys. Rev. Lett.* **1992**, *69*, 1512.
(184) de Vivie-Riedle, R.; Reischl, B.; Rutz, S.; Schreiber, E. *J. Phys. Chem.* **1995**, *99*, 16829.
(185) Rose, T. S.; Rosker, M. J.; Zewail, A. *J. Chem. Phys.* **1988**, *88*, 6672.
(186) Cong, P.; Mokhtari, A.; Zewail, A. H. *Chem. Phys. Lett.* **1990**, *172*, 109.
(187) Gruebele, M.; Roberts, G.; Dantus, M.; Bowman, R. M.; Zewail, A. H. *Chem. Phys. Lett.* **1990**, *166*, 459.
(188) Berg, L. E.; Beutter, M.; Hansson, T. *Chem. Phys. Lett.* **1996**, *253*, 327.
(189) Heufelder, J.; Ruppe, H.; Rutz, S.; Schreiber, E.; Wöste, L. *Chem. Phys. Lett.* **1997**, *269*, 1.
(190) Potter, E. D.; Herek, J. L.; Pedersen, S.; Liu, Q.; Zewail, A. H. *Nature (London)* **1992**, *355*, 66.
(191) de Vivie-Riedle, R.; Kobe, K.; Manz, J.; Meyer, W.; Reischl, B.; Rutz, S.; Schreiber, E.; Wöste, L. *J. Phys. Chem.* **1996**, *100*, 7789.
(192) Baumert, T.; Thalweiser, R.; Gerber, G. *Chem. Phys. Lett.* **1993**, *209*, 29.
(193) Reischl, B.; de Vivie-Riedle, R.; Rutz, S.; Schreiber, E. *J. Chem. Phys.* **1996**, *104*, 8857.
(194) Schön, J.; Köppel, H. *J. Phys. Chem. A* **1999**, *103*, 8579.
(195) Gauss, J. Ph.D. Thesis, Freie Universität Berlin, 1995.
(196) Ruppe, H.; Rutz, S.; Schreiber, E.; Wöste, L. *Chem. Phys. Lett.* **1996**, *257*, 356.
(197) Ruff, A.; Rutz, S.; Schreiber, E.; Wöste, L. *Z. Phys. D* **1996**, *37*, 175.
(198) Kühling, H.; Kobe, K.; Rutz, S.; Schreiber, E.; Wöste, L. *J. Phys. Chem.* **1994**, *98*, 6679.
(199) Vajda, S.; Rutz, S.; Heufelder, J.; Rosendo, P.; Ruppe, H.; Wetzel, P.; Wöste, L. *J. Phys. Chem. A* **1998**, *102*, 4066.
(200) Car, R.; Parrinello, M. *Phys. Rev. Lett.* **1985**, *55*, 2471.
(201) Leforestier, C. *J. Chem. Phys.* **1978**, *68*, 4406.
(202) Barnett, R. N.; Landman, U. *Phys. Rev. B* **1993**, *48*, 2081.
(203) Pulay, P. *Mol. Phys.* **1969**, *17*, 197.
(204) Yamaguchi, Y.; Osamura, Y.; Goddard, J. D.; Schaefer, H. F., III. *A New Dimension to Quantum Chemistry*; Oxford University Press: 1994.
(205) Gaw, J. F.; Yamaguchi, Y.; Schaefer, H. F., III. *J. Chem. Phys.* **1984**, *81*, 6395.
(206) Gaw, J. F.; Handy, N. C.; Palmieri, P.; Esposti, A. D. *J. Chem. Phys.* **1988**, *89*, 959.
(207) Chong, D. P., Ed. *Recent advances in density functional methods*; World Scientific: Singapore, 1997; Vol. I.
(208) Barone, V., Bencini, A., Fantucci, P., Eds. *Recent advances in density functional methods*; World Scientific: Singapore, 2002; Vol. III.
(209) Bartlett, R. J., Ed. *Recent advances in coupled-cluster methods*; World Scientific: Singapore, 1997; Vol. III.
(210) Hirao, K., Ed. *Recent advances in multireference methods*; World Scientific: Singapore, 1997; Vol. IV.
(211) Van Caillie, C.; Amos, R. D. *Chem. Phys. Lett.* **1999**, *308*, 249.
(212) Van Caillie, C.; Amos, R. D. *Chem. Phys. Lett.* **2000**, *317*, 159.
(213) Furche, F.; Ahlrichs, R. *J. Chem. Phys.* **2002**, *117*, 7433.
(214) Köhn, A.; Hättig, C. *J. Chem. Phys.* **2002**, *117*, 7433.
(215) Doltsinis, N. L.; Marx, D. *J. Theor. Comput. Chem.* **2002**, *1*, 319.
(216) Donoso, A.; Martens, C. *J. Phys. Chem.* **1998**, *102*, 4291.
(217) Hammes-Schiffer, S. *J. Phys. Chem. A* **1998**, *102*, 10443.
(218) Hack, M. D.; Truhlar, D. G. *J. Phys. Chem. A* **2000**, *104*, 7917.
(219) Hack, M. D.; Wensman, A. M.; Truhlar, D. G. *J. Chem. Phys.* **2001**, *115*, 1172.
(220) Donoso, A.; Martens, C. C. *J. Chem. Phys.* **2000**, *112*, 3980.
(221) Miller, W. H. *J. Phys. Chem.* **2001**, *105*, 2942.
(222) Sun, X.; Wang, H.; Miller, W. H. *J. Chem. Phys.* **1998**, *109*, 7064.
(223) Wang, H.; Thoss, M.; Miller, W. H. *J. Chem. Phys.* **2001**, *115*, 2979.
(224) Stock, G.; Thoss, M. *Phys. Rev. Lett.* **1997**, *78*, 578.
(225) Thoss, M.; Stock, G. *Phys. Rev. A* **1999**, *59*, 64.
(226) Ben-Nun, M.; Quenneville, J.; Martínez, T. J. *J. Phys. Chem. A* **2000**, *104*, 5161.
(227) Tully, J. C. In *Classical and Quantum Dynamics in Condensed Phase Simulations*; Berne, B. J., Ciccoti, G., Coker, D. F., Eds.; World Scientific: Singapore, 1998.
(228) Tully, J. C. In *Modern Methods for Multidimensional Dynamics Computations in Chemistry*; Thompson, D. L., Ed.; World Scientific: Singapore, 1998.
(229) Shapiro, M.; Brumer, P. *Int. Rev. Phys. Chem.* **1994**, *13*, 187.
(230) Gordon, R. G.; Rice, S. A. *Annu. Rev. Phys. Chem.* **1997**, *48*, 601.
(231) Zhu, L. C.; Kleiman, V.; Li, X. N.; Lu, S. P.; Trentelman, K.; Gordon, R. J. *Science* **1995**, *270*, 77.
(232) Chen, C.; Elliott, D. S. *Phys. Rev. Lett.* **1990**, *65*, 1737.
(233) Park, S. M.; Lu, R. J.; Gordon, R. J. *J. Chem. Phys.* **1991**, *94*, 8622.
(234) Xing, G. Q.; Wang, X. B.; Huang, X.; Bersohn, R. *J. Chem. Phys.* **1996**, *104*, 826.
(235) Assion, A.; Baumert, T.; Seyfried, V.; Weiss, V.; Wiedenmann, E.; Gerber, G. *Z. Phys. D* **1996**, *36*, 265.
(236) Baumert, T.; Helbing, J.; Gerber, G. *Adv. Chem. Phys.* **1997**, *101*, 47.
(237) Somlói, J.; Kazakov, V. A.; Tannor, D. J. *Chem. Phys.* **1993**, *172*, 85.
(238) Amstrup, B.; Doll, J. D.; Sauerbrey, R. A.; Szabó, G.; Lörincz, A. *Phys. Rev. A* **1993**, *48*, 3830.
(239) Tannor, D. J.; Rice, S. A. *J. Chem. Phys.* **1986**, *85*, 5805.
(240) Shi, S.; Rabitz, H. *Chem. Phys.* **1989**, *139*, 185.
(241) Rabitz, H.; Shi, S. *Adv. Mol. Vibr. Collision Dyn.* **1991**, *1A*, 187.
(242) Warren, W. S.; Rabitz, H.; Dahleh, M. *Science* **1993**, *259*, 1581.
(243) Kosloff, R.; Rice, S. A.; Gaspard, P.; Tersigni, S.; Tannor, D. J. *Chem. Phys.* **1989**, *139*, 201.
(244) Tersigni, S. H.; Gaspard, P.; Rice, S. A. *J. Chem. Phys.* **1990**, *93*, 1670.
(245) Judson, R. S.; Rabitz, H. *Phys. Rev. Lett.* **1992**, *62*, 1500.
(246) Goldberg, D. E. *Genetic Algorithms in Search, Optimization, and Machine Learning*; Addison-Wesley: Reading, MA, 1993.
(247) Schwefel, H. P. *Evolution and Optimum Seeking*; Wiley: New York, 1995.
(248) Assion, A.; Baumert, T.; Bergt, M.; Brixner, T.; Kiefer, B.; Seyfried, V.; Strehle, M.; Gerber, G. In Springer Series in Chemical Physics, Vol. 63; Elsässer, T., Fujimoto, J. G., Wiersma, D. A., Zinth, W., Eds.; Springer: Berlin, 1998; p 471.
(249) Rabitz, H.; de Vivie-Riedle, R.; Motzkus, M.; Kompa, K. *Science* **2000**, *288*, 824.
(250) Hornung, T.; Motzkus, M.; de Vivie-Riedle, R. *Phys. Rev. A* **2002**, *65*, 021403.
(251) Tannor, D. J.; Kosloff, R.; Bartana, A. *Faraday Discuss.* **1999**, *113*, 365.
(252) Tannor, D. J.; Bartana, A. *J. Phys. Chem. A* **1999**, *103*, 10359.
(253) Bartana, A.; Kosloff, R.; Tannor, D. J. *Chem. Phys.* **2001**, *267*, 195.
(254) Palao, J. P.; Kosloff, R. *Phys. Rev. Lett.* **2002**, *89*, 188301.
(255) Tesch, C. M.; de Vivie-Riedle, R. *Phys. Rev. Lett.* **2002**, *89*, 157901.
(256) Metiu, H.; Engel, V. *J. Chem. Phys.* **1990**, *93*, 5693.
(257) Lu, Z. M.; Rabitz, H. *Phys. Rev. A* **1995**, *52*, 1961.
(258) Lu, Z. M.; Rabitz, H. *J. Phys. Chem.* **1995**, *99*, 13731.
(259) Armstrup, B. A.; Toth, G. J.; Rabitz, H.; Lörinz, A. *Chem. Phys.* **1995**, *201*, 95.
(260) Yan, Y. J.; Gillilan, R. E.; Whitnell, R. M.; Wilson, K. R.; Mukamel, S. *J. Phys. Chem.* **1993**, *97*, 2320.
(261) Krause, J. L.; Whitnell, R. M.; Wilson, K. R.; Yan, Y. L.; Mukamel, S. *J. Chem. Phys.* **1993**, *99*, 6562.
(262) Krause, J. L.; Whitnell, R. M.; Wilson, K. R.; Yan, Y. L. In *Femtosecond Chemistry*; Manz, J., Wöste, L., Eds.; VCH: Weinheim, 1995.
(263) Kohler, B.; Yakovlev, V. V.; Che, J.; Krause, J. L.; Messina, M.; Wilson, K. R.; Schwentner, N.; Whitnell, R. M.; Yan, Y. L. *Phys. Rev. Lett.* **1995**, *74*, 3360.
(264) Che, J.; Messina, M.; Wilson, K. R.; Apkarian, V. A.; Li, Z.; Martens, C. C.; Zadoyan, R.; Yan, Y. *J. Phys. Chem.* **1996**, *100*, 7873.
(265) Bardeen, C. J.; Che, J.; Wilson, K. R.; Yakovlev, V. V.; Cong, P.; Kohler, B.; Krause, J. L.; Messina, M. *J. Phys. Chem. A* **1997**, *101*, 3815.
(266) Yan, Y. J. *Annu. Rep. Prog. Chem., Sect. C: Phys. Chem.* **1998**, *94*, 397.
(267) Yan, Y. J.; Shen, Z. W.; Zhao, Y. *Chem. Phys.* **1998**, *233*, 191.
(268) Yan, Y. J.; Che, J.; Krause, J. L. *Chem. Phys.* **1997**, *217*, 297.
(269) Yan, Y. J.; Cao, J. S.; Shen, Z. W. *J. Chem. Phys.* **1997**, *107*, 3471.
(270) Xu, R.; Cheng, J.; Yan, Y. *J. Phys. Chem. A* **1999**, *103*, 10611.
(271) Shen, Z.; Yan, Y.; Cheng, J.; Shuang, F.; Zhao, Y.; He, G. *J. Chem. Phys.* **1999**, *110*, 7192.
(272) Shen, Z.; Engel, V.; Xu, R.; Cheng, J.; Yan, Y. *J. Chem. Phys.* **2002**, *117*, 6142.
(273) Domcke, W.; Stock, G. *Adv. Chem. Phys.* **1997**, *100*, 1.
(274) Kühl, A.; Domcke, W. *J. Chem. Phys.* **2002**, *116*, 263.

(275) Egorova, D.; Thoss, M.; Domcke, W. *J. Chem. Phys.* **2003**, *119*, 2761.
(276) Pople, J. A.; Gill, P. M. W.; Johnson, B. G. *Chem. Phys. Lett.* **1992**, *199*, 577.
(277) Johnson, B. G.; Gill, P. M. W.; Pople, J. A. *J. Chem. Phys.* **1993**, *98*, 5612.
(278) Johnson, B. G.; Frisch, M. J. *J. Chem. Phys.* **1994**, *100*, 7429.
(279) Jellinek, J.; Bonačić-Koutecký, V.; Fantucci, P.; Wiechert, M. *J. Chem. Phys.* **1994**, *101*, 10092.
(280) Fantucci, P.; Bonačić-Koutecký, V.; Jellinek, J.; Wiechert, M.; Harrison, R. J.; Guest, M. F. *Chem. Phys. Lett.* **1996**, *250*, 47.
(281) Reichardt, D.; Bonačić-Koutecký, V.; Fantucci, P.; Jellinek, J. *Z. Phys. D* **1997**, *40*, 486.
(282) Bonačić-Koutecký, V.; Jellinek, J.; Wiechert, M.; Fantucci, P. *J. Chem. Phys.* **1997**, *107*, 6321.
(283) Reichardt, D.; Bonačić-Koutecký, V.; Fantucci, P.; Jellinek, J. *Chem. Phys. Lett.* **1997**, *279*, 129.
(284) Parr, R. G.; Yang, W. *Density functional theory of atoms and molecules*; Oxford University Press: London, 1989.
(285) Perdew, J. P. *Phys. Rev. Lett.* **1985**, *55*, 1665.
(286) Perdew, J. P.; Wang, Y. *Phys. Rev. B* **1986**, *33*, 8800.
(287) Becke, A. D. *Phys. Rev. A* **1988**, *98*, 3098.
(288) Lee, C.; Yang, W.; Parr, R. G. *Phys. Rev. B* **1985**, *37*, 785.
(289) Ziegler, T. *Chem. Rev.* **1991**, *91*, 651.
(290) Verlet, L. *Phys. Rev.* **1967**, *159*, 98.
(291) Bonačić-Koutecký, V.; Fantucci, P.; Koutecký, J. In *The Encyclopedia of Computational Chemistry*; Schleyer, P. v. R., Allinger, N. L., Clark, T., Gasteiger, J., Kollman, P. A., Schaefer, H. F., III, Schreiner, P. R., Eds.; John Wiley & Sons: Chichester, U.K., 1998; Vol. 2; p 876.
(292) Hartmann, M.; Pittner, J.; v. Dam, H.; Bonačić-Koutecký, V. *Eur. Phys. J. D* **1999**, *9*, 393.
(293) Bonačić-Koutecký, V.; Hartmann, M.; Reichardt, D.; Fantucci, P. In *Recent Advances in Density Functional Methods*, Part III; Barone, V., Bencini, A., Fantucci, P., Eds.; World Scientific: Singapore, 2000.
(294) Bonačić-Koutecký, V.; Fantucci, P.; Koutecký, J. In *Cluster and Nanostructure Interfaces*; Jena, P., Khana, S. N., Rao, B. K., Eds.; World Scientific: Singapore, 2000.
(295) Jensen, F. *Introduction to Computational Chemistry;* John Wiley & Sons: Chichester, U.K., 1999.
(296) Szabo, A.; Ostlund, N. *Modern Quantum Chemistry*; McGraw-Hill: 1982.
(297) Yarkony, D., Ed. *Modern electronic structure theory*; World Scientific: 1995.
(298) Hartke, B.; Carter, E. A. *J. Chem. Phys.* **1992**, *97*, 6569.
(299) Hartke, B.; Carter, E. A. *Chem. Phys. Lett.* **1993**, *216*, 324.
(300) Gibson, D. A.; Carter, E. A. *J. Phys. Chem.* **1993**, *97*, 13429.
(301) Gibson, D. A.; Ionova, I. V.; Carter, E. A. *Chem. Phys. Lett.* **1995**, *240*, 261.
(302) Gibson, D. A.; Carter, E. A. *Mater. Phys.* **1996**, *89*, 1265.
(303) Helgaker, T.; Uggerud, E.; Jensen, H. J. A. *Chem. Phys. Lett.* **1990**, *173*, 145.
(304) Uggerud, E.; Helgaker, T. *J. Am. Chem. Soc.* **1992**, *114*, 4265.
(305) da Silva, A. J. R.; Radeke, M. R.; Carter, E. A. *Surf. Sci. Lett.* **1997**, *381*, L628.
(306) da Silva, A. J. R.; Pang, J. W.; Carter, E. A.; Neuhauser, D. *J. Phys. Chem. A* **1998**, *102*, 881.
(307) Foresman, J. B.; Head-Gordon, M.; Pople, J. A.; Frisch, M. J. *J. Phys. Chem.* **1992**, *96*, 135.
(308) Liu, Z.; Carter, L. E.; Carter, E. A. *J. Phys. Chem.* **1995**, *99*, 4355.
(309) Frisch, M. J.; Trucks, G. W.; Schlegel, H. B.; et al. *GAUSSIAN 98*; Gaussian Inc.: Pittsburgh, PA, 1998.
(310) Ahlrichs, R.; Bär, M.; Häser, M.; Horn, H.; Kölmel, M. *Chem. Phys. Lett.* **1989**, *162*, 165.
(311) Guest, M. F.; van Lenthe, J. H.; Kendrick, J. *GAMESS−UK, Generalised Atomic and Molecular Electronic Structure System*, Version 6.2.
(312) Stanton, J. F.; Bartlett, R. J. *J. Chem. Phys.* **1993**, *98*, 7029.
(313) Bartlett, R. J.; Stanton, J. F. *Rev. Comput. Chem.* **1994**, *5*, 65.
(314) Nooijen, M.; Bartlett, R. J. *J. Chem. Phys.* **1997**, *106*, 6441.
(315) Buenker, R. J. *Theor. Chim. Acta* **1974**, *35*, 33.
(316) Buenker, R. J.; Peyerimhoff, S. D.; Butscher, W. *Mol. Phys.* **1978**, *35*, 771.
(317) Michl, J.; Bonačić-Koutecký, V. *Electronic Aspects of Organic Photochemistry*; John Wiley & Sons Inc.: New York, 1990.
(318) Dallos, M.; Lischka, H.; Shepard, R.; Yarkony, D. R.; Szalay, P. G. *J. Chem. Phys.* **2004**, *120*, 7330.
(319) Lischka, H.; Dallos, M.; Szalay, P. G.; Yarkony, D. R.; Shepard, R. *J. Chem. Phys.* **2004**, *120*, 7322.
(320) Hegarty, D.; Robb, M. A. *Mol. Phys.* **1979**, *38*, 1795.
(321) Eade, R. H. E.; Robb, M. A. *Chem. Phys. Lett.* **1981**, *83*, 362.
(322) Roos, B. O.; Taylor, P. R.; Siegbahn, P. E. M. *Chem. Phys.* **1980**, *48*, 1980.
(323) Saalmann, U.; Schmidt, R. *Z. Phys. D* **1996**, *38*, 153.
(324) Saalmann, U. Nicht-adiabatische Quantenmolekulardynamik-Ein neuer Zugang zur Dynamik atomarer Vielteilchensysteme. Ph.D. Thesis, Technische Universität Dresden, 1997.
(325) Schmidt, R.; Knospe, O.; Saalmann, U. *Il Nouovo Chim.* **1997**, *110*, 1201.
(326) Saalmann, U.; Schmidt, R. *Phys. Rev. Lett.* **1998**, *80*, 3213.
(327) Knospe, O.; Jellinek, J.; Saalmann, U.; Schmidt, R. *Eur. Phys. J. D* **1999**, *5*, 1.
(328) Kunert, T.; Schmidt, R. *Phys. Rev. Lett.* **2001**, *86*, 5258.
(329) Doltsinis, N. L.; Marx, D. *Phys. Rev. Lett.* **2002**, *88*, 166402.
(330) Granucci, G.; Toniolo, A. *Chem. Phys. Lett.* **2000**, *325*, 79.
(331) Granucci, G.; Persico, M.; Toniolo, A. *J. Chem. Phys.* **2001**, *114*, 10608.
(332) Cattaneo, P.; Persico, M. *J. Am. Chem. Soc.* **2001**, *123*, 7638.
(333) Persico, N.; Granucci, G.; Inglese, S.; Laino, T.; Toniolo, A. *THEOCHEM* **2003**, *621*, 119.
(334) Schultz, T.; Quenneville, J.; Levine, B.; Toniolo, A.; Martinez, T. J.; Lochbrunner, S.; Schmitt, M.; Schaffer, J. P.; Zgierski, M. Z.; Stolow, A. *J. Am. Chem. Soc.* **2003**, *125*, 8098.
(335) Donoso, A.; Zheng, Y.; Martens, C. *J. Chem. Phys.* **2003**, *119*, 5010.
(336) Donoso, A.; Martens, C. *Phys. Rev. Lett.* **2001**, *87*, 223202.
(337) Wigner, E. *Phys. Rev.* **1932**, *40*, 749.
(338) Hillary, M.; O'Connel, R. F.; Scully, M. O.; Wigner, E. P. *Phys. Rep.* **1984**, *106*, 1984.
(339) Moyal, J. E. *Proc. Cambridge Philos. Soc.* **1949**, *45*, 99.
(340) Li, Z.; Fang, J.-Y.; Martens, C. C. *J. Chem. Phys.* **1996**, *104*, 6919.
(341) Mukamel, S. *Principles of Nonlinear Optical Spectroscopy*; Oxford University Press: 1995.
(342) Heller, E. J. *J. Chem. Phys.* **1976**, *64*, 4912.
(343) Heller, E. J. *J. Chem. Phys.* **1976**, *65*, 1289.
(344) Lopreore, C. L.; Wyatt, R. E. *Phys. Rev. Lett.* **1999**, *82*, 5190.
(345) Wyatt, R. E.; Lopreore, C. L.; Parlant, G. *J. Chem. Phys.* **2001**, *114*, 5113.
(346) Lopreore, C. L.; Wyatt, R. E. *J. Chem. Phys.* **2002**, *116*, 1228.
(347) Trahan, C. J.; Hughes, K.; Wyatt, R. E. *J. Chem. Phys.* **2003**, *118*, 9911.
(348) Trahan, C. J.; Wyatt, R. E. *J. Chem. Phys.* **2003**, *118*, 4784.
(349) Tully, J. C. *J. Chem. Phys.* **1990**, *93*, 1061.
(350) Kohen, D.; Stillinger, F. H.; Tully, J. C. *J. Chem. Phys.* **1998**, *109*, 4713.
(351) Fang, J.-Y.; Hammes-Schiffer, S. *J. Chem. Phys.* **1999**, *110*, 11166.
(352) Hack, M. D.; Truhlar, D. G. *J. Phys. Chem. A* **2000**, *104*, 7917.
(353) Webster, F.; Rossky, P. J.; Friesner, R. A. *J. Chem. Phys.* **1994**, *100*, 4835.
(354) Coker, D. F.; Xiao, L. *J. Chem. Phys.* **1995**, *102*, 496.
(355) Herman, M. F. *J. Chem. Phys.* **1995**, *103*, 8081.
(356) Herman, M. F. *Int. J. Quantum Chem.* **1998**, *70*, 897.
(357) Herman, M. F. *J. Chem. Phys.* **1999**, *110*, 4141.
(358) Hack, M. D.; Wensmann, A. M.; Truhlar, D. G.; Ben-Nun, M.; Martinez, T. J. *J. Chem. Phys.* **2001**, *115*, 1172.
(359) Kapral, R.; Ciccotti, G. *J. Chem. Phys.* **1999**, *110*, 8919.
(360) Nielsen, S.; Kapral, R.; Ciccotti, G. *J. Chem. Phys.* **2000**, *112*, 6543.
(361) Martens, C. C.; Fang, J.-Y. *J. Chem. Phys.* **1997**, *106*, 4918.
(362) Donoso, A.; Kohen, D.; Martens, C. C. *J. Chem. Phys.* **2000**, *112*, 7345.
(363) Heller, E. J. *J. Chem. Phys.* **1975**, *62*, 1544.
(364) Pechukas, P. *Phys. Rev.* **1969**, *181*, 174.
(365) Pechukas, P.; Davis, J. P. *J. Chem. Phys.* **1972**, *56*, 4970.
(366) Kosloff, D.; Kosloff, R. *Comput. Phys. Commun.* **1983**, *30*, 333.
(367) Tal Ezer, H.; Kosloff, R. *J. Chem. Phys.* **1984**, *81*, 3967.
(368) Kosloff, R. *J. Phys. Chem.* **1988**, *92*, 2087.
(369) Kosloff, R. In *Dynamics of Molecules and Chemical Reactions*; Wyatt, R. E., Zhang, J. Z. H., Eds.; Marcel Dekker, Inc.: New York, Basel, Hong Kong, 1996.
(370) Light, J. C.; Carrington, T. *Adv. Chem. Phys.* **2000**, *203*, 263.
(371) Braun, M.; Engel, V. *J. Chem. Phys.* **1998**, *108*, 8983.
(372) Engel, V.; Metiu, H. *J. Chem. Phys.* **1989**, *91*, 1596.
(373) Rubner, O.; Meier, C.; Engel, V. *J. Chem. Phys.* **1997**, *107*, 1066.
(374) Bonačić-Koutecký, V.; Pittner, J.; Boiron, M.; Fantucci, P. *J. Chem. Phys.* **1999**, *110*, 3876.
(375) Furche, F.; Ahlrichs, R.; Weis, P.; Jacob, C.; Gilb, S.; Bierweiler, T.; Kappes, M. M. *J. Chem. Phys*. **2002**, *117*, 6982.
(376) Weis, P.; Bierweiler, T.; Gilb, S.; Kappes, M. M. *Chem. Phys. Lett.* **2002**, *355*, 355.
(377) Haruta, M. *Catal. Today* **1997**, *36*, 153.
(378) Lee, T. H.; Ervin, K. M. *J. Phys. Chem.* **1994**, *98*, 10023.
(379) Salisbury, B. E.; Wallace, W. T.; Whetten, R. L. *Chem. Phys.* **2000**, *262*, 131.
(380) Taylor, K. J.; Pettiette-Hall, C. L.; Cheshnovsky, O.; Smalley, R. E. *J. Chem. Phys.* **1992**, *96*, 3319.
(381) Ho, J.; Ervin, K. M.; Lineberger, W. C. *J. Chem. Phys.* **1990**, *93*, 6987.
(382) Handschuh, H.; Ganteför, G.; Bechtold, P. S.; Eberhardt, W. *J. Chem. Phys.* **1994**, *100*, 7093.
(383) Lüttgens, G.; Pontius, N.; Bechtold, P. S.; Neeb, M.; Eberhardt, W. *Phys. Rev. Lett.* **2002**, *88*, 076102.
(384) Negishi, Y.; Nakajima, Y.; Kaya, K. *J. Chem. Phys.* **2001**, *115*, 3657.

(385) Varganov, S. A.; Olson, R. M.; Gordon, M. S.; Metiu, H. *J. Chem. Phys.* **2003**, *119*, 2531.
(386) Mills, G.; Gordon, M. S.; Metiu, H. *J. Chem. Phys.* **2003**, *118*, 4198.
(387) Scharf, D.; Landman, U.; Jortner, J. *J. Chem. Phys.* **1987**, *87*, 2716.
(388) Rajagopal, G.; Barnett, R. N.; Landman, U. *Phys. Rev. Lett.* **1991**, *67*, 727.
(389) Landman, U. In *Physics and chemistry of finite systems: from clusters to crystals*; Jena, P., Khanna, S. N., Rao, B. K., Eds.; Kluwer: Dodrecht, The Netherlands, 1992; Vol. I.
(390) Galli, G.; Andreoni, W.; Tosi, M. P. *Phys. Rev. A* **1986**, *34*, 3580.
(391) Rajagopal, F.; Barnett, R. N.; Nitzan, A.; Landman, U.; Honea, E.; Labastie, P.; Homer, M. L.; Whetten, R. L. *Phys. Rev. Lett.* **1990**, *64*, 2933.
(392) Pandey, R.; Seel, M.; Kunz, A. *Phys. Rev. B* **1990**, *41*, 7955.
(393) Weiss, P. W.; Ochsenfeld, C.; Ahlrichs, R.; Kappes, M. M. *J. Chem. Phys.* **1992**, *97*, 2553.
(394) Bonačić-Koutecký, V.; Fuchs, C.; Gaus, J.; Pittner, J.; Koutecký, J. *Z. Phys. D* **1993**, *26*, 192.
(395) Häkkinen, H.; Barnett, R. N.; Landman, U. *Chem. Phys. Lett.* **1995**, *232*, 79.
(396) Barnett, R. N.; Cheng, H. P.; Häkkinen, H.; Landman, U. *J. Phys. Chem.* **1995**, *99*, 7731.
(397) Ochsenfeld, C.; Gauss, J.; Ahlrichs, R. *J. Chem. Phys.* **1994**, *103*, 7401.
(398) Giraud-Girard, J.; Maynau, D. *Z. Phys. D* **1992**, *23*, 91.
(399) Giraud-Girard, J.; Maynau, D. *Z. Phys. D* **1994**, *32*, 249.
(400) Bergmann, T.; Limberger, H.; Martin, T. P. *Phys. Rev. Lett.* **1988**, *60*, 1767.
(401) Honea, E. C.; Homer, M. L.; Whetten, R. L. *Phys. Rev. B* **1989**, *63*, 394.
(402) Poncharal, P.; L'Hermite, J. M.; Labastie, P. *Chem. Phys. Lett.* **1996**, *253*, 463.
(403) Pollack, S.; Wang, C. R. C.; Kappes, M. M. *Chem. Phys. Lett.* **1990**, *175*, 209.
(404) Yang, Y. A.; Conover, C. W.; Bloomfield, L. A. *Chem. Phys. Lett.* **1989**, *158*, 279.
(405) Xia, P.; Bloomfield, L. A. *Phys. Rev. Lett.* **1993**, *70*, 1779.
(406) Xia, P.; Cox, A. J.; Bloomfield, L. A. *Z. Phys. D* **1993**, *26*, 1841.
(407) Labastie, P.; L'Hermite, J. M.; Poncharal, P.; Sence, M. *J. Chem. Phys.* **1995**, *103*, 6362.
(408) Durand, G.; Spiegelman, F.; Poncharal, P.; Labastie, P.; L'Hermite, J. M.; Sence, M. *J. Chem. Phys.* **1999**, *110*, 7884.
(409) Durand, G.; Giraud-Girard, J.; Maynau, D.; Spiegelman, F.; Calvo, F. *J. Chem. Phys.* **1999**, *110*, 7871.
(410) Rayane, D.; Compagnon, I.; Antoine, R.; Broyer, M.; Dugourd, P.; Labastie, P.; L'Hermite, J. M.; Le Padallec, A.; Durand, G.; Calvo, F.; Spiegelman, F.; Allouche, A. R. *J. Chem. Phys.* **2002**, *116*, 10730.
(411) Durand, G.; Heitz, M.-C.; Spiegelman, F.; Meier, C.; Mitrić, R.; Bonačić-Koutecký, V.; Pittner, J. *J. Chem. Phys.* **2004**, *121*, 9898.
(412) L'Hermite, J. M.; Blanchet, V.; Le Padellec, A.; Lamory, B.; Labastie, P. *Eur. Phys. J. D* **2004**, *28*, 361.
(413) Schoenlein, R. W.; Peteanu, L. A.; Mathies, R. A.; Shank, C. V. *Science* **254**, *412*, 1991.
(414) Ottolenghi, M.; Sheves, M. *Isr. J. Chem.* **1995**, *35*, 3.
(415) Bearpark, M. J.; Robb, M. A.; Schlegel, H. B. *Chem. Phys. Lett.* **1994**, *223*, 269.
(416) Williams, S. O.; Imre, D. G. *J. Phys. Chem.* **1988**, *92*, 6636.
(417) Williams, S. O.; Imre, D. G. *J. Phys. Chem.* **1988**, *92*, 6648.
(418) Engel, V.; Metiu, H. *J. Chen. Phys.* **1989**, *90*, 6116.
(419) Braun, M.; Engel, V. *Z. Phys. D* **1997**, *39*, 301.
(420) Braun, M.; Meier, C.; Engel, V. *J. Chem. Phys.* **1995**, *103*, 7907.
(421) Kühling, H.; Rutz, S.; Kobe, K.; Schreiber, E.; Wöste, L. *J. Phys. Chem.* **1993**, *97*, 12500.
(422) Schäfer-Bung, B.; Pittner, J.; Bonačić-Koutecký, V. Manuscript in preparation.
(423) Bardeen, C. J.; Che, J.; Wilson, K. R.; Yakovlev, V. V.; Apkarian, V. A.; Martens, C. C.; Zadoyan, R.; Kohler, B.; Messina, M. *J. Chem. Phys.* **1997**, *106*, 8486.
(424) Sundermann, K.; de Vivie-Riedle, R. *J. Chem. Phys.* **1999**, *110*, 1896.
(425) Magnier, S.; Millié, P. *Phys. Rev. A* **1996**, *54*, 204.
(426) Magnier, S.; Aubert-Frécon, M.; Millié, P. J. *Mol. Spectrosc.* **2000**, *200*, 96.
(427) Demiralp, M.; Rabitz, H. *Phys. Rev. A* **1998**, *57*, 2420.
(428) Krotov, V. F. *Control Cybernetics* **1988**, *17*, 115.
(429) Manz, J.; Sundermann, K.; de Vivie-Riedle, R. *Chem. Phys. Lett.* **1998**, *290*, 415.
(430) de Vivie-Riedle, R.; Sundermann, K. *Appl. Phys. B* **2000**, *71*, 285.
(431) Mitrić, R.; Bürgel, C.; Burda, J.; Bonačić-Koutecký, V. *Eur. Phys. J. D* **2003**, *24*, 41.
(432) Kohler, B.; Krause, J. L.; Raksi, F.; Rose-Petruck, C.; Whitnell, R. M.; Wilson, K. R.; Yakovlev, V. V.; Yan, Y.; Mukamel, S. *J. Phys. Chem.* **1993**, *97*, 12602.
(433) Kohler, B.; Krause, J.; Raksi, F.; Wilson, K. R.; Whitnell, R. M.; Yakovlev, V. V.; Yan, Y. L. *Acc. Chem. Res.* **1995**, *28*, 133.
(434) Cheng, J. X.; Shen, Z. W.; Yan, Y. J. *J. Chem. Phys.* **1998**, *109*, 1654.
(435) Rice, J. E.; Amos, R. D.; Handy, N. C.; Lee, T. J.; Schaefer, H. F. I. *J. Chem. Phys.* **1986**, *85*, 963.
(436) Lee, T. J.; Handy, N. C.; Rice, J. E.; Scheiner, A. C.; Schaefer, H. F. I. *J. Chem. Phys.* **1986**, *85*, 3930.

CR0206925